ABSTRACT

Title of dissertation: IDENTIFYING ATOMIC AND MICROSTRUCTURAL RESPONSES IN ANHYSTERETIC Fe-BASED FERROMAGNETIC SHAPE MEMORY ALLOYS

Jacob Steiner
Doctor of Philosophy, 2018

Dissertation directed by: Professor Manfred Wuttig
Department of Materials Science and Engineering

Very soft ferromagnets are commonly amorphous so that no magnetocrystalline anisotropy energy density contributes to the coercivity. This thesis focuses on a class of Fe-based alloys softer than amorphous ferromagnets but crystalline in structure, exhibiting linear, isotropic, as well as totally hysteresis-free magnetization. This class includes Fe-Ga, Al, Ge, Si and Pd alloys, and the majority of the experimental studies focused on FeGa alloys with compositions between 17 and 26 at. % Ga. FeGa has seen much research since the discovery of its large saturation magnetostriction, $\lambda_{\parallel-\perp}$, up to 310 ppm, reported by Clark et al. in 2000 [1]. Our studies probed the magnetic, magnetostrictive, and structural characteristics of these alloys to elucidate the origin of its anomalous magnetic and magnetoelastic properites. The magnetostriction we observe defies classical theories established by Joule in 1847, which pertain to only single phase, crystalline materials. Magnetic anisotropy measurements demonstrate the FeGa alloys possess both cubic and uniaxial symmetry, indicating the presence of more than one phase, and a measured

soft anisotropy constant of 1000 J/m^3 for the cubic symmetry deviates from conventional proportionality between large magnetostriction and magnetic anisotropy in materials. Selected area and nanoelectron diffraction performed in a transmission electron microscope confirm the multi-phase nature of the FeGa alloys' microstructure, including disordered A2, ordered $D0_3$, and 6M $D0_3$ martensite phases. High resolution images show the microstructure is comprised of $\sim$5 nm crystallites, even for alloys manufactured to be single-crystalline. Novel *in situ* field measurements were carried out in the microscope to probe the structure as a function of field, and these results demonstrate that the volume fraction of $D0_3$ appears to vary in response to the field. It is also shown that the magnetic and structural characteristics of FeGa alloys change with repeated cycles of thermal and magnetic measurements. The $Fe_{82}Ga_{18}$ alloy studied exhibited increased $\lambda_{\parallel-\perp}$ from 300 to 600 ppm, increased signal for uniaxial magnetic anisotropy, and increased $D0_3$ and 6M volume fraction. These results have significant implications for future modelling of magnetostrictive behavior that takes into account varying phase content of multi-phase alloys, and the results also highlight the significance of processing and kinetics in the Fe-Ga system.

IDENTIFYING ATOMIC AND MICROSTRUCTURAL RESPONSES IN ANHYSTERETIC Fe-BASED FERROMAGNETIC SHAPE MEMORY ALLOYS

by

Jacob Steiner

Dissertation submitted to the Faculty of the Graduate School of the
University of Maryland, College Park in partial fulfillment
of the requirements for the degree of
Doctor of Philosophy
2018

Advisory Committee:
Professor Manfred Wuttig, Chair/Advisor
Professor Abdellah Lisfi
Professor Lourdes Salamanca-Riba
Professor John Cumings
Professor Ichiro Takeuchi
Professor Alison Flatau

Table of Contents

List of Tables

List of Figures

Chapter 1: Introduction

Actuator and sensor technologies require materials that exhibit transducive properties with low hysteresis, or energy loss, in their actuating mechanism. Terfenol-D, since its discovery by Clark at the Naval Ordinance Laboratory in the 1970s [3], is the most well-established magnetoelastic transducer and has seen extensive use in magnetic sensing applications, underwater acoustic projectors, sonar, and more [4–6]. It exhibits gigantic strain when saturated magnetically, up to 2%, and possesses a modicum of hysteresis, but it is prohibitively costly to fabricate due to the necessary incorporation of Tb and Dy. Its large magnetostriction is a result of careful processing of the alloy to bring it to an equilibrium state at room temperature straddling a morphotropic phase boundary between tetragonal Fe_2Tb and rhombohedral Fe_2Dy. The equilibrium becomes perturbed upon application of a magnetic field, causing extensive growth of one phase over the other, resulting in shape changes throughout the bulk. These lower symmetry ordered crystal structures additionally cause the material to possess significant brittleness and high anisotropy in the magnetostrictive behavior. This inhibits the machinability with only useful longitudinal magnetostrictive responses.

Ferromagnetic shape memory alloys (FSMAs) have undergone intense research

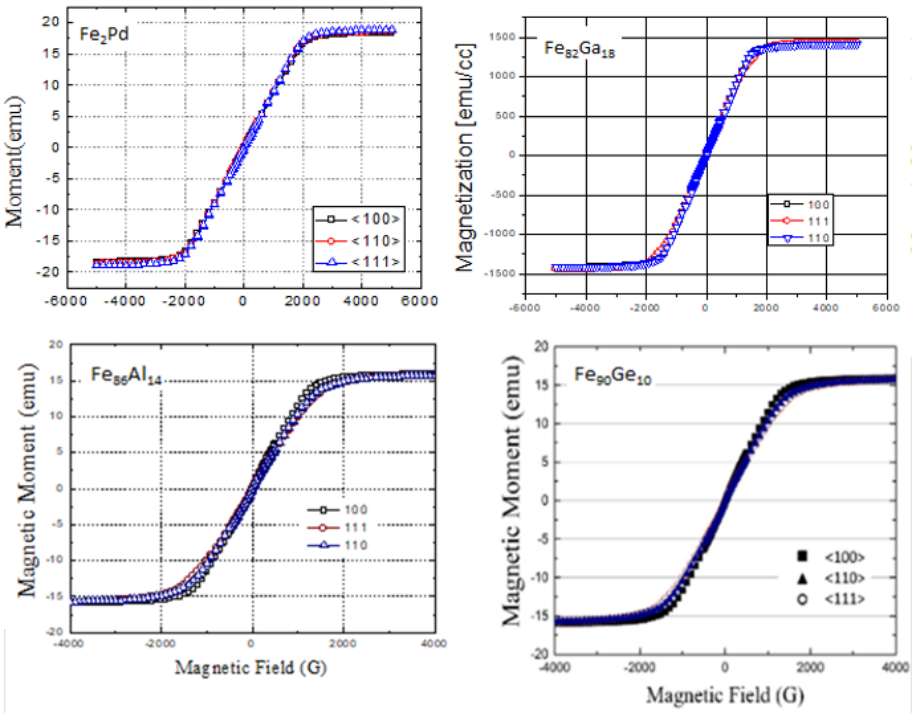

Figure 1.1: Magnetization curves for Fe-binary alloys Fe_2Pd, $Fe_{82}Ga_{18}$, $Fe_{86}Al_{14}$, and $Fe_{90}Ge_{10}$. The magnetization is linear, anhysteretic, and isotropic with respect to crystalline direction in each case. This isotropic behavior contradicts convenviontal behavior of soft magnetic materials.

over the past two decades as alternative candidates to Terfenol-D towards magnetoelastic actuation and sensing. Heusler alloy Ni_2MnGa was the first FSMA discovered by Webster in 1984 [7], yet it took twelve years for its significant magnetostriction, up to 0.2% strain, to be documented by Ullakko in 1996 [8]. Ni_2MnGa has since seen more detailed studies of its magnetoelastic properties, phase equilibria, martensitic transformations, and microstructural development to assess its usefulness as a replacement for Terfenol-D as well as to develop a more fundamental understanding of the mechanisms contributing to its large magnetostriction. Limiting widespread commercialization of Ni_2MnGa for actuation is also its brittleness and lack of machinability imparted by the strict ordering of its Heusler structure,

and the material requires high magnetic fields of 1 T to saturate. FeGa FSMAs consisting of Ga contents between 16-25 at. % have seen the next largest initiative in the literature towards their development as an alternative to Terfenol-D. These alloys exhibit a much smaller saturation magnetostriction up to 400 ppm, or 0.04% strain, but they saturate at lower fields of 0.2 T or less, possess good machinability, extremely low hysteresis, and lower cost elements. In the interest of reducing cost, FeAlGa and FeAl alloys have also been investigated, exhibiting nearly identical material properties save for a lower saturation magnetostriction of 0.02% strain [9].

While it may seem unsurprising that FeAl and FeGa share extremely similar material properties, owing to the fact that Ga and Al belong to the same elemental column, there exist many other Fe-based FSMAs which all belong to the same unique class of magnetostrictors, one characterized not only by high magnetostriction but also through their magnetization behavior. Each of these alloys exhibits isotropic, linear, anhysteretic magnetization behavior until saturation, and examples of these curves are shown in Figure 1.1 for several different alloys: FeGa, FeAl, FePd, and FeGe. While anhysteretic magnetization exists for a wide variety of soft magnetic materials, isotropy in magnetic behavior defies classical theories pertaining to magnetism in materials. Furthermore, magnetostriction along different crystalline directions in these materials is anisotropic, but the behavior does not adhere to elastic laws outlined in the Joulian theory of magnetostriction.

Connecting each of these alloys is both elastic softening and reduced magnetic anisotropy at room temperature. FePd alloys, in particular, possess unusual premartensitic microstructures which form nanoscale twin modulations as an

adaptive mechanism induced by large strain between parent-austente transformations [10–13], and this adaptive mechanism causes anomalous ferromagnetoelastic properties which lead to non-classical magnetic and magnetoelastic behavior. Evidence for such nanoscale martensite and magnetoelastic adaptive mechanism has been mixed in regards to FeGa, which has seen contrary evidence from other research groups studying alloys of similar composition and make. The following section reports on non-classical magnetoelastic behavior evidenced in our own measurements on FePd and FeGa alloys as well as that evidenced historically.

For more background on the concepts discussed in this thesis, a detailed overview of the science of martensitic transformations and shape memory alloys is contained in Appendix A while that of classical magnetism in materials in Appendix B.

Chapter 2: Evidence of Non-Joulian Magnetostriction in FePd and FeGa alloys

2.1 Tenets of Joule Magnetostriction

The vast majority of magnetic materials exhibit a spontaneous strain in the presence of a magnetic field, which was first discovered in by Joule in 1847 on measurements of pure Fe [14]. Materials typically elongate along the direction of the applied field, and experience a contraction in the transverse directions in accordance with Poisson's ratio. This implies the strain is elastic by nature, and Joule developed a phenomenological theory of magnetostriction using a magnetoelastic coupling tensor B_{ij} and elastic constants c_{ij}. For a cubic material, the strain, λ, as a function of field is expressed in terms of direction cosines for magnetization α_{ij} and crystalline axes β_{ij}:

$$\begin{aligned}\lambda = &- \frac{B_1}{c_{11}-c_{12}}\left(\alpha_1^2\beta_1^2 + \alpha_2^2\beta_2^2 + \alpha_3^3\beta_3^3 - \frac{1}{3}\right) \\ &- \frac{B_2}{c_{44}}\left(\alpha_1\alpha_2\beta_1\beta_2 + \alpha_2\alpha_3\beta_2\beta_3 + \alpha_1\alpha_3\beta_1\beta_3\right)\end{aligned} \tag{2.1}$$

Cubic materials have magnetostriction fully characterized by their saturation responses along [100] and [111] directions, expressed as

$$\lambda_{100} = -\frac{2}{3}\frac{B_1}{c_{11} - c_{12}} \tag{2.2}$$

$$\lambda_{111} = -\frac{1}{3}\frac{B_2}{c_{44}}, \tag{2.3}$$

which one can understand as a dilatational and shear response, respectively. The [110] response is a linear combination of these two, given by

$$\lambda_{110} = \frac{1}{4}\lambda_{100} + \frac{3}{4}\lambda_{111}. \tag{2.4}$$

The two constants, λ_{100} and λ_{111}, sufficiently characterize the magnetostrictive response in all possible directions for single phase cubic crystals, changing the expression in 2.1 to

$$\begin{aligned}\lambda = &-\frac{3}{2}\lambda_{100}\left(\alpha_1^2\beta_1^2 + \alpha_2^2\beta_2^2 + \alpha_3^3\beta_3^3 - \frac{1}{3}\right) \\ &- 3\lambda_{111}\left(\alpha_1\alpha_2\beta_1\beta_2 + \alpha_2\alpha_3\beta_2\beta_3 + \alpha_1\alpha_3\beta_1\beta_3\right)\end{aligned} \tag{2.5}$$

If one magnetizes a sample along its [100] direction ($\alpha_1 = \beta_1 = 1$, all others 0), one measures exactly λ_{100} along the parallel axis, and one would also measure $\lambda_{010} = -\frac{1}{2}\lambda_{100}$ in the transverse direction. Magnetostriction is often reported through the difference in strain between these two axes, such that $\lambda_s = \lambda_{\parallel} - \lambda_{\perp} = \frac{3}{2}\lambda_{100}$.

In 1954, Néel developed a fundamental explanation for magnetostriction through a Legendre expansion of the potential energy for atomic bonds, $\mathbf{r}$, using the ex-

change, $g(r)$, dipole-dipole, $l(r)$, and quadrupolar, $q(r)$, interaction terms as expansion coefficients [15]. Thus, different magnetization directions correspond to different equilibrium bond positions, reflected in the elastic strain described in the Joulian model. Having origins related to the dipole and quadrupolar potentials in the crystal, Joule magnetostriction is strongly tied to the magnetic anisotropy of magnetic materials as well. In cubic materials, second order anisotropy is expressed through the magnetization directions, α_i, proportional to an anisotropy constant K_1 as

$$u_A = K_1(\alpha_1^2\alpha_2^2 + \alpha_2^2\alpha_3^2 + \alpha_3^2\alpha_1^2), \tag{2.6}$$

but eq. 2.1 can also be reinterpreted to express additional anisotropy such that

$$u_A = (K_1 + \Delta K)(\alpha_1^2\alpha_2^2 + \alpha_2^2\alpha_3^2 + \alpha_3^2\alpha_1^2), \tag{2.7}$$

where ΔK is a combined expression of the magnetostriction constants [16]:

$$\Delta K = \frac{B_1^2}{c_{11} - c_{12}} - \frac{B_2^2}{2c_{44}} \tag{2.8}$$

This expression represents a powerful relationship between magnetostriction and anisotropy. Materials with high magnetostriction tend to possess high anisotropy, and inversely, materials with high anisotropy tend to possess high magnetostriction.

This brief overview of Joule magnetostriction is expounded upon more in Appendix B.4, but the important tenets of the theory are described to clarify what it means for a material to not exhibit Joulian magneostriction. Joule theory applies if

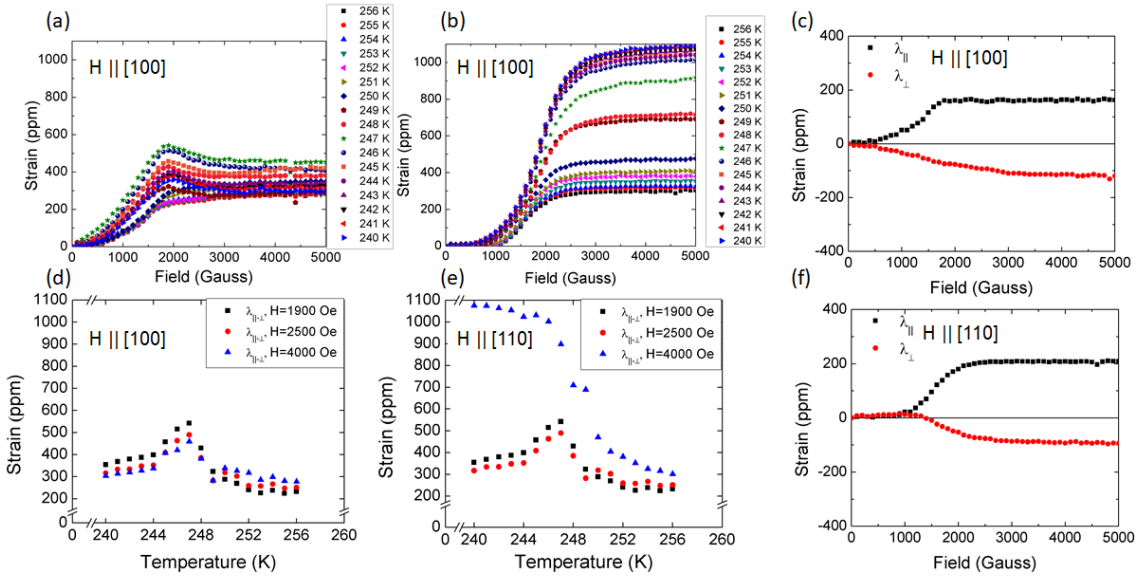

Figure 2.1: Magnetostriction data shown for single crystal $Fe_{68.8}Pd_{31.2}$ at several different temperatures along the **(a)** $\langle 100 \rangle$ and **(b)** $\langle 110 \rangle$ crystalline directions as a function of field. The same data is shown as a function of temperature at select fields ■ 1900 Oe, ● 2500 Oe, and ▲ 4000 Oe, along the **(d)** 100 and **(r)** 110 crystalline directions. **(c)** and **(f)** show magnetostriction measurements taken at 256K for the $\langle 100 \rangle$ and **(b)** $\langle 110 \rangle$ directions, respectively.The data shows $\lambda_{110} \approx \lambda_{100}$ for temperatures above 250 K, below which a martensitic transformation occurs resulting in growth of of λ_{110} from 300 to 1100 ppm, surpassing the magnitude of λ_{100} by over a factor of two.

(1) the magnetic material is crystalline and of single phase, (2) the response is elastic and obeys the relationships of eqs. 2.5 and 2.4, and (3) a high magnetostriction proportionally yields high anisotropy.

2.2 Background and Evidence of Non-Joulian Magnetostriction in FePd

This section summarizes the major conclusions drawn from earlier work on FePd alloys, which Appendix C contains in heavier detail.

The FePd alloys within the 30-35 % Pd composition exhibit anomalous pre-

martensitic behavior and softening of the shear elastic constant, $c_{11} - c_{12}$, which has been reflected in phonon measurements showing softening in the $\{\xi\xi 0\}$ transverse acoustic mode [17, 18]. The quench treatment bypasses phase separation into an equilibrium two-phase mixture of α-FCC and ordered-FCC $L1_0$ and instead stabilizes a martensitic transformation from α-FCC to disorder face-centered tetragonal (FCT). The premartensitic behavior of these alloys manifests as nanoscopic tetragonal distortions along $\langle 110 \rangle$ twinning directions in the microstructure above the transformation temperature, forming what has been called martensitic 'nuclei' that grow and condense in a pseudo-second order transformation mechanism before the material undergoes a bulk first-order transition at the transformation temperature [11, 17].

In the premartensitic state, FePd exhibits large saturation magnetostriction of $\sim$300 ppm. Measurements were carried out on a single crystal sample of $Fe_{68.8}Pd_{31.2}$ from a temperature of 258 K to 248 K along both the [100] and [110] direction, results shown in Figure 2.1. This temperature range covers the behavior above and below the transformation temperature, which was estimated to be 252 K based on a thermal expansion measurement of the same sample. The plots of Fig. 2.1d and 2.1e show the results plotted in Fig. 2.1a and 2.1b, respectively, at constant field as a function of temperature to highlight abrupt changes which occur in the magnetostriction measurements as a result of the phase transformation onset at 250 K. The individual magnetostriction curve for the [100] direction in Fig. 2.1c shows that $\lambda_{010} = -\frac{1}{2}\lambda_{100}$, in accordance with eq. 2.5. However, the individual curve for the [110] direction in Fig. 2.1f completely departs from the magnetoelastic

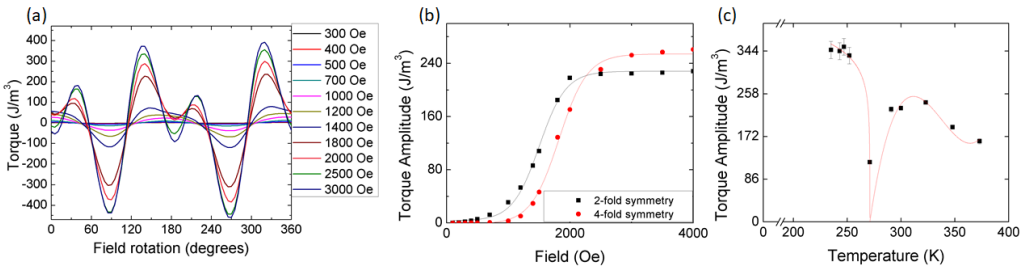

Figure 2.2: **(a)** Magnetic torque data of several field strengths taken at 293K for single crystal $Fe_{68.8}Pd_{31.2}$, **(b)** change of torque amplitudes A and B fitted to $A\sin 4(\theta+\varphi_1)+B\sin 2(\theta+\varphi_2)$ for curves of **(a)** to separate the anisotropy behavior of the ■ 2-fold symmetry and ● 4-fold symmetry, and **(c)** temperature dependence of the 2-fold symmetry with applied field of 3000 Oe. The variation of amplitude for the 2-fold symmetry with temperature attests to the presence of a uniaxial phase in addition to the 4-fold symmetry cubic phase.

framework of Joule. While a large λ_{100} may be understood as a consequence of the elastic constant softening, λ_{111} would be significantly small as c_{44} does not soften as heavily in the material. In Joule's framework, this implies $\lambda_{110} \approx \frac{1}{4}\lambda_{100}$ from the relation in eq. 2.4 and also that $\lambda_{1\bar{1}0} \approx \frac{1}{4}\lambda_{100}$, but the data clearly shows $\lambda_{110} = \lambda_{100} \neq \frac{1}{4}\lambda_{100} \neq \lambda_{1\bar{1}0}$, clearly violating the theory.

Furthermore, one would expect FePd to exhibit significantly high anisotropy because of the large magnetostriction, but magnetic torque measurements carried out on the $Fe_{68.8}Pd_{31.2}$ sample, shown in Figure 2.2, show that it possesses remarkably low anisotropy at saturation, ~425 J/m^3. The magnitude of this is lower than the anisotropy of some metglasses, which are amorphous magnetic materials designed to have low anisotropy by virtue of their lack of crystallinity. The anisotropy response also changes significantly as the material magnetizes, possessing only a 2-fold symmetry at low fields followed by the evolution of a 4-fold symmetry closer to saturation. Fig. 2.2b shows the amplitude of these two phase components as a

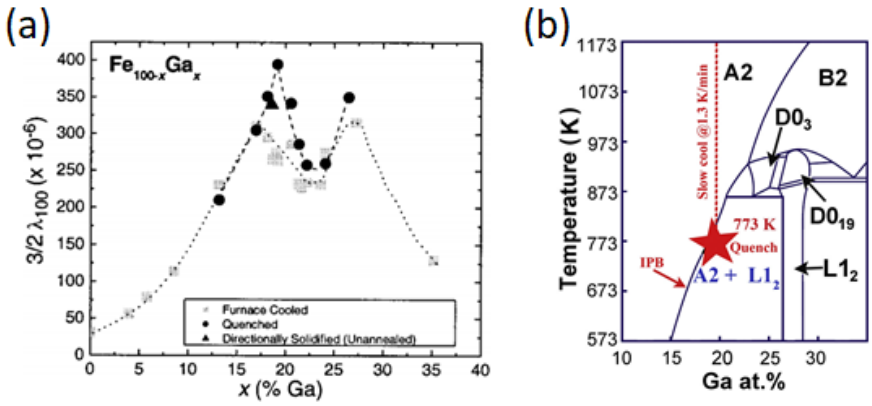

Figure 2.3: Taken from Clark et al. [19],values of $3/2\lambda_{100}$ reported as a function of composition for single crystal alloys in the Fe-Ga binary system either quenched or slow-cooled (10 K/min) following homogenization at 1273 K between 72 and 168h .Two maxima of the striction occur at 18 and 27 at. % Ga for quenched alloys, matching closely to the boundary of a two-phase equilbirium of disordered BCC α+ordered FCC $L1_2$ region, seen in the phase diagram **(b)**, taken from Rahman et al. [2].

function of field, and this implies that two phases exist and contribute to the overall magnetic behavior. Fig. 2.2c documents the amplitude of the 2-fold symmetry as a function of temperature, showing drastic changes towards the transformation temperature of 252 K, which tells us the 2-fold symmetry cannot be accounted for by shape anisotropy of the sample alone.

2.3 Background and Evidence of Non-Joulian Magnetostriction in FeGa

The FeGa alloys within the 15-30 % Ga composition have attracted extensive study for their large magnetostriction, possessing two maxima in the saturation value at 18 and 27 at %, as documented by Clark et al. [19], shown in Figure 2.3. These maxima correspond closely to the boundary of a two-phase disordered-BCC

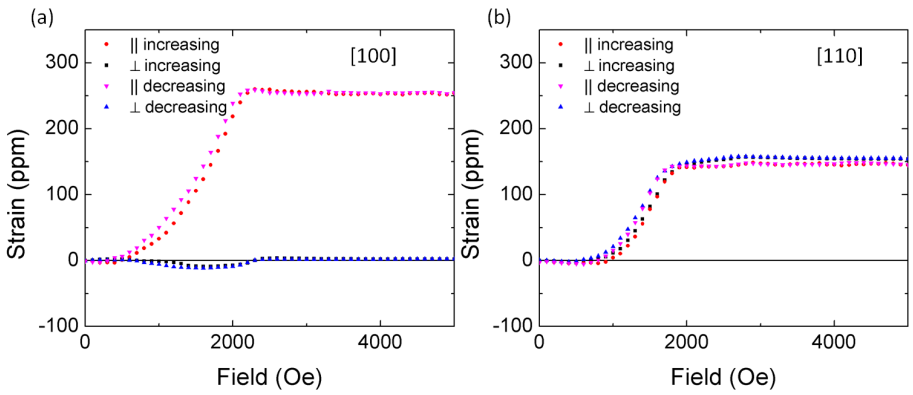

Figure 2.4: Magnetostriction data shown for single crystal $Fe_{83}Ga_{17}$ at room temperatures along the **(a)** $\langle 100 \rangle$ and **(b)** $\langle 110 \rangle$ crystalline directions. The data shows a $\lambda_{110} \approx \frac{1}{31}\lambda_{100} \neq \frac{1}{4}\lambda_{100}$, as expected with the classical Joulian framework of magnetostriction.

A+ordered-FCC $L1_2$ two-phase region, seen in Fig.2.3b. However, most highly magnetostrictive FeGa alloys are fabricated as follows: (1) single crystals grown through the Bridgmann method; (2) homogenization between 1123-1273 K for durations between 72 and 168 h; and (3) either ice-quenching or slow-cooling the sample 10/K per minute to room temperature [19–27]. These alloys tend to exhibit disorderded-BCC A2 or $D0_3$ crystal phases [2, 19–25, 28], with limited evolution of equilbirum ordered-HCP $D0_{19}$ or ordered-FCC crystal phases, which tend to manifest for slower cooling rates of 2 K/min [29]. The origin for these maxima in magnetostriction remains debated in literature, with one school of thought attributing the large magnetostriction to elastic consequences from the variation in elastic shear constant $c' = \frac{1}{2}(c_{11} - c_{12})$ [19, 21, 22, 25], and another attributing the large magnetostriction to severe elastic softening and martensitic behavior [20, 24, 28]. Discpreancies for values of shear constants, magnetoelastic constants, saturation magnetostrictions λ_{100} and λ_{111}, magnetizations, and anisotropy constants vary for alloys of the same

composition throughout reports in the literature and represent the core of this debate.

For instance, He et al. reported this year magnetistrction constants different single crystal alloys of 17 % Ga [25]. Their crystals were first grown as single crystal, annealed at 1273 K for 10 h, and, of those, furnace cooled, ice-quenched after second 1033 K anneal for 30 min, or slow-cooled 10 K/min to 473 K. Their constants definitely fall within the Joulian model. However, our own measurements conducted on the [100] and [110] axes of an $Fe_{83}Ga_{17}$ single crystal homogenized at 1273 K for 2 h followed by a 10 K/min slow-cool to room temperature, shown in Figure 2.4, show $\lambda_{110} = \frac{1}{2}\lambda_{100}$, a ratio that does not fulfill the Joulian tenet that $\lambda_{110} \approx \frac{1}{4}\lambda_{100}$. Furthermore, the individual curve for the [100] direction in Fig. 2.4a shows that $\lambda_{010} = 0 \neq -\frac{1}{2}\lambda_{100}$, also clearly violating the Joulian relationship between parallel and perpendicular response. Both results show that single crystals, either quenched after homogenization at 1273 K, exhibit highly different magnetoelastic properties, and one then must suppose the processing affects the material drastically.

Because much of the magnetostriction within our alloys is non-Joulian, reporting our measurements within the Joulian model would be misleading. It's not possible for a measured λ_{100} to characterize the response along different directions in our alloys, and, as such, further saturation values contained in this thesis will be reported as $\lambda_s = \lambda_{\parallel-\perp} = \lambda_{\parallel} - \lambda_{\perp}$ to distinguish from the convention of $\lambda_s = \frac{3}{2}\lambda_{100}$.

Torque for these FeGa alloys is shown in Figure 2.5, and is anomalously small in light of its magnetostriction, at a little over 1000 J/m^3. It has a dominant 4-fold symmetry, with a small 2-fold shape anisotropy symmetry component causing the

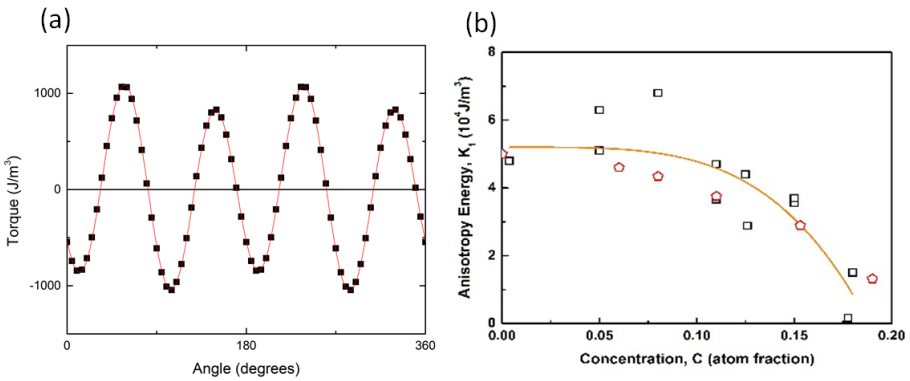

Figure 2.5: **(a)** Room temperature magnetic torque data shown for single crystal $Fe_{83}Ga_{17}$ at saturation and **(b)** taken from [30],the variation in magnetic anisotropy for FeGa (squares) and FeAl (pentagons) alloys as a function of composition.

peak amplitude to vary in height between 90° intervals. Such a value is indicative of an extremely soft magnet, at an order of magnitude less than pure Fe which has anisotropy constants of $K_1 = 4.8 \times 10^4$ J/m^3 and $K_2 = -1.0 \times 10^4$ J/m^3 [16]. The anisotropy energy for these alloys as a function of composition shown in Fig. 2.5b, taken from Rafique, Cullen, and Wuttig's work in 2004 [20], demonstrates a monotonic decrease towards conentrations of 20 at. % Ga, which stand in contrast to calculated values one obtains based on magnetoelastic constants reported by other groups [19, 21]. The decrease in anisotropy also does not reflect the simultaneous increase in magnetostriction for the same Ga concentrations seen in Fig. 2.3. That is, eq. 2.8 predicts an increase an anisotropy proportional to the increase in magnetostriction, which is not exhibited at all in the Fe-Ga system.

In summation, both FePd and FeGa alloys we studied violate the tenets necessary to describe their magnetostrictive responses with the classical Joulian theory, namely that λ_{100} represents a material constant sufficient to describe the saturation values for arbitrary crystalline direction. This makes their magnetostrictve

response non-Joulian in nature, and a new theory must be developed to describe their anomalous magnetic characteristics.

Chapter 3: Hypothesis of Nanoscale, Adaptive Martensite

The differing values of magnetostriction for $Fe_{83}Ga_{17}$ single crystals reported by different research groups suggests alloy processing has a substantial role on the magnetic behavior, which is only recently being explored in the work of Rahman et al. [2]. Taken from their work, Figure 3.1 shows a large enhancement of magnetostriction in $Fe_{81}Ga_{19}$ alloys based on quenching either from a high homogenizing temperature of 1273 K versus a lower temperature of 773 K. The discrepancies across measured values related to the magnetostrictive behavior of FeGa seem to imply that researchers of different groups are studying different materials of different atomic- and microstructures. The alloys of FeGa with extremely low anisotropy energy also tend to sharper decreases in shear elastic constant c' [20,32], depicted in Figure 3.2, and these decreases are towards c' values three orders of magnitude small than those reported FeGa alloys exhibiting Joulian striction [19, 21]. Most groups agree large magnetostriction comes from development of the $D0_3$ phase, and much work has gone on to attemp structural idenfitication in these alloys to determine the crystallographic origin of large magnetostriction. However, due to the fact that the $D0_3$ lattice parameter differs by only 0.2 % compared to the A2 structure [22,29], the $D0_3$ phase can only be uniquely identified by the presence of lower intensity reflections

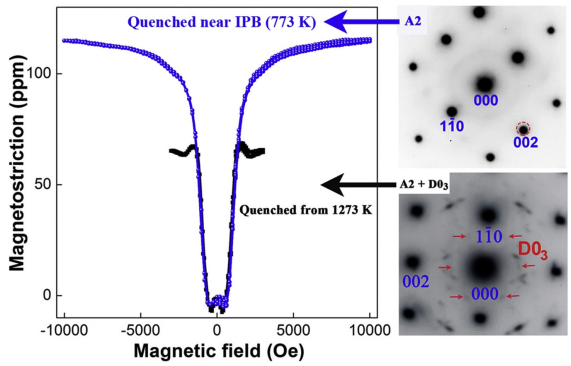

Figure 3.1: Taken from [2] shows magnetostriction data acquired from single crystals of $Fe_{81}Ga_{19}$ either quenched from a homogenization temperature of 1273 K or quenched after slow-cooling from 1273 to 773 K at 2 K /min.

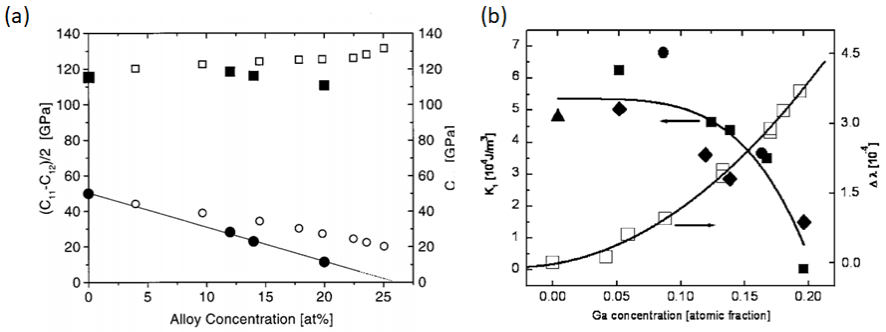

Figure 3.2: **(a)** Taken from [31], variation in elastic constants $c'(\frac{c_{11}-c_{12}}{2})$ and c_{44} for FeGa quenched single crystals 0 - 25 at. % Ga, and **(b)**, taken from [32] , variation in magnetostriction values (open symbols) for FeGa quenched single crystals 0 - 25 at. % Ga reported in literature compared to measured variation in magnetic anisotropy (solid symbols) of quenched single crystal FeGa alloys. The two plots in tandem suggest a relationship between low c', K_1/K_2, and λ_s values for quenched FeGa alloys.

permitted by the ordering of the atoms which are otherwise forbidden in A2. This makes crystallographic data difficult to interpret and correlate closely with the A2 or $D0_3$ phases. Elastic softening is a universal characteristic of martensitic materials exhibiting shape memory properties, and the softening seen in the low anisotropy energy alloys make the likelihood high that martensitic structures develop and have some effect on magnetic anistoropy and magnetoelastic behavior. The reortienta-

tion of tetragonal clusters 15 nm in size under critical stress and magnetic fields was observed through small angle neutron scattering measurements reported by Laver et al. in 2010 [23]. Very recently, Liu et al. found evidence of nanoscale martensitic twin modulation of the $D0_3$ through TEM [33]. The structure of this martensite corresponds to a 6M nanomodulations corresponding to orthorhombic martensites based on stacking fault sequences as documented by Otsuka in 1976 [34].

Alloy	**Heat Treatment**	**Cooling**	**Crystallinity**
$Fe_{83}Ga_{17}$	1273 K, 24 h, Ar atmosphere	Slow-cooled 10 K/ min	Single Crystal, [100] normal
$Fe_{82}Ga_{18}$	1273 K, 24 h, Ar atmosphere	Slow-cooled 10 K/ min	Single Crystal, [100] normal
$Fe_{81}Ga_{19}$	1273 K, 72 h, Ar atmosphere	Ice-quenched	Polycrystalline
$Fe_{78}Ga_{22}$	1273 K, 24 h, Ar atmosphere	10 K/ min	Single Crystal, [100] normal
$Fe_{74}Ga_{26}$	Arc-melted and no anneal	Furnace-cooled	Polycrystalline

Table 3.1: A summary of the different alloys studied detailing their processing history and reported crystallinity.

The experimental evidence of non-Joulian magnetostriction for FeGa alloys of low anisotropy energy, low shear constant, high saturation magnetostriction, and anhysteretic and isotropic magnetization, in accompaniment with documented tetragonal and martensitic structures [23, 33], makes the fact unassailable that the departure from classical magnetization and magnetoelastic mechanisms come from ferromagnetoelastic behavior. Still, this data stands at odds with that of other research groups who do not measure the same characteristics for alloys of the same composition and similar processing history. This can only be reconciled under the assumption that the tendency of 15-30 at% FeGa alloys to form martensite is a consequence of metastable kinetics of different phases' evolution during the heat treatment process. We hypothesize this martensite develops as a consequence of $D0_3$ precipita-

tion during quenching or slow-cooling, and epitaxial strain across A2/$D0_3$ interfaces locally-induces martensitic transformations at the nanoscale. Such martensite develops adaptive qualities which accommodate variations in stress or magnetic field in a near-reversible mechanism, exhibiting magnetic and magnetoelastic responses which defy classical behavior. More details of such martensitic behavior are contained in Appendices C and D, which document earlier work conducted on FePd and FeNi alloys, respectively. To assess the extent and possible adaptive nature of martensite in FeGa alloys, we carried out experiments on alloys of compositions $Fe_{100-x}Ga_x$ ($x = 17, 18, 19, 22$, and 26 at. %), characterizing their magnetic, magnetoelastic, and nanoscale structural characteristics under an *in situ* applied magnetic field in an attempt to connect the three together. Table I details the processing history and reported crystallinity of these alloy, and Table II gives an overview of experimental work carried out. Details of the specific measurement equipment, measurement techniques, and sample preparation techniques employed in these studies is expounded upon in Appendix E.

Alloy	$\varepsilon(T)$	$M(H)$	$\lambda(H,T)$	$L(H)$	**SAD/NED v. H**	**HRTEM v. H**	**DFTEM**
$Fe_{83}Ga_{17}$	✓	✓	✓	–	–	–	–
$Fe_{82}Ga_{18}$	✓	✓	✓	✓	✓	✓	✓
$Fe_{81}Ga_{19}$	✓	✓	✓	–	✓	✓	–
$Fe_{78}Ga_{22}$	✓	✓	✓	–	✓	✓	✓
$Fe_{74}Ga_{26}$	✓	✓	✓	–	–	–	–

Table 3.2: This table clarifies which experimental studies were carried out on each alloy, including measurements of thermal expansion ($\varepsilon(T)$), room temperature magnetization ($M(H)$), temperature dependent magnetostriction curves ($\lambda(H,T)$), room temperature magnetic torque curves at different fields ($L(H)$), selected area and nanoelectron diffraction studies versus magnetic field inside the TEM (SAD/NED v. H), high resolution TEM imaging versus magnetic field inside the TEM (HRTEM v. H), and dark field imaging under two-beam conditions at the nominal operating field inside the TEM (DFTEM).

Chapter 4: Studies on FeGa

4.1 Magnetic Characteristics of FeGa

Thermal expansion curves for the x = 17, 18, 19, 22, and 26 % alloys are shown in Figure 4.1. The $Fe_{83}Ga_{17}$, $Fe_{82}Ga_{18}$, $Fe_{81}Ga_{19}$, and $Fe_{78}Ga_{22}$ samples show slight non-linear responses towards higher temperatures in its expansion. The deviation from linear behavior in both the 17 and 22 % Ga alloys occurs at the same temperature, 327 K, which may be indicative of similar phase transition in both alloys. There is a clear jump in the coefficient of thermal expansion from near 6.3-6 ppm/K at 18 at. % Ga to 8.23 ppm/K at 22 at. % Ga, likely attributable to crystallographic differences expected from the phase diagram.

Room temperature magnetization curves for $Fe_{82}Ga_{18}$ and $Fe_{78}Ga_{22}$ are shown in Figure 4.2, depicting isotropic, anhysteretic behavior as seen in FePd. We demonstrated in previous work on FePd that the slope of the curve is determined by the demagnetization factor of the samples [35], and the derivation of this result based on an analysis of the magnetic energy in the system is found in Appendix C. Both samples were disks with dimensions of 8mm diameter and 0.5 mm thickness, and the demagnetization factor determined from the slope of the curve is measured at 0.270, closely corresponding to the theoretical demagnetization factor of 0.269 for

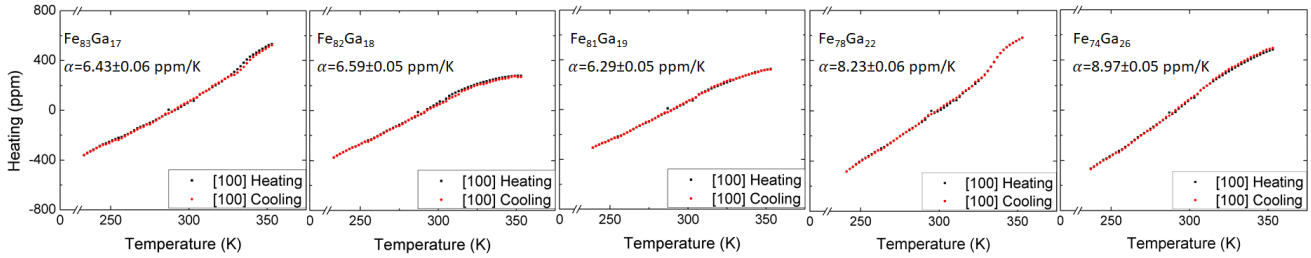

Figure 4.1: Thermal expansion measurements taken over a range of 233-378 K for $Fe_{100-x}Ga_x$ alloys (x = 17, 18, 19, 22, and 26) with corresponding thermal expansion coefficients α reported in the plots. There's a clear jump in α from 6.29 to 8.23 between the $Fe_{81}Ga_{19}$ and $Fe_{78}Ga_{22}$ alloys that might attest to fundamental crystallographic differences between the 17,18, and 19 % compositions versus the 22 and 26 % ones. Anomalous bumps in the expansion occuring near 327 K are seen in both the 17 and 22 at. % Ga alloys.

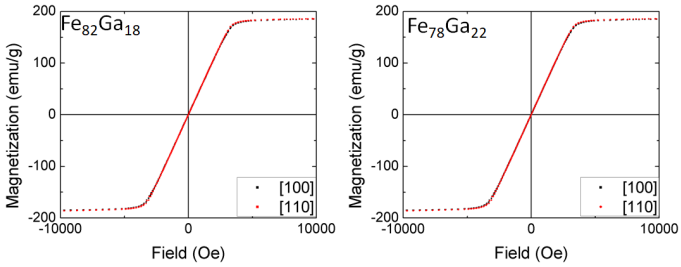

Figure 4.2: Magnetization curves for single crystal $Fe_{82}Ga_{18}$ and $Fe_{78}Ga_{22}$ alloys. Both alloys exhibited linear, anhysteretic, and isotropic magnetization.

magnetic cylinders with a 16:1 aspect ratio [36]. In addition, the two curves are nearly identical, meaning the magnetization remains independent of the crystallographic differences responsible for the change in thermal expansion behavior.

The magnetostriction data for these samples starts to paint a more complex picture of magnetoelastic coupling in these alloys not reflected in the magnetization behavior. Figure 4.3 shows $\lambda_{\parallel-\perp}$ as a function of temperature for the x = 17, 18, 19, 22, 26 % alloys. The data shows very clearly that $Fe_{83}Ga_{17}$ and $Fe_{78}Ga_{22}$ have some sort of magnetostrictive transition occurring near 325K which is liekly connected to the anomalous bump in thermal expansion seen in their heating curves from

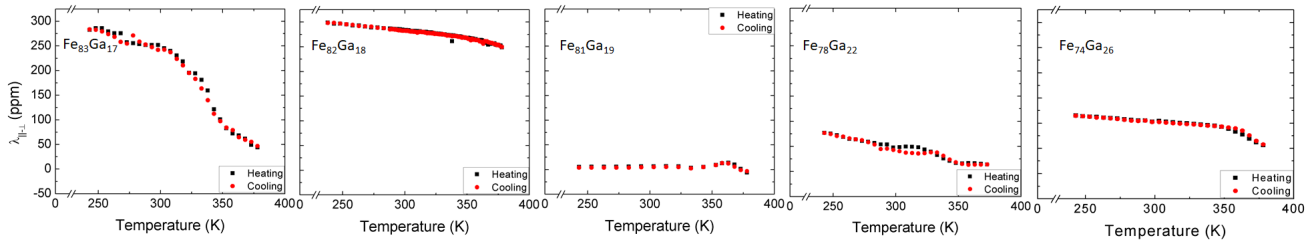

Figure 4.3: Saturation magnetostriction, $\lambda_{\parallel-\perp}$, values plotted as a function of temperature for $Fe_{100-x}Ga_x$ alloys ($x = 17$, 18, 19, 22, and 26). Large room temperature magnetostriction of 250 and 300 ppm was observed for the 17 and 18 at. % Ga alloys, respectively. Significant decreases are seen within the 17 and 22 at. % Ga alloys near 325 K, corresponding to the same temperature at which an anomalous hump in the thermal expansion data appears. Slight decreases are seen in the values for 19 and 26 at. % Ga alloys at 360 K that suggest magnetic transitions not reflected in the thermal expansion data.

Fig. 4.1. The $Fe_{81}Ga_{19}$ sample has extremely low magnetostriction, but it has an anomalous maximum in its value at 370K, indicating a transition not reflected at all in the thermal expansion data. The $Fe_{74}Ga_{26}$ sample may be exhibiting a high temperature transition near 370K as well, but the limits of the instrumentation make this difficult to interpret. No such phenomena are seen in the $Fe_{82}Ga_{18}$ sample.

All alloys but the $Fe_{74}Ga_{26}$ composition exhibit anomalous magnetostriction at room temperature, shown in Figure 4.4.The $Fe_{74}Ga_{26}$ alloy was also the only composotion not subject to homogenization and quenching/slow cooling, which could account for it being the only material with typical Joulian behavior. The $Fe_{83}Ga_{17}$ and $Fe_{78}Ga_{22}$ alloys have near zero λ_{010}, and the linear approach to saturation in $Fe_{78}Ga_{22}$ suggests twin boundary motion, which has been modelled for FSMAs [37]. It has been demonstrated that FeGa alloys exhibit large variation in values of Poisson's ratio for $\langle 110 \rangle$ directions as a consequence of their magnetic properties [25, 38, 39], and this could account for the anomalous positive response for $\lambda_\perp$ in the $Fe_{81}Ga_{19}$

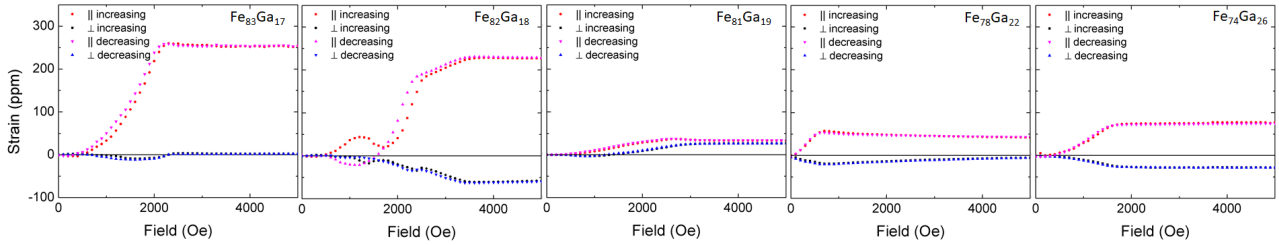

Figure 4.4: Magnetostriction measurements taken at room temperature showing both $\lambda_{\parallel}$ and $\lambda_{\perp}$ for $Fe_{100-x}Ga_x$ alloys ($x = 17$, 18, 19, 22, and 26). The 17, 18, and 22 at. % Ga single crystal alloys had strain gauges along [100] and [010] directions, and all exhibit non-Joulian magnetostriction. Both $Fe_{83}Ga_{17}$ and $Fe_{78}Ga_{22}$ show $\lambda_{010} \approx 0$ at saturation. The $Fe_{82}Ga_{18}$ alloy shows very unusual non-linear behavior and transitions to linear responses at 2300 Oe along both directions before saturation. The $Fe_{81}Ga_{19}$ alloy show positive transverse magnetostriction which is atypical of polycrystals. Only the $Fe_{74}Ga_{26}$ sample shows Joulian behavior.

alloy. There's also the possibility of abnormal grain growth of $\langle 110 \rangle$ texturing during the heat treatment, as seen in FeGa alloys studied by Na and Flatau [40–42]. This could explain the positive transverse striction as a $\lambda_{1\bar{1}0}$ response. We adhered the strain gauge to this $Fe_{81}Ga_{19}$ sample without regard to any known direction under the assumption of non-textured polycrystallinity, which would mean that the arbitrary placement coincidentally lay along an unknown [110] texturing, a possibility we did not verify for this alloy. The $Fe_{82}Ga_{18}$ alloy has mixed quadratic and linear characteristics in its magnetostrictive response, which suggests perhaps both classical and twin-boundary movement responses contribute to the overall behavior at different field strengths. The $Fe_{82}Ga_{18}$ sample sees this initiate near 2300 Oe, but it is unknown what crystallographically and microstructurally may be occurring to produce this magnetoelastic response. The process is reversible, indicating the response demagnetizes the sample completely, in accordance with the magnetization behavior. A plot of the magnetostriction values for $Fe_{82}Ga_{18}$ at an intermediate

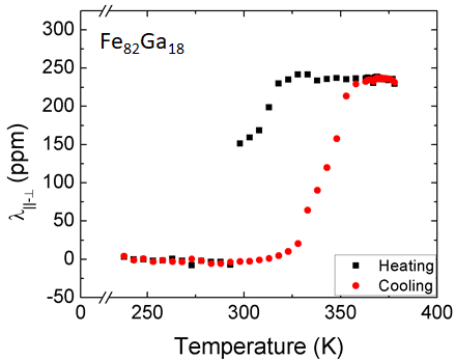

Figure 4.5: Magnetostriction values ($\lambda_{\parallel} - \lambda_{\perp}$) obtained with an applied field of 1500 Oe plotted as a function of temperature for an $Fe_{82}Ga_{18}$ alloy. This data shows a clear transition in intermediate magnetostriction values with temperature variation that does not appear at all in the saturation magnetostriction values versus temperature.

field of 1500 Oe, seen in Figure 4.5, reveals an anomalous transition near 325 K not captured by the $\lambda_{\parallel-\perp}(T)$ plot. There's a large hysteresis between the values obtained during the heating cycle as opposed to the cooling cycle for this alloy, but at no point do the individual magnetostriction curves, not shown, indicate a loss of reversibility for the sample at any temperature.

We carried out torque measurements as a function of field on the $Fe_{82}Ga_{18}$ sample in the attempt to probe structural characteristics indirectly and to gain a better understanding of the origin of these magnetostrictive transitions. Reference curves are shown in Figure 4.6 at low, intermediate, and saturation fields. Similar to FePd, the torque possesses only 2-fold symmetry at lower fields, and a 4-fold symmetry manifests at intermediates fields and ultimately comes to dominate the torque. Unlike FePd, however, the 2-fold symmetry component exhibits hysteretic switching between forward and reverse measurements, a phenomena corresponding to an anisotropy response of hard, uniaxial magnetic materials like $CoFe_2O_4$ [43,44].

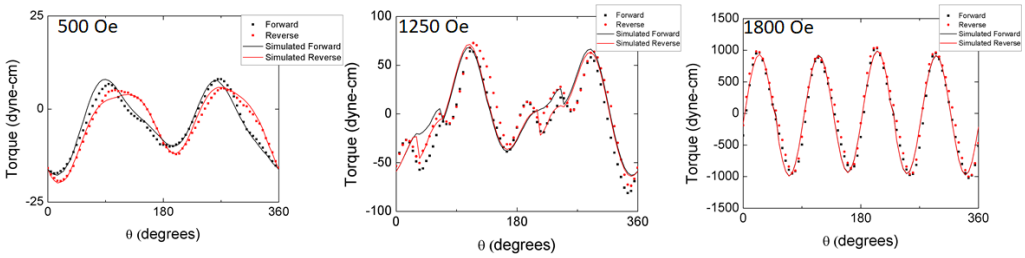

Figure 4.6: Magnetic Torque measurements of $Fe_{82}Ga_{18}$ taken at 500, 1250, and 1800 Oe. Contrary to the magnetization, hysteresis appears corresponding to a 2-fold uniaxial symmetry within the magnetic torque data at the low and intermediate field values 500 and 1250 Oe before cubic 4-fold symmetry dominates the signal at the higher field of 1800 Oe near saturation.

The presence of this uniaxial switching means the $Fe_{82}Ga_{18}$ sample is not single crystalline but two-phase. The curves in Fig. 4.6 have fitted lines constructed from a model superposing cubic (4-fold), uniaxial (2-fold), and shape anisotropy (2-fold) through the following expression:

$$L_{total}(\theta) = N_{cubic}\sin(4\theta) + N_{uniaxial}\sin(2(\psi_0(\theta) - \theta_{uniaxial})) + N_{demag}M^2\sin(2(\theta - \theta_{demag})) \tag{4.1}$$

where L_{total} describes the total value of the anisotropy for a given applied field angle, θ, N_{cubic} is the amplitude of the cubic anisotropy component, $N_{uniaxial}$ is the amplitude of the uniaxial anisotropy component, N_{demag} is the demagnetization factor of the sample, M is the sample magnetization at the applied field strength, $\theta_{uniaxial}$ is the phase difference between the uniaxial and cubic components, and θ_{demag} is the phase difference between the cubic and shape anisotropy components. To capture the switching behavior of the uniaxial component, equilibrium magnetization angles, $\psi_0(\theta)$ are determined by minimizing the anisotropy and Zeeman energy with respect to the uniaxial phase's own magnetization angle, ψ, which does not follow

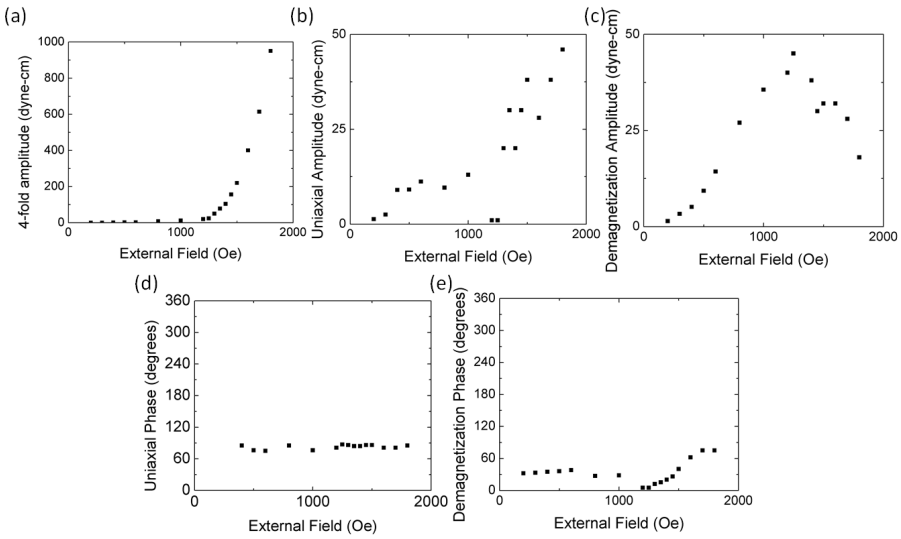

Figure 4.7: Several values as a function of field extracted from modelling the magnetic torque curves of $Fe_{82}Ga_{18}$ with eq. 4.1, including **(a)** N_{cubic}, **(b)** $N_{uniaxial}$, **(c)** $N_{demag}M^2$, **(d)** $\theta_{uniaxial}$, and **(e)** θ_{demag}.

the angle of the applied field as the sample is magnetized along its hard axes below a critical field value [44]. This minimization corresponds to two solution sets for the equilibrium angle, which accounts for the hysteresis observed in the forward and reverse measurements. Further details of this modelling are contained in Appendix E.

The model was used to track the response of the different anisotropy components as a function of field, shown in Figure 4.7. Most notably, the shape anisotropy behavior shows very anomalous results after the cubic phase begins to manifest. Shape anisotropy is proportional to the square of the sample magnetization, as expressed in eq. 4.1, which holds true up to 1000 Oe, but at higher fields it shows a steady decrease. Furthermore, the phase of the shape anisotropy, which depends only on the sample geometry and thus should not show field dependence, begins to change as a function of field after 1000 Oe. Shape anisotropy originates from

the slight ellipticity of circular samples, causing preferred magnetization directions along one axis over its transverse counterpart. The factor N_{demag} is determined by the difference in length between these axes, $N_{\parallel} - N_{\perp}$, and the magnitude of the shape anisotropy at 1000 Oe has an energy of $\sim$140 J/m^3, corresponding to a demagnetization of approximately 0.00342. This represents an ellipticity of $\sim$0.24 % or roughly 20 μm around the disk perimeter. The magnetostriction, in comparison, introduces a 4 μm variation around the disk parameter, so it is believed that the magnetostriction is responsible for the departure of both the amplitude and phase of the shape anisotropy from typical behavior.

The critical field at which the uniaxial hysteresis is overcome is determined by the uniaxial anisotropy constant and magnetization through the relation $H_k = 2K_u/M_s$ [44]. The critical field extracted from the modelling is 2300 Oe, which corresponds to a uniaxial anisotropy of $\sim$ 1.66 $\times 10^6$ J/m^3. This field value matches the same field strength where the magnetostriction behavior of $Fe_{82}Ga_{18}$ switches from quadratic to linear behavior as well, which could imply exceeding this critical field activates a mangetostrictive effect of the uniaxial phase. Considering the magnitude of the uniaxial anisotropy, which exhibits an amplitude of 46 dyne-cm or 183 J/m^3 in the actual data, one can obtain a volume fraction estimate of $\sim$0.11 % for this uniaxial phase.

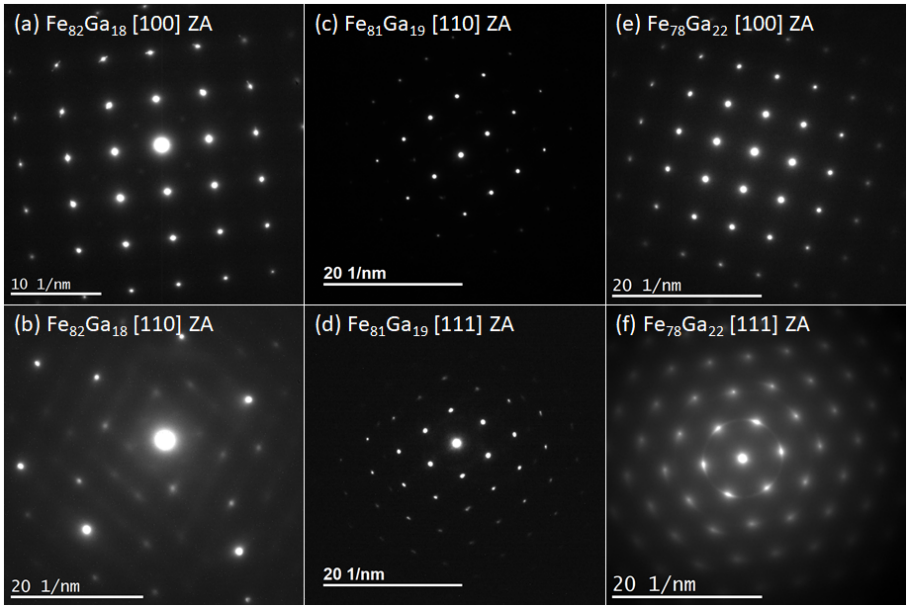

Figure 4.8: Diffraction patterns obtained for an $Fe_{82}Ga_{18}$ alloy along **(a)** [001] and **(b)** [011] zone axis, an $Fe_{81}Ga_{19}$ alloy along **(c)** [110] and **(d)** [110] zone axes, and an $Fe_{78}Ga_{22}$ alloy along **(e)** [001] and **(f)** [111] zone axes.

4.2 TEM Studies of FeGa

The extremely small volume fraction for a uniaxial magnetic phase within the $Fe_{82}Ga_{18}$ sample meant bulk diffraction probes could not be trusted to provide accurate structural information for the sample, and most likely other samples. Thus, TEM measurements have been carried out on [100] and [110] slices of $Fe_{82}Ga_{18}$, [100] and [111] slices of $Fe_{78}Ga_{22}$ alloys, and sample cut of arbitrary orientation from polycrystalline $Fe_{81}Ga_{19}$. Characteristic diffraction patterns are shown in Figure 4.8 for the respective zone axes of the slices from $Fe_{82}Ga_{18}$ and $Fe_{78}Ga_{22}$. The dominant phases apparent in both alloys are A2 (disordered-BCC) and $D0_3$ (ordered BCC), with $a_{A2} \approx 2a_{D0_3}$, and no clear evidence of twinning in any of these patterns can be seen. The near-equivalent lattice parameters of these two structures make

separation of their contribution to the diffraction patterns difficult; only the fact that ordering in $D0_3$ permits otherwise forbidden reflections for the A2 structure in $h+k+l$ =odd values lets one understand both phases are present. For the [111] zone axis, distinctions between the two structures is impossible, seen in Fig. 4.8d and 4.8f. It can be seen that the $Fe_{81}Ga_{19}$ pattern appears to have brighter, less diffuse $D0_3$ reflections than that of $Fe_{82}Ga_{18}$, such that it must possess a large volume fraction of $D0_3$ through its bulk, as one would expect from the phase diagram. The $Fe_{78}Ga_{22}$ alloy also possesses faint ring-like patterning for the $\langle 110 \rangle$ reflections, indicating the alloy may not be as single crystalline or homogeneous as determined by the manufacturer of the material. The $Fe_{82}Ga_{18}$ crystal demonstrates heavily diffuse streaking along $\langle 211 \rangle$ directions in its [011] zone axis pattern as well as non-uniform intensity distribution among its many reflections, which may be interpreted as twin-like distortions for a BCC crystal, but evidence of these structures was not seen in any micrographs.

In order to attempt to distinguish the $D0_3$ phase from the A2 in these materials, dark field imaging was attempted for $[200]_{A2}$ and $[100]_{D0_3}$ reflections, shown in Figures 4.9 for $Fe_{82}Ga_{18}$ and 4.10 for $Fe_{78}Ga_{22}$. In both cases, dislocations were nowhere found throughout the bulk of the TEM samples; bright spots highlighted by the technique seem to indicate the presence of substantial precipitates nanoscopic in size towards the edges. The nanoscopic size of these precipitates requires extremely thin portions of the samples to even observe their presence, which explains why they resolve most clearly near the thin edges of the samples.

High resolution (HR) imaging for the alloys are shown in Figures 4.11, 4.12,

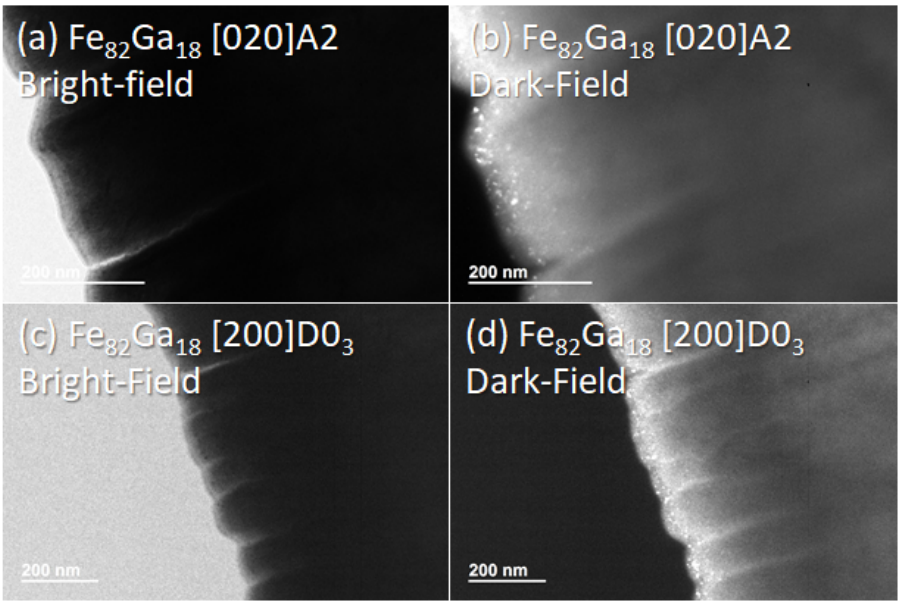

Figure 4.9: **(a)** Bright field and **(b)** dark field images TEM micrographs taken under two-beam conditions for a [020]A2 reflection in [001] oriented $Fe_{82}Ga_{18}$ sample. **(c)**Bright field and **(d)** dark field TEM micrographs taken under two-beam conditions for a [100] $D0_3$ reflection in the same [001] oriented $Fe_{82}Ga_{18}$ sample. Btoh dark field images illuminate a distribution of nano-sized precipitates towards the thinner edge of the sample.

and 4.13. Both samples can be seen to possess a curious texturing at lower magnifications which seems to be caused by the presence of these nanoscopic precipitates. Upon closer inspection, one sees this contrast definitely comes not from thickness, stress, or compositional variation, but by the presence of an extremely large amount of nanoscopic crystallites misoriented with respect to each other, best seen in highest magnification images from the figures. The crystallites average around 5 nm in size, and their overlap also gives rise to Moiré fringes in certain places. Phase identification of these precipitates, as well as twinning, are hard to evaluate, and as it stands, Fourier analysis cannot overcome the signal-to-noise ratio to clearly identify to what extent these precipitates are $D0_3$ or A2.

One thing that is clear is that neither of the $Fe_{82}Ga_{18}$ or $Fe_{78}Ga_{22}$ alloys are

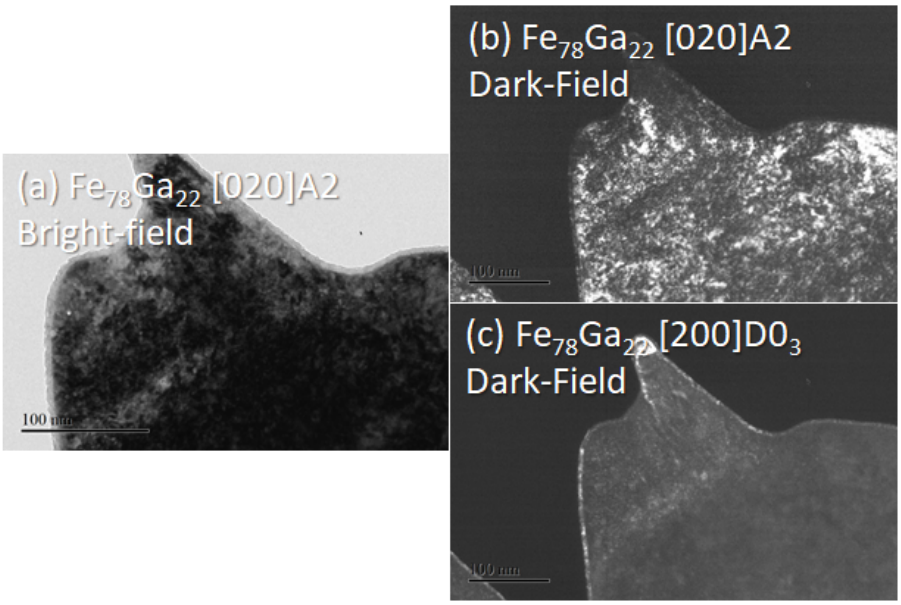

Figure 4.10: **(a)** Bright field TEM micrograph under two-beam conditions for a [020]A2 reflection of a [001] oreinted $Fe_{78}Ga_{22}$ sample, along with dark field micrographs under **(b)** [020]A2 and **(c)** [200]$D0_3$ two-beam conditions. These images again illuminate a distribution of nano-sized precipitates.

single crystal, but the extent to which these precipitates are distributed in the bulk is also unknown. Even the polyrcrystalline $Fe_{81}Ga_{19}$ possesses nanocrystallites within the bulk of single crystalline grains. Because the grains average roughly 5 nm in size, one cannot resolve them properly once the sample thickness exceeds this dimension. The diffraction pattern, too, tends to become dominated by an A2 single crystal pattern if it is taken from thicker areas, which could cause one measuring the phase via XRD or neutron diffraction to assume the samples are both single-phase, single crystal. An example of this is shown for $Fe_{81}Ga_{19}$ in Figure 4.14, which displays [110] zone axis diffraction patterns obtained over the same area using an aperture 1 μm in diameter versus 0.15 μm in diameter. The second pattern shows a much greater enhancement of $D0_3$ reflections from the smaller area, as well as numerous off-axis reflections around the transmitted beam corresponding to the variety of

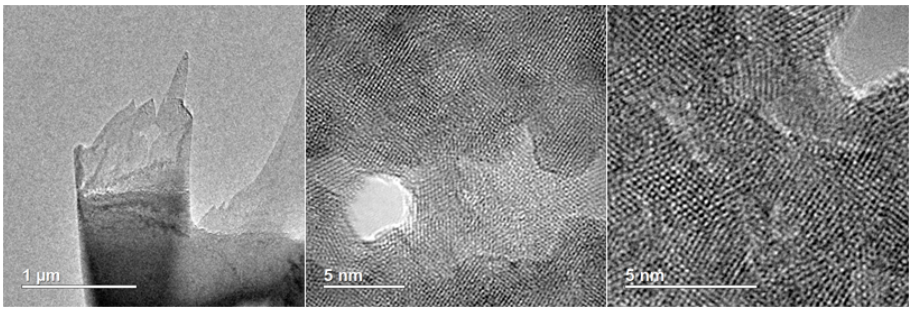

Figure 4.11: A series of high contrast images taken of an $Fe_{82}Ga_{18}$ alloy at several different magnifications, up to higher resolution using a JEM2100FEG TEM.

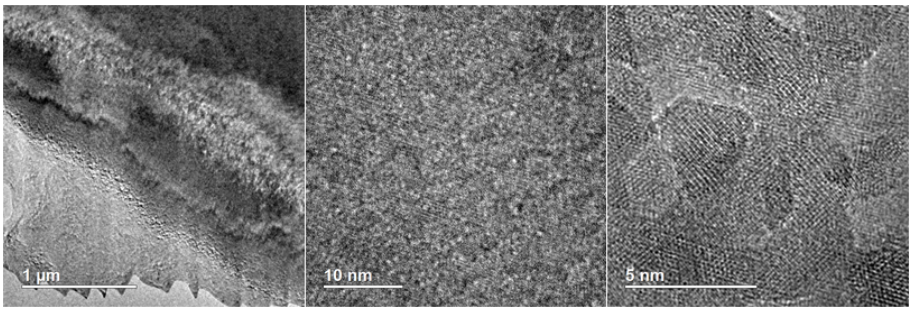

Figure 4.12: A series of high contrast images taken of an $Fe_{81}Ga_{19}$ alloy at several different magnifications, up to higher resolution using a JEM2100FEG TEM.

orientations the nanocrystallites possess. The local structure for these alloys now must be understood as a heterogeneous two phase mixture of A2 and $D0_3$. It could be perhaps that single crystal growth causes some degree of texturing, but this remains an open question.

The key to understanding the magnetoelastic mechanisms for large magnetostriction in these alloys must then involve local diffraction probes of the alloys as a function of field. All results shown thus far were taken at high magnification in TEM, which necessitates maintaining a high current in the objective lens, placing the sample in a field of approximately 3.15 T. Thus, most images correspond to the structural state of the sample close to magnetic saturation. Preliminary attempts to obtain patterns at lower objective lens voltages (V_{OL}s) of a JEOL 2100 LaB_6

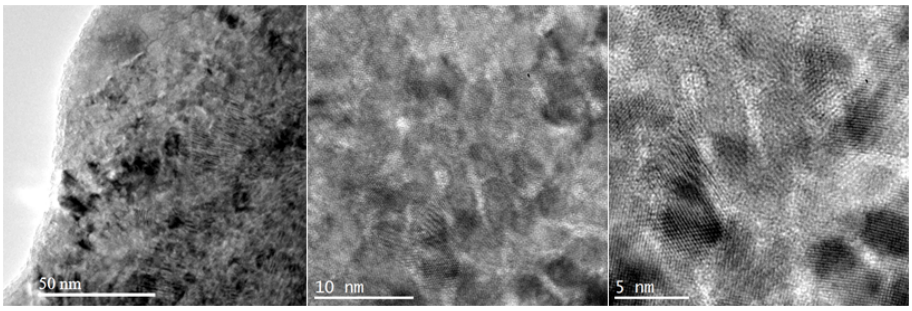

Figure 4.13: A series of high contrast images taken of an $Fe_{78}Ga_{22}$ alloy at several different magnifications, up to higher resolution using a JEM2100FEG TEM.

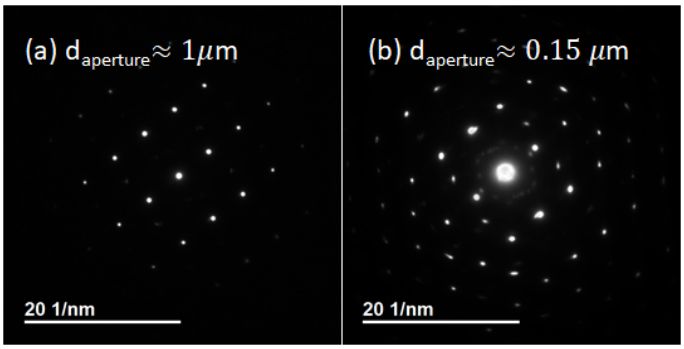

Figure 4.14: Selected Area Diffraction patterns taken of the same area in $Fe_{81}Ga_{19}$ using a **(a)** 1 μm size aperture and **(b)** 0.15 μm size aperture. The use of a smaller aperture leads to enhanced brightness in off-axis reflections showing the distribution in orientation amongst nanocrystallites.

TEM for the $Fe_{78}Ga_{22}$ sample are shown in Figure 4.15, with corresponding HR images in Figure 4.16. Lowering the objective lens lowers the magnetic field surrounding the sample, and we fabricated a Hall Probe to measure the field inside the TEM to assess the magnitude of the field changes. Despite the relatively small decrease in field, one can see the local structure changes drastically, with a large broadening of the A2 reflections, sharpening of the $D0_3$ reflections, and emergence of a significant distribution of differently oriented crystallites for both phases. The HR images focus on a single grain with inset fast Fourier transforms (FFT) to give an approximate look into reciprocal space for the crystallite. The crystallites lattice

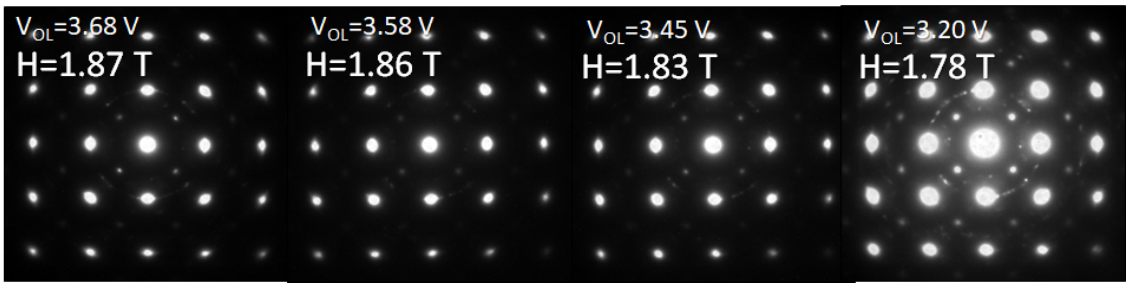

Figure 4.15: A series of selected area diffraction patterns taken over a roughly 150 nm diameter circular area for an $Fe_{78}Ga_{22}$ alloy at different strengths of objective lens voltage using a JEOL 2100 LaB_6 TEM. The sensitivity of the magnetic field reported is 0.1 mT. Lowering the field yields brighter $D0_3$ reflections and shows crystalline reorientation through emergence of differently rotated [001] zone axis reflections.

planes appear to go through severe distortions as V_{OL} decreases; the FFTs attest to a rhombohedrally distorted symmetry that forms twin-like reflection patterns at $V_{OL} = 3.68$ V and $V_{OL} = 3.45$ V. These interpretations are not definitive, however, as lowering V_{OL} changes alignment and focus conditions in ways unaccounted for. Below $V_{OL} = 3.20$ V, it becomes impossible within the limitations of the microscope to move the sample back to the image plane for focus.

Similar measurements were conducted on a $Fe_{82}Ga_{18}$ and $Fe_{81}Ga_{19}$ samples using a JEOL 2100 FEG TEM, which has considerably improved resolution than that of the LaB_6 due to the nature of the electron source [45], and those results are shown in Figures 4.17 and 4.18 for the 18 % alloy and Figures 4.19 and 4.20 for the 19 % alloy. Just as in $Fe_{78}Ga_{22}$ even the slight lowering of the field from 3.15 to 3.07 T, a difference of about 0.08 T or 800 Oe, causes a substantial change in intensity of reflections corresponding to the $D0_3$ phase for both alloys. The high resolution images in Figs. 4.18a-d and 4.20a-d are all of the same area for their respective sample, but locally the structure appears to vary as the field decreases. This may be

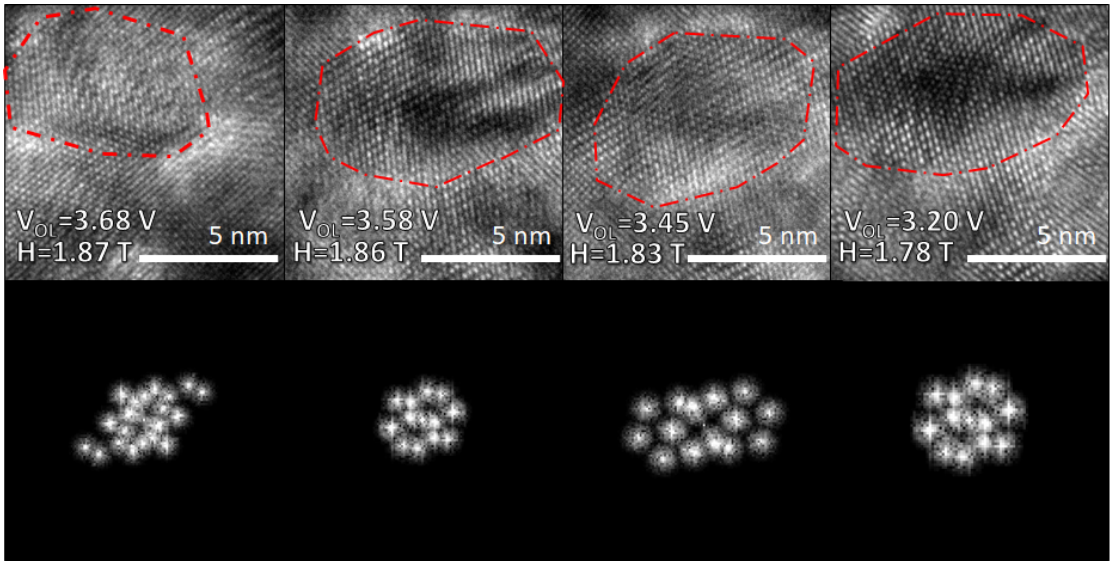

Figure 4.16: A series of high resolution images for a single 5 nm-sized crystallite in an $Fe_{78}Ga_{22}$ alloy at different strengths of objective lens voltage. The sensitivity of the magnetic field reported is 0.1 mT. The nanocrystallite region in consideration is highlighted in red, with fast Fourier transforms of the nanocrystallite region shown below, exhibiting different reflections as the field decreases. This suggests the crystallite reorients its structure in response to the field.

due to changes in focusing caused by re-alignment after each incremental decrease in V_{OL}, so filtered images were prepared in Figs. 4.18e-h and 4.20e-h by applying an artificial mask on the $D0_3$ [100] reflection in the Fast Fourier Transforms (FFTs) of the parent images. This FFT-filtering enhances the contrast for portions of the image that contribute to the intensity of the reflections, and therefore the regions where wave-like striations appear clearest correspond to regions of local $D0_3$ ordering. The size and location of these regions varies greatly in the $Fe_{82}Ga_{18}$ sample, where one can see a larger cluster of $D0_3$ orientation break into three pieces between the 3.10 and 3.07 T field increments in Fig. 4.18g and h. The interface between the light contrast in the edge of the sample and darker contrast of a 111 oriented portion of the crystal appears to shift greatly between the 3.12 and 3.10 T incre-

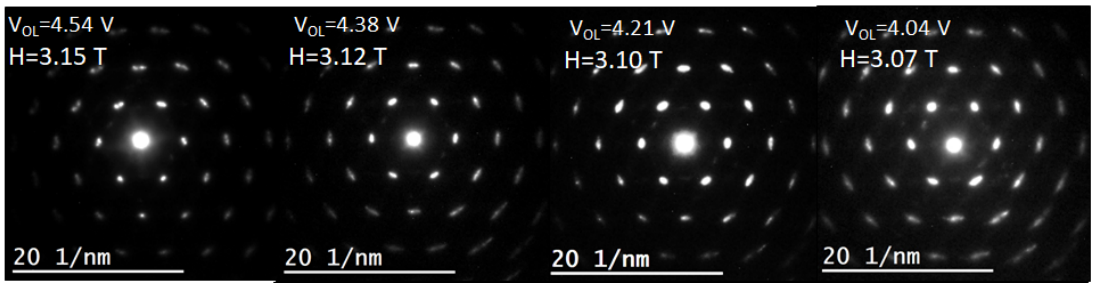

Figure 4.17: A series of selected area diffraction patterns taken over a roughly 150 nm diameter circular area for an $Fe_{82}Ga_{18}$ alloy at different strengths of objective lens voltage. The sensitivity of the magnetic field reported is 0.1 mT. These patterns also show brighter $D0_3$ reflections and the emergence of new reflections as the field decreases.

ments as well (Fig. 4.18f and g), further demonstrating wide-spread reorientation of the nanocrystalline regions. In the $Fe_{81}Ga_{19}$ sample, one sees a large spread of such clusters near 2.5 nm in size at 3.15 T (Fig. 4.20e), but at 3.07 T (Fig. 4.20e), the clusters appear larger and even spread across a much larger sized area of ∼10 nm.

The use of SAD allows one to see clearer diffraction information from the 5 nm-sized crystallites, but it is of interest to characterize the structure of individual grains that differ to some extent from the overall diffraction patterns obtained within the 150 nm diameter aperture probe. Thus, we employed NED in a JEOL 2100 FEG TEM under scanning conditions (STEM) to condense the electron beam to probe sizes of 1 nm or less. The beam probes in NED are completely coherent due to the use of a converged electron beam acting as an idealized point source of scattering at the sample surface [46–48], and its usage necessitates a very thin area of sample to limit dynamical scattering events which lead to incoherence. The usage of the technique for non-saturated V_{OL} is not documented in the literature, but operating in STEM mode allows for decreases in V_{OL} to be compensated by adjustment of the

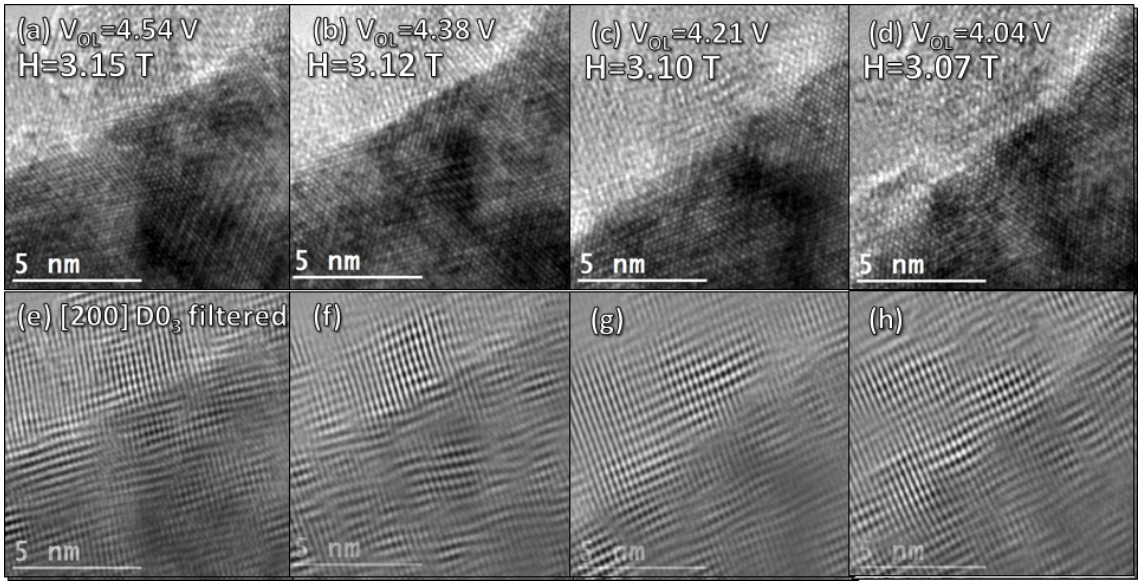

Figure 4.18: A series of high resolution images **(a-d)** of the same area within an $Fe_{82}Ga_{18}$ alloy at different strengths of objective lens voltage. The images **(e-h)** show enhanced contrast areas contributing to $D0_3$ [100] reflections in the Fast Fourier Transforms of images **(a-d)**, obtained through filtering software in Digital Micrograph. The images shows substantial displacement of a light/dark contrast interface that suggests large reorientation between field values of **(b)** 3.12 and **(c)** 3.10 T. The FFT-filtered images show regions of local $D0_3$ orientation shifting as the field decreases.

CL3 condenser lens to readjust the movement of the focal plane back to the plane of the screen or CCD camera [49], thereby permitting diffraction data to be collected at substantially lower magnetic fields.

Examples of patterns as well as dark fields images obtained for an $Fe_{82}Ga_{19}$ sample through NED are shown in Figure 4.21. The compensation of the CL3 lens while lowering V_{OL} allows dark field images to remain in focus and permit accurate placement of the beam in the same position of the sample to ensure the same structure is being measured throughout. Scale bars are intentionally removed from the images, as the various adjustments to lens voltages make calibrations difficult. The diffraction patterns at the low end of V_{OL} show significant distortions in various

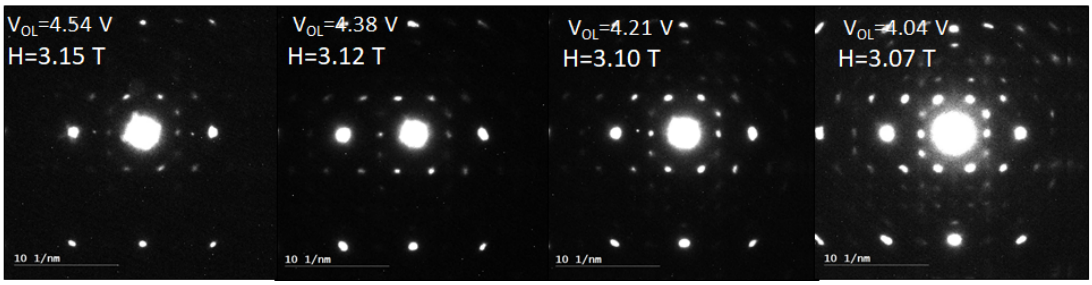

Figure 4.19: A series of selected area diffraction patterns taken over a roughly 150 nm diameter circular area for an $Fe_{81}Ga_{19}$ alloy at different strengths of objective lens voltage. The sensitivity of the magnetic field reported is 0.1 mT. These patterns also show brighter $D0_3$ reflections and the emergence of new reflections as the field decreases.

cubic reflections in $Fe_{82}Ga_{18}$, meaning exact interplanar distances at lower objective lens voltages are difficult to measure. While not shown, calibrations were first attempted on single crystal Si as proof of concept, but even in Si the distortions at lower V_{OL} cannot be overcome. Below a V_{OL} of 1.92 V, obtaining usable NED patterns for the FeGa samples became extremely difficult, and thus the measurements on these samples were carried out only from 4.54 V, the nominal operating voltage, to 1.92 V in intervals of approximately 0.155 V. The calibration between V_{OL} and the magnetic field in the instrument is contained in Appendix E, which corresponds to a field range of 2.38 to 3.15 T. Because the FIB samples are fabricated with dimensions of approximately 20 μm $\times$ 5 μm $\times$ 0.01 μm, the demagnetization factor of the sample out of plane, or along the direction of the field inside the TEM, is approximately equal to 1. This means the demagnetization field of the sample is approximately twice that of the samples' saturation magnetization, which comes to about 3.64 T based on a magnetization of 185 emu/g. The samples therefore are not fully magnetized in the TEM, and the NED probes the local structure from about

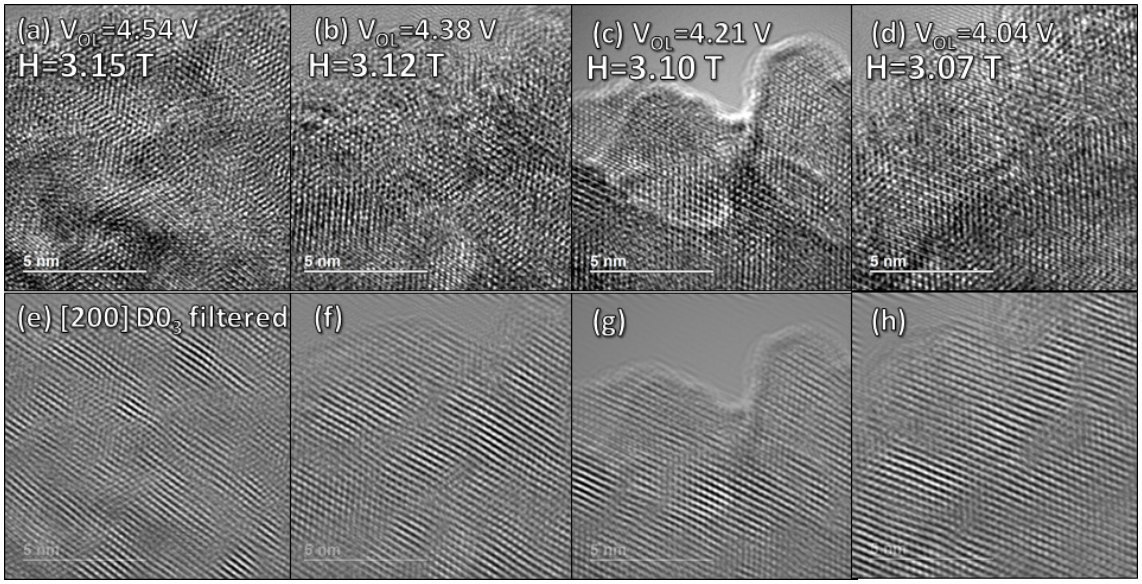

Figure 4.20: A series of high resolution images **(a-d)** of the same area within an $Fe_{81}Ga_{19}$ alloy at different strengths of objective lens voltage. The images **(e-h)** show enhanced contrast areas contributing to $D0_3$ [100] reflections in the Fast Fourier Transforms of images **(a-d)**, obtained through filtering software in Digital Micrograph. The FFT-filtered images show regions of local $D0_3$ orientation shifting as the field decreases.

65-85 % magnetization.

Because of inaccuracy in assessing lattice parameters, the presence of $D0_3$ was assessed through intensity comparisons of $D0_3$ forbidden reflections to those of A2+$D0_3$ reflections, which serve as a measure of the relevant volume fraction of $D0_3$ in probe. More details of this analysis are contained in Appendix E, but the results are shown in Figure 4.22. For the $Fe_{82}Ga_{18}$ and $Fe_{78}Ga_{22}$ samples, the $D0_3$ signal quickly decreases upon initial lowering of the field, and the 18 % sample shows a significant increase in signal at the intermediate values before shrinking back down at the lower end. The $Fe_{81}Ga_{19}$ sample shows little variation in $D0_3$ signal before exhibiting a decrease such as at lower fields seen in the other samples. The data demonstrates the $D0_3$ fraction does not remain stagnant, which could be an

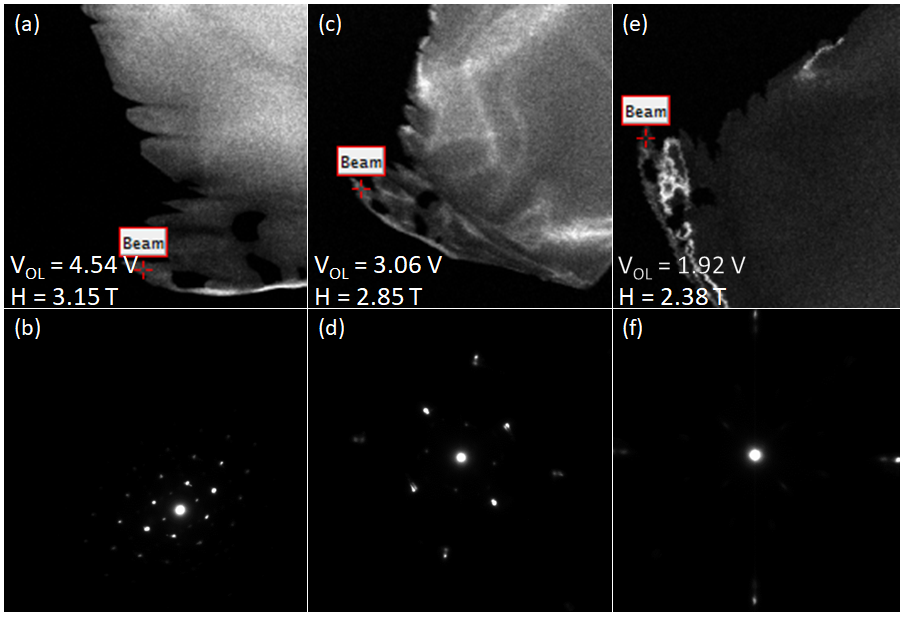

Figure 4.21: Dark field images and nanodiffraction patterns of an $Fe_{82}Ga_{18}$ crystal obtained in STEM mode taken at V_{OL} of **(a)** **(b)** 4.54, **(c)** **(d)** 3.06V, and **(e)** **(f)** 1.92 V. These images demonstrate the ability to keep a sample in focus and obtain nanoelectron diffraction patterns from the same location while decreasing V_{OL}.

indication of short-range ordering in response to the changing magnetic field. How and why this occurs is not exactly clear just from these measurements, since they suggest considerable atomic rearrangement through diffusive mechanisms must be responsible for the change in phase fraction of $D0_3$.

The $Fe_{81}Ga_{19}$ sample also exhibited twin-like [210] reflections for $D0_3$ crystals in the nanodiffraction patterns across $A2_{211}$ planes. These reflections had extremely defuse scattering across the $\langle 211 \rangle$ trace rather than isolated peaks. Analysis of this intensity as a function of field showed a dependence, and these results are shown in Figure 4.23. The measurements suggest not only does the fraction of $D0_3$ change with respect the to the field, but martensite variants thereof take place in twinning/detwinning mechanisms as well, pointing to a rather complex magnetization

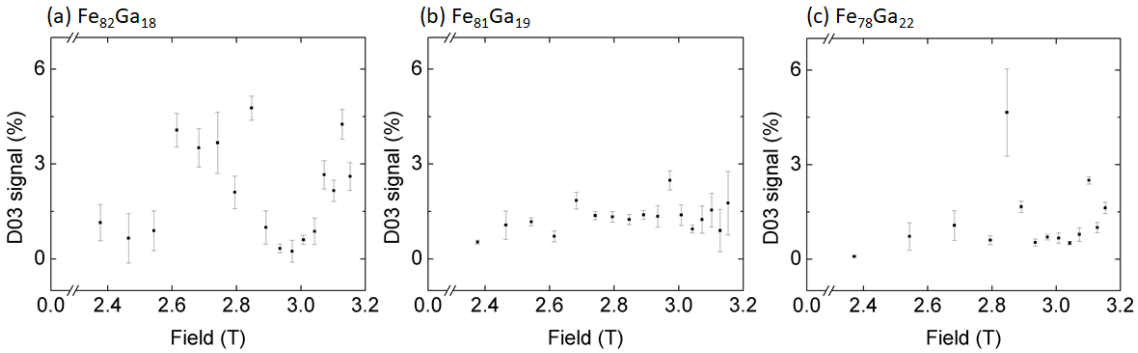

Figure 4.22: Plots of the $D0_3$ signal intensity versus magnetic field for **(a)** $Fe_{82}Ga_{18}$, **(b)** $Fe_{81}Ga_{19}$, and **(c)** $Fe_{78}Ga_{22}$ samples as analyzed through nanodiffraction patterns taken at each voltage. All three plots show variation in $D0_3$ reflection intensity with the field, with more drastic responses in the 18 and 22 at. % Ga alloys.

and magnetostriction response for the alloy.

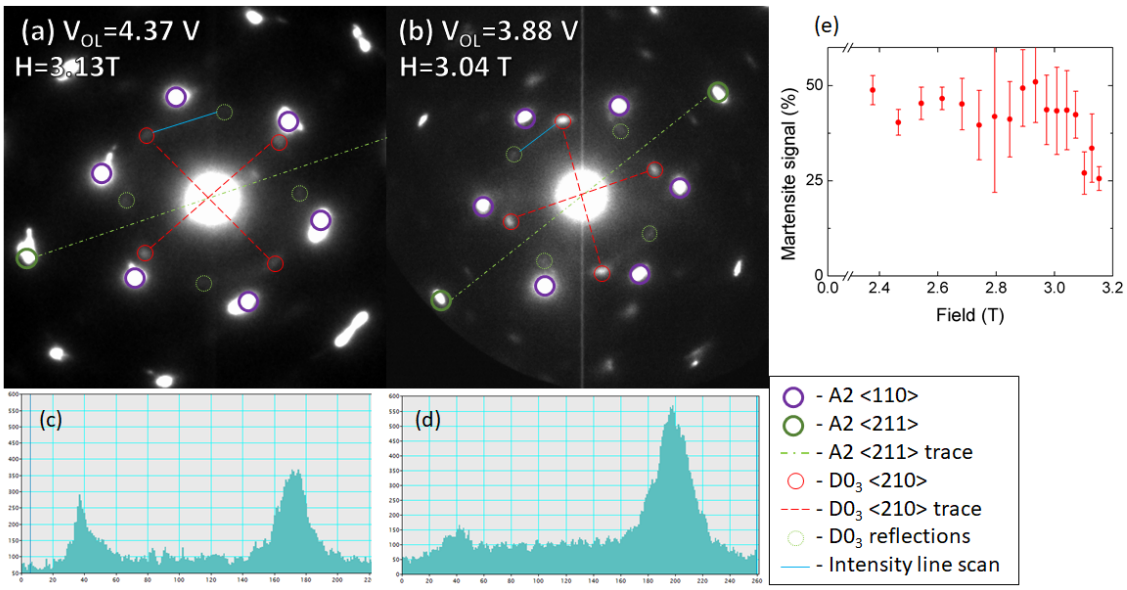

Figure 4.23: Nanodiffraction patterns collected for $Fe_{81}Ga_{19}$ at **(a)** 3.13 and **(b)** 3.04 T, with respective **(c)** and **(d)** intensitity line profiles along $\langle 211 \rangle$ directions across $\langle 210 \rangle$ $D0_3$ twin-reflections. The results of intensity analysis as a function of field for the twin reflection intensity compared to the stronger $D0_3$ is shown in **(e)**. This analysis suggests de-twinning occurs within $Fe_{81}Ga_{19}$ in response to the field.

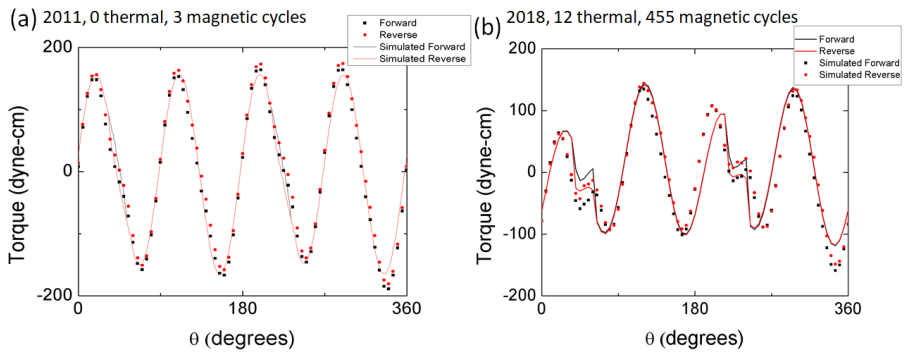

Figure 4.24: Magnetic torque measurements on the same $Fe_{82}Ga_{18}$ under a 1300 Oe applied field taken in **(a)** 2011 and **(b)** 2018, after an estimated 12 temperature cycles from 233 to 373 K and 455 magnetic cycles from zero field to saturation. A strong 2-fold uniaxial torque signal manifests in the latter data.

4.3 Evidence of Trained $Fe_{82}Ga_{18}$ Samples

The $Fe_{82}Ga_{18}$ alloy studied in these various measurements came from Ames Laboratory over 7 years ago as a single crystal rod homogenized at 1273 K for 72 h followed by 10 K/min slow cooling to room temperature. The various studies reported in this thesis lasted over the span of a year. Through this timeframe, it became clear that the same measurements repeated on the same samples started to yield different results, suggesting a form of training through growth of both $D0_3$ and tetragonal precipitates that was hitherto unanticipated. As such, the training history for the alloy cannot be exactly quantified, but it can be estimated based on the timeline of measurements taken. We classify training between either thermal cycling between 233 and 373 K as well as field cycling from 0 field to saturation, and the estimates for such cycles are reported in Table III.

Torque measurements carried out at 1300 Oe seven years ago are shown side-by-side with measurements taken at the same field this year for the same $Fe_{82}Ga_{18}$

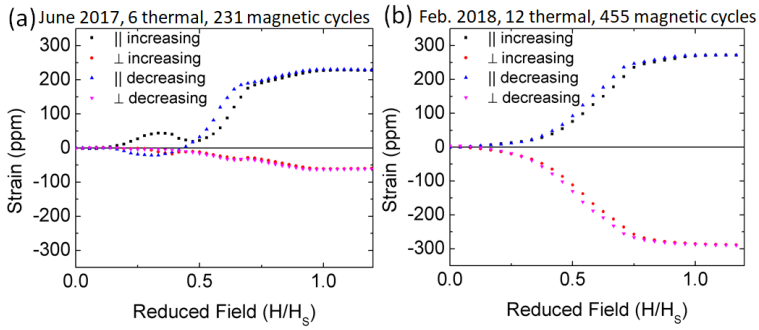

Figure 4.25: Room temperature magnetostriction curves measured on the same $Fe_{82}Ga_{18}$ sample in **(a)** June 2017 and **(b)** February 2018. The magnetostriction changes in non-linear response substantially and λ_{010} increases from -50 to -300 ppm to change the $\lambda_{\parallel-\perp}$ from 300 to 570 ppm after having gone through 6 additional temperature cycles from 233 to 373 K and 168 magnetic cycles from zero field to saturation.

disk in Figure 4.24. The sample would have undergone an estimated 12 thermal cycles and 455 magnetic cycles between these two measurements, and while the magnitude of the torque remained constant, the hysteretic switching attributable to a uniaxial tetragonal phase grew substantially, exhibiting approximately a 10× increase in magnitude from 5 to 50 dyne-cm.

Magnetostriction measurements taken eight months apart on the same sample also revealed a substantial increase in saturation, shown in Figure 4.25. The value of $\lambda_{\parallel-\perp}$ changed from 300 to 570 ppm, almost doubling in magnitude, after having undergone an estimated 6 thermal cycles and 224 magnetic cycles. One can see from the curve that this enhancement comes from a substantial change of the $\lambda_{010,\perp}$ response, and considered in tandem with the torque measurements, it may be attributable to the large increase in a tetragonal symmetry phase. Furthermore, the response at intermediate fields loses its unusual shape and becomes purely quadratic in nature before exhibiting linear behavior shortly before saturation. This could sug-

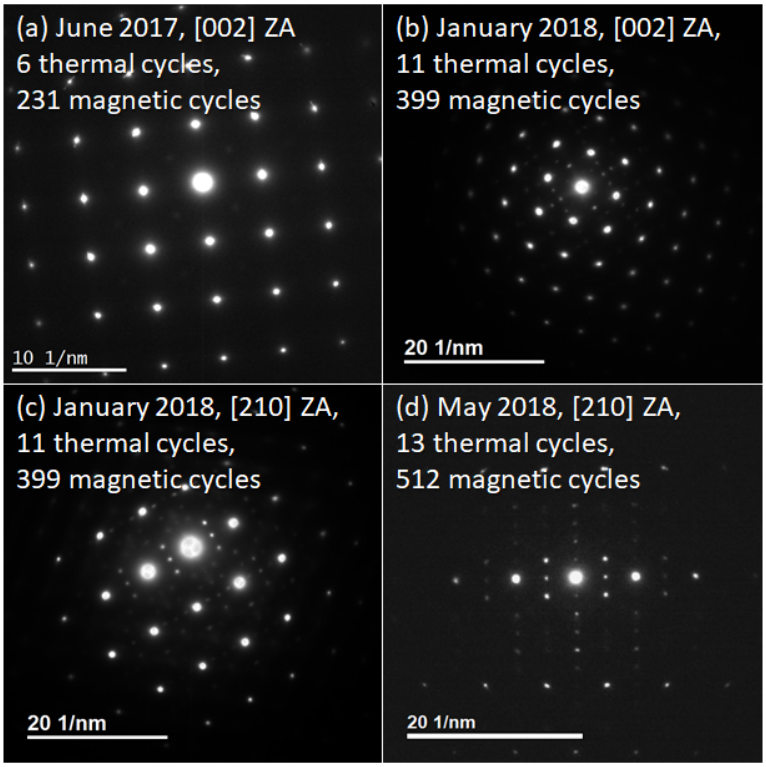

Figure 4.26: Several SAD patterns taken of $Fe_{82}Ga_{18}$ samples fabricated in June 2017 and January 2018 along **(a)** and **(b)** [002] zone axes and fabricated in January 2018 and May 2018 along **(c)** and **(d)** [210] zone axes. A greater number of [001] superlattice reflections emerges, which is attributable to a 6M martensite variant of $D0_3$ likely stabilized by the large amount of thermal and magnetic cycles reported in the patterns.

gest that the repeated magnetization cycles on the sample had the effect of trained specific growth of the tetragonal symmetry phase to select variants more favorably aligned in [100] and [010] directions.

TEM measurements were made on samples cut through FIB at different times: one in May 2017, one in January 2018, and one in May 2018, corresponding to cumulative thermal cycles of 6, 11, and 13 and cumulative magnetic cycles of 231, 399, and 512, respectively. Several SAD patterns are shown of these samples in Figure 4.26. Between June 2017 and January 2018, $D0_3$ spots grew in intensity,

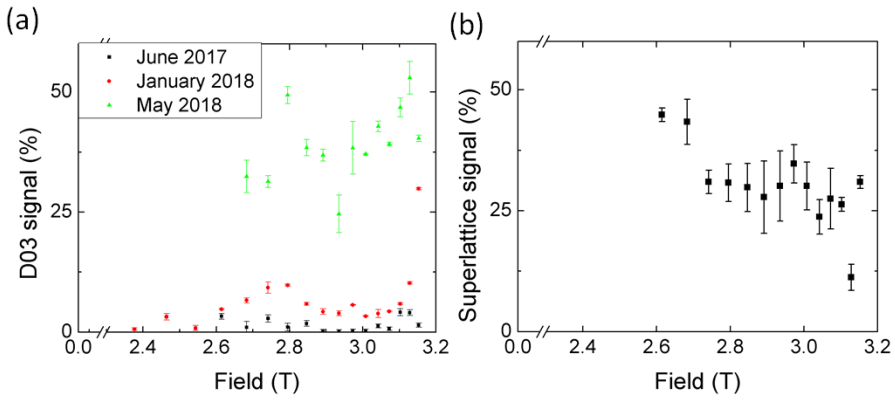

Figure 4.27: **(a)** The results of intensity analysis of NED patterns as a function of field for $Fe_{82}Ga_{18}$ FIB samples fabricated in June 2017 (6 thermal cycles, 231 magnetic cycles), January 2018 (12 thermal cycles, 399 magnetic cycles) and May 2018 (13 thermal cycles, 512 magnetic cycles), and **(b)** the variation in intensity of superlattice reflections as a function of field for the May 2018 sample. The data suggests that increased numbers of temperatures cycles from 233 to 373 K and magnetic cycles from zero field to saturation enhance $D0_3$ phase fraction and martensitic activity in the sample.

and in addition, superlattice reflections appear along $\langle 002 \rangle$ directions, which become even more apparent in diffraction on the January sample for a $[0\bar{1}2]$ zone axis. Such superlattice reflections were also observed for $Fe_{79}Ga_{21}$ along the same zone axis by Liu et al. and were identified as nano-modulated martensitic phase of $D0_3$ [33].The sample fabricated in May showed these same superlattice reflections, and it also demonstrated a significant tetragonal distortion with a c/a ratio of 0.823. However, this distortion was found only in a thin area of the sample, which exhibited a typical cubic SAD pattern when taken over the thicker bulk. The same NED analysis was performed on each sample, and the results are shown in Figure 4.27. Fig. 4.27b shows the change in the superlattice reflection intensity versus the field in the microscope. These results reveal a substantial increase in $D0_3$ intensity measured, yet demonstrate a similar response to the magnetic field within

each sample. The increase in superlattice intensity as the field decreased is similar to the change in martensite intensity observed in the $Fe_{81}Ga_{19}$ sample, which could be related to twinning/de-twinning processes as well. Magnetization remained unchanged throughout, but a larger fraction of $D0_3$ and martensitic behavior causes larger magnetostriction to manifest. With these results in mind, it is clear that such training in $Fe_{82}Ga_{18}$ occurs over the course of thermal (over ten) and magnetic field cycling (over several hundred) and must be accounted for when studying the magnetostrictive behavior.

Measurement	**Date**	**Cum. Thermal cycles**	**Cum. Magnetic Cycles**
[100] and [110] $M(H)$	2011	0 (as-prepared)	2
$L(H,\theta)$	2011	0 (as-prepared)	3
λ_{100}, λ_{110}	2011	0 (as-prepared)	5
[100] and [110] $M(H)$	May 2017	0	7
[100] $\varepsilon(T)$	May 2017	2	7
$\lambda_{100}(T)$ (four attempts)	June 2017	6	231
First FIB Preparation	June 2017	6	231
[110] $\varepsilon(T)$	June 2017	8	231
$\lambda_{110}(T)$ (three attempts)	July 2017	11	399
Second FIB Preparation	January 2018	11	399
$\lambda_{100}(T)$	February 2018	12	455
$L(H,\theta)$	February 2018	12	456
$\lambda_{110}(T)$	March 2018	13	512
Third FIB Preparation	May 2018	13	512

Table 4.1: This table enumerates the dates of different measurements performed on an $Fe_{82}Ga_{18}$ alloy, including room temperature magnetization $M(H)$, field-dependent magnetic torque $L(H,\theta)$, magnetostriction as a function of temperature $\lambda_{hkl}(T)$, thermal expansion $\varepsilon(T)$, and FIB-preparation for the samples for TEM studies. This results in estimated cumulative tallies for thermal cycling between 233 and 373 K and magnetic field cycling from 0 field to saturation over the course of those measurements.

Chapter 5: Summary and Outlook

5.1 Discussion of completed studies

The structural evidence observed in the TEM studies demonstrates these alloys possess much more complex microstructures than previously detailed in the literature. The majority of studies are performed on supposed single crystal alloys, but the TEM results of such single crystals such as the $Fe_{82}Ga_{18}$ and $Fe_{78}Ga_{22}$ alloys studied demonstrate that these alloys are polycrystalline at the nanoscale, exhibiting overall single crystal diffraction patterns in bulk probes which differ from the local structural data. There remains a possibility as to whether the preparation of samples through the FIB may have caused developed the nanocrystalline microstructures rather than reveal them. The use of a Ga-source focused ion beam carries risks of structural damage and Ga implantation at the nanoscale [45,51], but final thinning of the FIB samples was carried out in using low-energy, low current beam settings to minimize this risk. One would have to prepare further TEM samples of the crystals using conventional ion milling methods to assess the extent of FIB-related influence on the samples, which we elected not to carry out since doing so would render the specimen destroyed for any further analysis.

However, indications of nanocrystallinity within FeGa alloys can be inferred

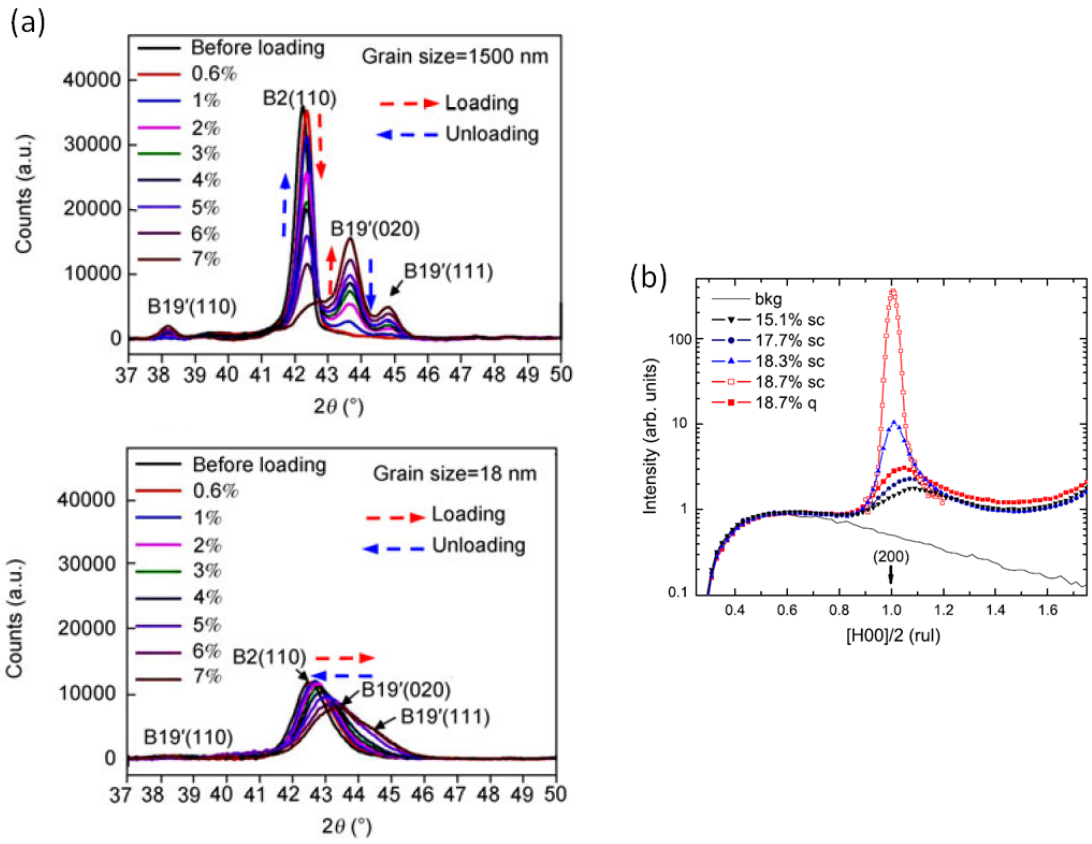

Figure 5.1: Taken from [50], **(a)** shows in situ applied stress XRD data taken on $Ni_{49.1}Ti_{50.9}$ polycrystals of 1500 and 18 nm grain sizes, and, taken from [22], **(b)** shows XRD data taken on single crystal FeGa alloys of different composition either slow-cooled (sc) or quenched (q) from 1273K. The broadening of the peaks is attributed to the nanocrystal grain size in **(a)**, and the cause of broadening in **(b)** was reported as unknown.

from past XRD and neutron diffraction results, which manifests through substantial broadening of major diffraction peaks due to larger amorphous volume fractions from increased grain boundary surface area, as well as increased stress transferred throughout the bulk of nanocrystals [50]. This has been demonstrated both in nanocrystal NiTi alloys [50], and XRD studies of single crystal FeGa conducted by Xing et al. in 2008 also show substantial peak broadening [22], with results taken from both papers shown in Figure 5.1 for illustration. Neutron diffraction exper-

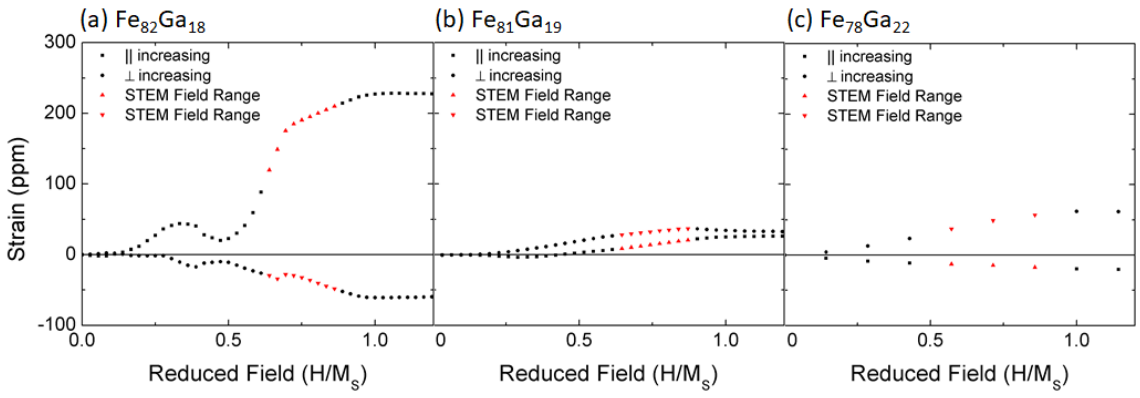

Figure 5.2: Room temperature magnetostriction plots for **(a)** $Fe_{82}Ga_{18}$ (June 2017), **(b)** $Fe_{81}Ga_{19}$, and **(c)** $Fe_{78}Ga_{22}$ plotted versus their internal magnetization with the range covered by the STEM NED analysis highlighted in red.

iments carried out by Laver et al. on quenched $Fe_{81}Ga_{19}$ single crystals provided evidence for the existence of $\sim$ 15 nm-sized tetragonal precipitates [23]. This supports the TEM results and suggests FIB-preparation revealed the nanocrystallinity rather than caused it.

Not only are the alloys nanocrystalline, but the TEM results also demonstrate the presence of A2, $D0_3$, and a martensite variant of $D0_3$ within the alloys. This martensite variant corresponds to an orthorhombic phase created by shear $\langle 110 \rangle$ stacking faults off the [100] projection in the sequence ABCBCBA, first classified as a rare 6M martensite found in ordered Cu_3(Al,Ni) alloys by Otsuka in the 70s and identified in FeGa alloys by Liu et al. last year [33,34,52]. Because of the large grain boundary volume fraction, one must also consider a substantial presence of an amorphous fourth phase.

The challenge now becomes to connect the microstructural characteristics of the different alloys to their magnetostrictive responses. With the existence of three crystalline phases and a substantial amorphous phase, low anisotropy, and unusual

magnetostrictive responses, one must conclude that the behavior for these particular materials is definitively non-Joulian. The phase fractions change in response to the field, seen through both the *in situ* high resolution TEM images and NED studies. To compare the magnetostriction to the NED analysis, Figure 5.2 shows the studied alloys' magnetostriction responses with the magnetic field range probed in the TEM highlighted in red. The 18 % Ga alloy has the most abnormal magnetostrictive behavior within this range, transferring from a quadratic-like response to a linear response, and during this transition one sees the $D0_3$ intensity peaks in Fig. 4.22a for the material. This suggests that the $D0_3$ may possibly possess a critical activation field after which it begins contributing more heavily to the magnetostriction, and this critical field may be tied to the 2300 Oe anisotropy field needed to overcome magnetic pinning within uniaxial precipitates. In the 19 % Ga alloy, the $D0_3$ does not show as much variation as the 18 % alloy in response to the field, but the twin reflections seen in the NED demonstrate the twinning/de-twinning processes may occur. This would explain the linear magnetostrictive behavior, which occurs as a de-twinning mechanism in FSMAs [37].The 22 % Ga sample showed a linear response as well, but the NED analysis did not reveal evidence of martensite or twins in this alloy. However, the preliminary *in situ* experiments shown in Figs. 4.15 and 4.16 demonstrated distortion and crystallite reorientation at the nanoscale, and the NED analysis showed variation of $D0_3$ signal intensity through this range. In addition, the NED analysis of the 22 % Ga sample had been done on a [100] zone axis, which would have not shown clear martensite or twin reflections, so it's possible the analysis overlooked these features. In addition, the 6M phase is orthorhombic, with

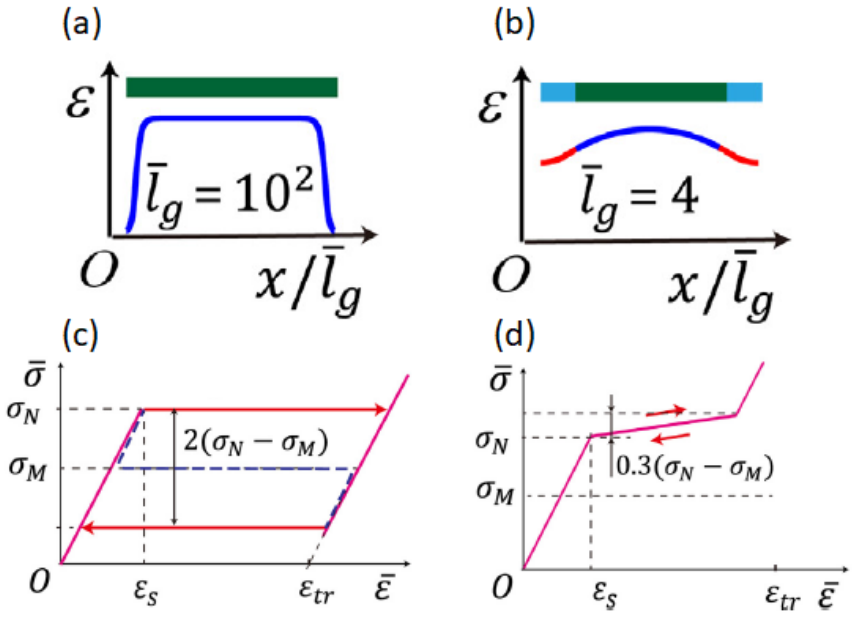

Figure 5.3: Taken from [53], **(a)** and **(b)** show strain profiles across the length of a stressed grain 100× and 4× larger than their grain boundary, respectively. The strain in **(b)** becomes smooth and less localized because the smaller grain cannot accommodate an austenite/martensite interface. **(c)** and **(d)** show corresponding stress-strain curves, demonstrating that hysteresis vanishes for the nanosized grain as well.

a larger c-axis of 13.364 $\AA$, and the small size of the nanocrystallites may prevent a sufficient diffraction signal to build up from coherent scattering of only few such planes.

The evidence makes clear that the microstructure and the mechanism of magnetostriction for these alloys is much more complex than previously believed, and these results therefore have serious implications towards accurate modelling of these materials. Brinson developed a method to evaluate the stress-strain characteristics of shape memory alloys as a function of temperature based on constitutive laws of thermodynamics and the kinetics of the transformation [54], and Kabir and Tehrani have demonstrated how one can use Brinson's model to capture the stress-strain

behavior of materials with varying volume fraction of a SMA phase [55]. Such techniques have also been extended to polycrystalline SMAs, which require resolving the applied stress onto differently oriented SMA grains, detailed in a microplane model by Brocca, Brinson, and Bazant in 2002 [56]. However, the nanocrystalline microstructure changes the mechanical responses of materials drastically, resulting in a loss of strength beyond a critical grain size due to enhanced slip shear and plasticity of the grain boundaries themselves [57]. Furthermore, it has been determined in recent years that nanocrystalline shape memory alloys lose hysteresis in their phase transformation below a critical size scale [50, 53]. Li and Sun demonstrated just this year how this is achieved through continuum mechanics modelling of nanocrystal NiTi as a core-shell structure with an SMA core and grain boundary as amorphous shell [53]. Their model takes into account the modulus of the grain, E, the grain boundary, E_g, the ratio of the grain size to its boundary, $\bar{l_g}$, the transformation strain, ε_{tr}, and the gradient strain energy α, and some of their results are shown in Figure 5.3. The main conclusions drawn from their work predict a critical grain size of 10 nm, below which hysteresis in the stress-strain curve vanishes and, in addition, the elimination of any possible two-phase coexistence. That is, the transformation cannot possibly introduce an austenite/martensite interface below a critical size of 40 nm, and the martensite develops in a second-order like fashion with increasing stress as a result. One can imagine this type of stress-strain behavior also has a magnetic equivalent by modelling the strain in response to an effective magnetic stress, and this could provide a valuable explanation for the lack of magnetic hysteresis in Fe-based FSMAs.

If these alloys possessed high magnetic anisotropy, one would expect to see large hysteresis reflected in the magnetization curves, and furthermore, one would see a substantial difference upon magnetization of an easy crystalline axis versus a hard one, i.e. [100] versus [111]. However, it may be the case that these FSMAs compensate for conventional magnetic anisotropy with their elastic softness, and that their nanocrystalline microstructure coupled with this softness allows them to reorient easily as well. The HRTEM results indicate that these nanoscopic precipitates distort easily in response to a magnetic field, and these distortions exhibit a unique magnetic response inherent to this class of materials. From Khachaturyan's PFM work [58], one understands that the martensite present in these systems is an adaptive response of each system to external stimuli in the form of its thermal and processing history as well as applied stress or magnetic field at constant temperature. His PFM work even extends towards understanding the growth of martensitic embryos in response to an applied magnetic field. Because the magnetic torque data suggests the martensite in FeGa possesses significant magnetic anisotropy, its magnetic response dictates the magnetization of the soft magnetic phases surrounding it within the material. From Khachaturyan [59], the magnetization of a single martensite embryo, $\mathbf{M}_p$, may be expressed as

$$\mathbf{M}_p = \mathbf{M}_p^0 \omega(\mathbf{H})_p \tag{5.1}$$

where the p uniquely identifies the embryo, M_p^0 is a constant magnetization density inherent to the martensite phase of the embryo, and $\omega(\mathbf{H})_p$ is the volume of that

embryo as a function of the applied field. This volume possesses a constant value in the demagnetized state, $\omega(0)_p = \omega_0$, and the volume will change to accommodate the field according to the following approximation:

$$\omega(\mathbf{H})_p = \omega_0 + \gamma(\mathbf{a}_p \cdot \mathbf{H}) \tag{5.2}$$

where $\mathbf{a}_p$ is a positioning vector corresponding to the p-th embryo and γ is a magnetoelastic coefficient linking the volume change of the particle with respect to the applied field. The total magnetization is then expressed by the sum of magnetizations for all such embryos:

$$\mathbf{M} = \sum_p \mathbf{M}_p^0 \omega(\mathbf{H})_p = \sum_p \mathbf{M}_p^0(\omega_0 + \gamma(\mathbf{a}_p \cdot \mathbf{H})) \tag{5.3}$$

In this expression, assuming a non-preferential orientation of embryos, the first term $\sum_p \mathbf{M}_p^0 \omega_0$ sums to zero, a reflection of the martensite embryos settling into a state that eliminates the internal magnetization field when no external field is applied. In the second term, one can introduce tensor notation and simplify in the following manner:

$$\mathbf{M} = \gamma \sum_p (\mathbf{M}_p^0)_i (\mathbf{a}_p)_j \mathbf{H}_j \tag{5.4}$$

$$\mathbf{M} = \gamma \left(\sum_p (\mathbf{M}_p^0)_i (\mathbf{a}_p)_j \right) \mathbf{H}_j = \chi_{ij} \mathbf{H}_j \tag{5.5}$$

This simplification demonstrates (1) a natural linear response to the magnetic

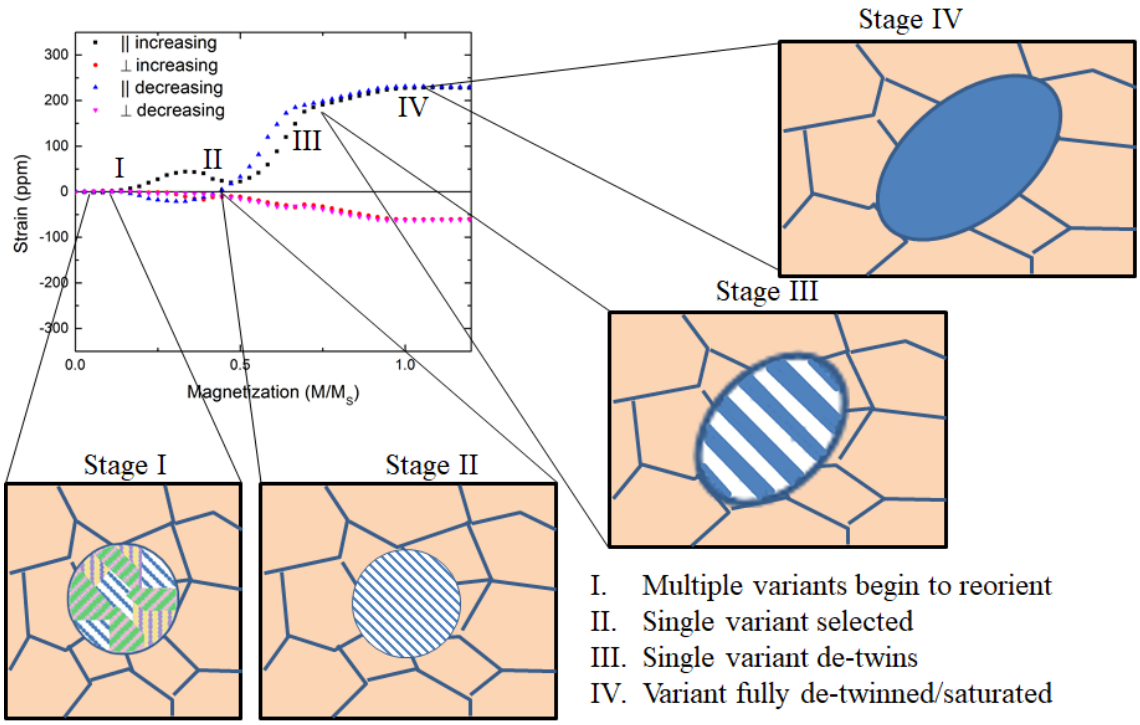

Figure 5.4: A schematic to illustrate how non-Joulian magnetostriction is achieved in $Fe_{82}Ga_{18}$ through an adaptive martensitic response. The sample is fully demagnetized at zero field (Stage I) through the inhomogeneous distribution of randomly oriented nanoscale martensite embryos. As the field increases (Stage II), variants aligned with the field grow while those unfavorably aligned shrink. At a critical field (Stage III), only favorably aligned variants are left and begin to de-twin to rotate their magnetic moments further towards the field. At saturation (Stage IV), the sample is fully de-twinned and magnetically saturated.

field on the basis of growing and shrinking martensite embryos as well as (2) a magnetic susceptibility χ_{ij} uniquely defined by the magnetoelastic response of these embryos based on their position with respect to the field. This result, however, stands in contrast to the evidence that the demagnetization factor determines the slope of the magnetization in response to the field. Whether χ_{ij} reflects an intrinsic value or extrinsic geometry is unknown, and more theoretical work must be done to establish such a connection to the PFM model.

A schematic for how the adaptive martensitic causes non-Joulian magnetostric-

tion is depicted in Figure 5.4. At zero field, labelled Stage I, the sample possesses inhomogeneously distributed and randomly oriented martensite embryos configured to isotropically demagnetize the material. As the field increases, the magnetostriction becomes non-linear within Stage II, during which the martensite embryos reorient as variants aligned with the field grow while others unfavorably aligned shrink. At Stage III, the magnetostriction transitions to a linear response as favorably aligned martensite variants begin to de-twin, rotating their overall magnetic moment towards the applied field. At Stage IV, the sample becomes fully de-twinned as magnetic/magnetoelastic saturation is achieved.

5.2 Future Work

The evidence of training through repeated thermal/magnetic cycles in $Fe_{82}Ga_{18}$ makes imperative further study into the processing of these materials. Initial processing effects on the magnetostriction have been acknowledged since the first report on large magnetostriction in FeGa in 2003 by Clark et al. [19], but thorough evaluation of these effects has been limited. Typically, the only consideration in studies is between quenching or slow-cooling alloys from a homogenizing heat treatment at 1273 K [2, 22, 24, 25], and only very recently has Rahman et al. demonstrated that annealing at a different temperature of 773 K also affects the magnetostriction substantially [2]. The initial microstructure developed by different processes likely affects the tendency of these alloys to exhibit growth of nanoscopic precipitates, but the drastic effect that training has on FeGa alloys suggests that groups looking at

supposed single crystals of equivalent composition may in actuality be studying fundamentally different materials. That is to say, the discrepancy in magnetostriction values, elastic constants, magnetization, and magnetic anisotropy from different research groups is the result of studying FeGa alloys with different metastable phases achieved from variations in processing before study at room temperature.

An end to the debate around the origin of high magnetostriction in FeGa alloys, and whether the behavior is Joulian or non-Joulian, must first come from acknowledging the inherent metastability that comes from bypassing the evolution of equilbrium phases in the Fe-Ga binary system due to processing. Pure A2, A2+$D0_3$, Pure $D0_3$, and martensitic 6M transformations from the $D0_3$ are all non-equilibrium structures in consideration with 15-30 at. % Ga region in the phase diagram, yet no systematic study exists which attempts to assess which processing conditions yield a particular metastable state. Our group is currently conducting preliminary studies in regards to this by measuring magnetostriction for $Fe_{81}Ga_{19}$ polycrystals subject to 30 minute heat treatments followed by ice-quenching at 50 K temperature intervals from 200 - 500 K. The goal of such studies is to demonstrate the variation in magnetoelastic characteristics through low temperature anneals of an already metastable alloy, and ultimately we plan to relate the results to structural measurements carried out with either high-resolution synchrotron XRD or TEM SAD. Such studies will form the foundation of research into the phase and magnetoelastic evolution of highly magnetostrictive FeGa alloys attributable to processing.

In addition to experimental studies assessing processing effects, theoretical research based on first principles, such as Density Functional Theory (DFT), repre-

sents a second avenue to evaluate the metastable characteristics of the A2, $D0_3$, and 6M phases of FeGa. Such DFT calculations carried out by Gruner et al. on FePd alloys demonstrated that premartensitic tweed develops as a metastable structure that twins on the nanoscale to reduce magnetostatic energy [60]. The difference in formation energy between parent disordered FCC and nano-twinned martensitic FCT is between 1-2 meV/atom in $Fe_{68}Pd_{32}$. Evaluating the formation energies of the A2, $D0_3$, and 6M martensites with considerations of their magnetostatic energies would allow one to better assess the metastable formation of these phases in FeGa alloys of composition 15-30 at. %.

The second major direction for future work relating to FeGa alloys will be quantitative modelling of the non-Joulian response. Such research should come after more reliable processing techniques are established to reliably fabricate FeGa alloys exhibiting such characteristics. Ultimately, an accurate model would have to take into account the influence of the non-martensitic cubic phase as well as the size effects of the nanocrystalline microstructure. Such models do not exist in the current literature. In a simple assumption of superposition, one could imagine a magnetostrictive model as

$$\lambda(H) = \chi_{A2}(H)\lambda_{A2}(H) + \chi_{D0_3}(H)\lambda_{D0_3}(H) + \chi_{6M}(H)\lambda_{6M}(H) + \chi_{GB}(H)\lambda_{GB}(H) \tag{5.6}$$

where $\lambda(H)$ represents the total magnetostriction, $\chi_i(H)$ represents the phase fraction of phase i with respect to field, and $\lambda_i(H)$ represents that phase's distinct magnetostriction behavior. Owing to the fact that phase fractions evidently change

with respect to the field, one must also append this expression with interaction terms between the phases:

$$\begin{aligned}\lambda(H) = {} & \chi_{A2}(H)\lambda_{A2}(H) + \chi_{D0_3}(H)\lambda_{D0_3}(H) + \chi_{6M}(H)\lambda_{6M}(H) + \chi_{GB}(H)\lambda_{GB}(H) \\ & + \frac{\partial \chi_{A2\leftrightarrow D0_3}}{\partial H}\varepsilon_{A2\leftrightarrow D0_3} + \frac{\partial \chi_{A2\leftrightarrow GB}}{\partial H}\varepsilon_{A2\leftrightarrow GB} + \frac{\partial \chi_{D0_3\leftrightarrow 6M}}{\partial H}\varepsilon_{D0_3\leftrightarrow 6M} + \frac{\partial \chi_{D0_3\leftrightarrow GB}}{\partial H}\varepsilon_{D0_3\leftrightarrow GB} \\ & + \frac{\partial \chi_{6M\leftrightarrow GB}}{\partial H}\varepsilon_{6M\leftrightarrow GB}\end{aligned} \tag{5.7}$$

where $\frac{\partial \chi_{i\leftrightarrow j}}{\partial H}$ represents the change in phase fraction i with respect to phase j due to the change in field and $\varepsilon_{i\leftrightarrow j}$ is the amount of strain introduced by the change in phase. For such a model to prove effective, one would have to determine the equilibrium evolution of the different phase fractions based on thermodynamic principles and intrinsic magnetic, elastic, and magnetoelastic properties inherent to each phase, such as $M_{s,i}$, E_i, and B_i. However, acquiring data pertaining to all of the different phase fractions and magnetoelastic responses is what makes it imperative to develop first a better understanding of how the phase fractions develop under metastable processing conditions in these alloys.

5.3 Conclusion

The work contained in this thesis sought to connect the structural properties of $Fe_{100-x}Ga_x$ ($x = 17, 18, 19, 22$, and 26) alloys to their anomalous magnetic and magnetoelastic behavior. Extensive debate has ensued over the years regarding the extent to which the presence of disordered BCC A2, ordered BCC $D0_3$, or possible

nanoprecipitate martensite influences these properties, and this thesis suggests the debate has stemmed from attributing the same magnetoelastic properties to fundamentally different FeGa alloys with variations in metastable phase evolution due to processing. For our alloys, large magnetostriction coupled with low anisotropy defies the classical Joule framework of magnetostriction, and diffraction carried out through TEM measurements was elected to assess whether nanoprecipitate phases may be account for this behavior. To assess whether structural changes occur in response to a change in magnetic field, *in situ* high resolution and nanoelectron diffraction studies were carried out in the TEM while modulating the objective lens voltage. The main results from the thesis are as follows:

1. The three alloys, $Fe_{82}Ga_{18}$, $Fe_{81}Ga_{19}$, $Fe_{78}Ga_{22}$, possess a nanocrystalline microstructure of ∼5 nm crystallites, revealed through high-resolution imaging of extremely thin areas of FIB-prepared samples.

2. Each alloy possessed at least the presence of A2 and $D0_3$, with clear evidence of 6M martensite in both the $Fe_{82}Ga_{18}$ and $Fe_{81}Ga_{19}$ alloys.

3. Each alloy appears to exhibit a change in the amount of $D0_3$ as a function of field inside the TEM, based on analysis of the intensity of $D0_3$ reflections observed in the NED patterns.

4. The $Fe_{82}Ga_{18}$ alloy showed clear signs of training after roughly 13 temperature cycles from 233 to 373K and 512 magnetic field cycles from 0 field to saturation. A significant uniaxial anisotropy developed in the magnetic torque data after seven years between measurements. The saturation magnetostriction, $\lambda_{\parallel-\perp}$

increased from 300 to 570 ppm, as a result of training the sample during eight months of repeated measurements. Significant increase in D03 signal intensity in the NED patterns was observed as well.

5. The results suggest future research should systematically evaluate phase and magnetoelastic evolution within Fe-Ga alloys based on their processing history. DFT calculations of formation energies for possible metastable phases in the Fe-Ga system could support such studies and lead to a much improved understanding of fabricating high magnetostriction FeGa alloys which display either Joulian or non-Joulian magnetostriction.

6. Aspects of modelling nanocrystalline SMAs were discussed. Recent modelling done by Li and Sun demonstrate that hysteresis in stress-strain behavior vanishes below a critical grain size in $Ni_{49.1}Ti_{50.9}$ [53], and a simple model of an adaptive martensite under an applied magnetic field demonstrates that growth/shrinking of martensite embryos can yield an isotropic, linear magnetization response [59].

7. A conceptualized model for the non-Joulian magnetostriction was put forth. Future work must be done to quantify such behavior with a model which can capture the differing magnetoelastic responses of the A2, $D0_3$, and 6M phases reorienting at the nanoscale.

The fundamental origin of non-Joulian magnetostriction in FeGa, as well as other related alloys like FePd and FeAl, is related to the tendency of these materials to form metastable, adaptive martensites at the nanoscale. The results contained

in this thesis make clearer that models must move away from assumptions of single crystal, single phase microstructures, and, while the problem thus becomes more complex to solve, the experimental results provide new evidence to guide future research into these materials' unique behavior.

Appendix A: Martensitic materials and the shape memory effect

The characteristics of phase transformations which give rise to the shape memory effect have been well-documented and can be traced back to early studies of a body-centered tetragonal (BCT) crystal phase called martensite, after Martens [61], that manifests in steel alloys when quenching from the high temperature face-centered cubic (FCC) phase to room temperature. To accommodate the sudden thermal compression of the large temperature gradient induced by quenching, the metal system relaxes by distorting some of the FCC structure into a BCT structure irreversibly, shown in Figure A.1. Such a transformation occurs rapidly, approaching the speed of sound in the metal, spreading through the material as a soliton [62]. Because of the time scale, there exists no opportunity for the equilibrium diffusion-controlled eutectic separation of iron into body-centered cubic (BCC) α-ferrite phase and ordered Fe_3C cementite. Thus, the martensitic transformation is termed displacive, only involving a rearrangement of atoms within the crystal rather than movement of atoms towards structures of differing compositions, and it exists as an alternative to mitigate the evolution of large strain in the material.

Possessing a martensitic transformation satisfies only one requirement for a material to exhibit the shape memory effect. The second requirement is that the dis-

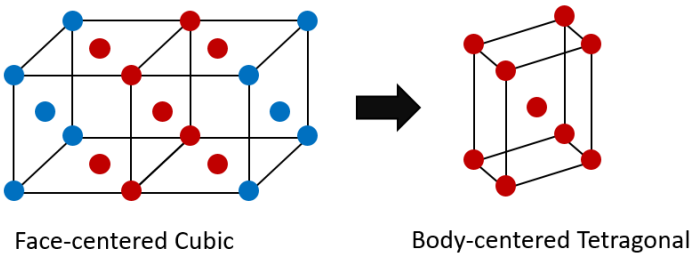

Figure A.1: A schematic depicting how the martensitic body-centered tetragonal structure forms from displacing atoms contained in the austenitic face-centered cubic structure.

placive transformation be reversible, which was not recognized until discovery of the first shape memory alloy NiTi, or nitinol, by the US Naval Ordnance Laboratory in 1959 [63]. Reversibility implies that the martensitic alloy may be transformed back and forth between its higher temperature, higher symmetry parent, or austenitic, phase and its lower temperature, lower symmetry martensitic phase through the application of stress or temperature. The manifestation of reversibility exists within a subset of martensitic alloys, and it emerges for those materials whose parent and martensitic phases possessing a softening of their shear elastic constant c' ($\frac{C_{11}-C_{12}}{2}$) about a transformation temperature [64]. Below the transformation temperature, the martensite transforms to the lower symmetry martensite, and the strain between the austenite and martensite is accommodated throughout the crystal by twinning within the microstructure. This twinning allows the material to retain its original shape, but when in this twinned state, the application of a stress well-below the threshold for plastic deformation allows the material to deform through shear motion of the twins about their boundaries. If heat is then supplied to the material,

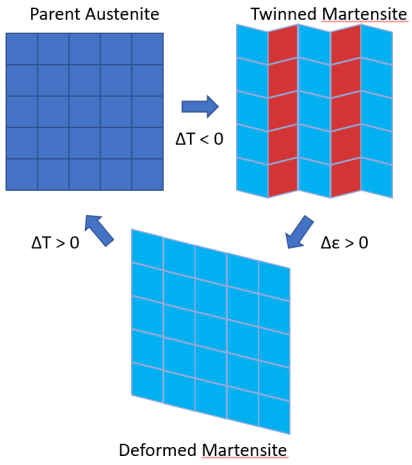

Figure A.2: A diagram depicting the shape memory effect made possible through a reversible martensitic transformation.

it will transform back to the parent phase and its original shape, earning the name shape memory. A diagram of this is shown in Figure A.2.

Mathematically, martensite transformations are typically modelled using the Landau-Ginsburg theory, which explains the transformation through a power series approximation of the free energy as a function of the strain physically reflected in the shape change between austenite and martensite phases. These strains are mapped to tensors which express both the longitudinal and shear strains in reference to the parent phase. For a cubic to tetragonal transformation, the symmetry change is described by two major strain components: elongation/compression along the c-axis of the new tetragonal crystal, ϵ_c, and the transverse strains for the new a-axis lattice constants, ϵ_a. The crystal transformation is then clearly expressed through the following relations:

$$\epsilon_c = \frac{c_t - a_c}{a_c}, \epsilon_a = \frac{a_t - a_c}{a_c} \tag{A.1}$$

$$E_1^t = \begin{bmatrix} \epsilon_c & 0 & 0 \\ 0 & \epsilon_a & 0 \\ 0 & 0 & \epsilon_a \end{bmatrix}, E_2^t = \begin{bmatrix} \epsilon_a & 0 & 0 \\ 0 & \epsilon_c & 0 \\ 0 & 0 & \epsilon_a \end{bmatrix}, E_3^t = \begin{bmatrix} \epsilon_a & 0 & 0 \\ 0 & \epsilon_a & 0 \\ 0 & 0 & \epsilon_c \end{bmatrix} \tag{A.2}$$

where the subscripts t and c correspond to the tetragonal and cubic phase, respectively, and c and a refer to their respective crystallographic axes. Based on symmetry between parent and martensite, one observes three distinct possible transformations in equation A.2, depending on the axis the parent crystal distorts towards the new tetragonal c-axis. Applying these strains to the Landau-Ginsburg model requires reducing the tensor components to six strain-order parameters: e_1, the dilatation strain; e_2 and e_3, the deviatoric strains; and e_4,e_5, and e_6, the shear strains. These are mapped according to the following relations:

$$\begin{aligned} e_1 &= \frac{1}{\sqrt{3}}(\epsilon_{11} + \epsilon_{22} + \epsilon_{33}) \\ e_2 &= \frac{1}{\sqrt{2}}(\epsilon_{11} - \epsilon_{22}) \\ e_3 &= \frac{1}{\sqrt{6}}(\epsilon_{11} + \epsilon_{22} - 2\epsilon_{33}) \\ e_4 &= \epsilon_{23} \\ e_5 &= \epsilon_{13} \\ e_6 &= \epsilon_{12} \end{aligned} \tag{A.3}$$

The Landau-Ginsburg model is then expressed fully as

$$F_L^t = A(e_2^2 + e_3^2) + Be_3(e_3^2 - 3e_2^2) + C(e_1 - E_0(e_2^2 + e_3^2))^2 + D(e_2^2 + e_3^2)^2 \tag{A.4}$$

where F_L^t is the free energy, and A, B, C, D, and E_0 are temperature-dependent coefficients empirically fitted to mimic the elastic constants as a function of temperature of the material being modelled. The temperature dependence for the coefficients is consistent, following a $\frac{T-T_0}{T_0}$ relation in consideration of the transformation temperature T_0, though some coefficients exhibit stronger dependence on this than others. A thorough, applied use of this type of model can be found in reference [65]. Within the model, the quadratic terms associated with coefficient A represent a harmonic potential that keeps the crystal stable in a cubic state (i.e. $\epsilon = 0$) above T_0. As the temperature approaches T_0, this initial well becomes shallower. The anharmonic term associated with the B coefficient causes a secondary potential well to begin forming below T_0 with a local minimum reflecting the martensite invariant strain e_0 ϵ_c. Once this well falls below the harmonic minimum, the material itself strains towards the new equilibrium state, thus completing the martensitic transformation. The quartic terms associated with C, E_0, and D close the potential well and tend to have weaker temperature dependence. To capture the distinct variants that can form, angular dependences can be introduced to the free energy term. For a cubic to tetragonal transformation, this dependence is introduced to the anharmonic term, transforming B into $B(\theta)$ such that $B = B(T)sin(3\theta)$. The results of Landau-Ginsburg analysis are shown in Figure A.3, showing free energy contour plots at different temperatures along with the phenomenology of the crystal structure transformation.

The characterization of a material's martensitic transformation thus requires extensive understanding of the mechanical properties for the various structures pos-

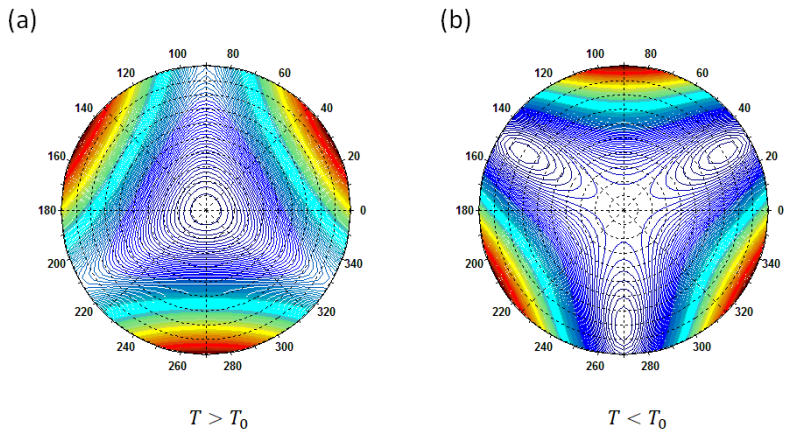

Figure A.3: Energy contour plots using Landau-Ginsburg theory to show the development of three tetragonal variants as temperature decreases from **(a)** above the transformation temperature to **(b)** below it.

sible in these materials. The first thing to characterize are the crystal structures of the parent and the martensite phase, as well as identifying the temperature at which the transition occurs. The twinning that occurs in shape memory alloys (SMAs) give these materials complex microstructures as well. To understand how these microstructures develop, one must take the knowledge of parent and martensite crystal structure to analyze the symmetry relations between the two. These symmetry relations dictate the different variants, or unique crystalline configurations, of martensite which develop out of the parent phase. These different twins intersect at boundaries of shared planes, wherein the twins exist as stress-free domains and the twinning planes contain the strain induced by the transformation. From this, one can conduct mathematical evaluations of the twins, characterized by matrices of their crystal structure, and examine their compatibility with other twins and evaluate the strains therein to predict more energetically stable combinations of twins which then give rise to the material's microstructure. This technique was developed

heavily by the work of James' and his group [64, 66, 67], allowing one to condense the complexity of the microstructure into a quantifiable mathematical understanding. As an example, not only can one determine that three tetragonal variants arise in a cubic to tetragonal transition, but also that these variants themselves give rise to either type I or type II twins, depending on the commensurability of the shared twinning plane. Type I twins for cubic to tetragonal transitions typically have commensurate {110} twinning planes. Furthermore, because these operations essentially quantify how well the twins fit, one can build a correlation between SMAs which possess better fits and the extent of reversibility in the alloy. This is more so being seen in development of high-fatigue SMAs [68] which necessarily require very low hysteresis in the transformation to permit an extremely high number of stress cycling. In a similar vein, it is important to measure the various elastic constants of the parent and martensitic phase as a function of temperature, which can give one another way to gauge how reversible the transition is.

From an elastic point of view, one can see that SMAs require much to fully characterize their behavior. Fundamentally, however, all of this behavior reflects changes in thermodynamic equilibrium for a material undergoing drastic changes in internal stress that cannot be released through diffusion-controlled mechanisms. This gives rise to complex microstructures which minimize the strain by transforming and twinning, turning the energetics into a competition between strain mitigation and energy increased by the surface energy of twinning interfaces. The introduction of magnetism to these alloys may then be seen as an extension to this approach of energy minimization, meaning FSMAs not only will twin to minimize their internal

stress but also their internal magnetic field.

Appendix B: Classical magnetization, magnetostriction, and magnetic anisotropy

B.1 Origins and classification of magnetism in materials

All materials possess magnetism due to the charge nature of electrons which continuously move around their orbits in materials. The type of magnetism depends on whether constituent elements of a material have unpaired electrons whose angular momentum induces an internal magnetic field not cancelled out by a paired counter-spin. These types of magnetic materials can be expected to have elements from the d- or f-block groups of the periodic table, the most common of which are Fe, Co, and Ni. Materials possessing unpaired electrons enhance the magnetic flux through their bulk when an external field is applied as opposed to those possessing solely paired electrons, which reject it in accordance with Faraday's Law. Regardless of the type of magnetism, all magnetic materials thus follow a proportional relation between their induced flux, $\mathbf{B}$ and the applied field $\mathbf{H}$:

$$\mathbf{B} = \mu\mathbf{H} \tag{B.1}$$

where μ is the permeability of that material. This flux is a combined result of both the contribution of the field to the flux as well as the material's enhancement of the flux, so the relation is often expanded to segregate the material's response to that of a vacuum:

$$\mu = \mu_0 \mu_r \tag{B.2}$$

$$\mathbf{B} = \mu_0 \mu_r \mathbf{H} \tag{B.3}$$

$$\mu_r = 1 + \chi \tag{B.4}$$

$$\mathbf{B} = \mu_0 (1 + \chi) \mathbf{H} \tag{B.5}$$

$$\mathbf{B} = \mu_0 \mathbf{H} + \mu_0 \chi \mathbf{H} = \mu_0 (\mathbf{H} + \mathbf{M}) \tag{B.6}$$

$$\chi = \frac{\partial \mathbf{M}}{\partial \mathbf{H}} \tag{B.7}$$

These relations form the basis of magnetism in all materials, and new material-dependent terms have been introduced: μ_r is the relative permeability of a material, χ is the magnetic susceptibility of a material, and $\mathbf{M}$ is the magnetization vector of a material. These parameters distinguish the expected flux from applying a field in a vacuum, $\mu_0 \mathbf{H}$.

Materials have three major classes of magnetism defined by magnitude and sign of χ. Diamagnetic materials possess paired electrons throughout their bulk, and these materials have no internal magnetic fields of their own. They lightly expel magnetic flux in accordance with Faraday's Law, possessing susceptibilities on the order of -10^{-5} [69]. Paramagnetic materials possess unpaired electrons throughout

their buk, and these materials have internal magnetic fields that lightly enhance the magnetic flux, with χ ranging from $10^{-5} - 10^{-2}$ [69]. In terms of practical applications, one would not say a diamagnet or paramagnet has much practical use due to the extremely small magnitude of χ in each case. Thus, these two classes belong to materials typically thought of as non-magnetic.

The third class of magnetism is called ferromagnetism, and the magnetic behavior of materials in this class is subdivided into three further categories: ferromagnetism, ferrimagnetism, and antiferromagnetism. Each material in this class possesses collective spin alignment or anti-alignment throughout their bulk that is explained by the introduction of a new contribution to the free energy of the system with roots in the quantum mechanical behavior of electron spin between neighboring atoms within a crystal [70]. This contribution is called the exchange interaction, $E_{exchange}$, and it is defined by the following relation:

$$E_{exchange} = -\frac{1}{2}\sum_{i \neq k}^{n} J_{ik}\mathbf{s}_i \cdot \mathbf{s}_k \tag{B.8}$$

where i and k subscripts represent distinct atoms in the material, J_{ik} is a proportionality constant called the exchange constant for the atom pair, and $\mathbf{s}_i$ and $\mathbf{s}_k$ are the spin angular momentum numbers of those atoms. The exchange constant is closely tied to the change in electrostatic potential from overlap of wavefunctions between bonded atoms in a material [70]. It thus takes significant values only between nearest neighboring and, occasionally, next nearest neighboring atoms, so often one

might see the relation reduced to

$$E_{exchange} = -J_{exchange} \sum_{i=1}^{N} \mathbf{s}_i \cdot \mathbf{s}_{i+1}$$
$$E_{exchange} = -N J_{exchange} (\mathbf{s}_1 \cdot \mathbf{s}_2) \tag{B.9}$$

where the summation now is performed over only nearest neighbors, $J_{exchange}$ is the exchange constant for nearest neighbors, N is the total number of atoms in the material, and $\mathbf{s}_1$ and $\mathbf{s}_2$ are a single dot product evaluated only for nearest neighbors.

The result from eq. B.9 demonstrates that magnetic materials collectively align all spins or anti-align all spins depending on the sign of $J_{exchange}$. If $J_{exchange} > 0$, the material will align its magnetic spins such that $\mathbf{s}_1 \cdot \mathbf{s}_2 = \frac{1}{4}$, thereby lowering the free energy of the system. Such materials are called ferromagnetic, and their collective spin arrangements enhance the internal magnetic flux considerably, possessing χ values between $10^2 - 10^6$. If $J_{exchange} < 0$, the material anti-aligns its magnetic spins such that $\mathbf{s}_1 \cdot \mathbf{s}_2 = -\frac{1}{4}$ in order to lower the free energy. These materials are called antiferromagnetic, and they have zero magnetization with no external field. Unlike diamagnets, antiferromagnets do possess positive χ values typically on the order of 10^2. Supplied magnetic energy causes the spins to slowly align, and high fields, greater than 3-4 T, can yield greatly enhanced χ mimicking ferromagnetic-like behavior [71, 72].

Ferrimagnets possess more nuanced exchange interactions that must take into account both nearest neighbor and next nearest neighbor interactions. These materials are typically oxides possessing ions of differing charges, the most common

example of which is magnetite Fe_3O_4. In Fe_3O_4, two Fe^{3+} atoms on octahedral sites order antiferromagnetically in their exchange, but the Fe^{2+} atoms on tetrahedral sites order ferromagnetically across unit cells, resulting in net ferromagnetic-like behavior whose magnitude is reduced comparatively if all spins were aligned. These materials possess χ values between $10^2 - 10^3$ in magnitude.

B.2 Overview of Magnetic Anisotropy

The majority of ferromagnetic materials have appreciable magnetic anisotropy, preferred directions the individual moments point towards with respect to the crystal structure. For pure Fe, the "easy," or preferred directions are $\langle 100 \rangle$, while in pure Ni, the easy directions are $\langle 111 \rangle$ [16]. Hexagonal ferromagnets like pure Co possess uniaxial magnetic anisotropy, having moments pointed solely along the c-axis with a strong aversion to pointing in the basal plane. For uniaxial magnets, the anisotropy typically is expressed as a power series with respect to the direction of the magnetic moment, θ, keeping only the first three terms:

$$U_{a,uniaxial} = \sum_n K_n \sin^{2n}\theta = K_0 + K_1 \sin^2\theta + K_2 \sin^4\theta + \ldots \tag{B.10}$$

where $U_{a,uniaxial}$ is the anisotropy energy density and K_n are anisotropy constants typically obtained empirically. Cubic ferromagnets tend not to have uniaxial anisotropy, but the expression for $U_{a,cubic}$ is obtained similarly through a power series expansion, taking into account the direction cosines of the magnetic moment direction

with respect to each axis:

$$U_{a,cubic} = K_0 + K_1(\alpha_1^2\alpha_2^2 + \alpha_2^2\alpha_3^2 + \alpha_1^2\alpha_3^2) + K_2(\alpha_1^2\alpha_2^2\alpha_3^2) \tag{B.11}$$

where α_1, α_2, and α_3 corresponds to the [100], [010], and [001] axes, respectively. The nature of the magnetic anisotropy is determined by the sign and magnitude of the anisotropy constants. For instance, Fe has $K_1 = 4.8 \times 10^4\ J/m^3$ while Ni has $K_1 = -4.5 \times 10^3\ J/m^3$, which accounts for the change in easy axes from $\langle 100 \rangle$ to $\langle 111 \rangle$ between the two materials [16]. For uniaxial materials like Co, $K_1 > 0$, but a uniaxial material could also have $K_1 < 0$, causing the c-axis to become the "hard" to magnetize direction while xy-basal plane becomes easy for any direction it contains. Cubic materials can also possess $\langle 110 \rangle$ easy directions if the anisotropy constants satisfy the condition that $K_1 < 0$ and $\frac{9|K_1|}{4} < K_2 < 9|K_1|$ [73]. Lower symmetry crystal structures tend to display uniaxial-like behavior depending on how the c/a distortion and its effects on the anisotropy along the c-axis [74], but the formulation differs from Eq. B.10 since one must take develop the formula in accordance with the crystal symmetry [16, 75]:

$$U_{a,tetragonal} = K_0 + K_1 \cos^2\varphi - \frac{1}{2}K_{2,c}\cos^4\varphi - \frac{1}{8}K_{2,a}(3 + \cos 4\theta)\sin^4\varphi \tag{B.12}$$

where the fourth-order constant splits into two terms for the c-axis, $K_{2,c}$, and the two equivalent a-axes, $K_{2,a}$, and a new angular dependence, φ, describes the azimuth between the a and c-axes.

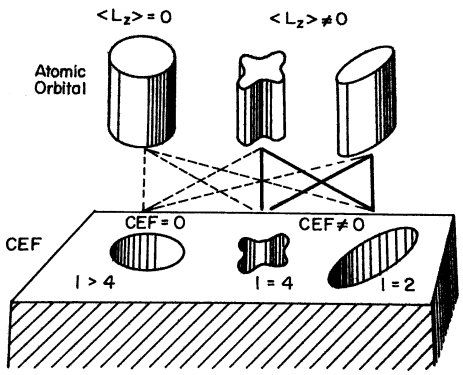

Figure B.1: Taken from [16], an illustration of how the crystal electric field accommodates differently shaped orbitals with $\langle L_z \rangle \neq 0$.

Magnetic anisotropy comes from a separation of energy between electron orbital states as they couple to the crystalline electric field of the lattice. If valence electrons of an atom are unpaired and have nonzero angular momentum ($L_z \neq 0$), then the electron orbital will have a non-spherical charge distribution which must assume a preferred orientation with respect to the crystal field. The concept is illustrated in Figure B.1, taken from [16], where electron orbitals of non-zero L_z assume the proper placement into the crystal, like puzzle pieces. The spin can also have a preferred orientation coupled to the orbital provided $\xi \mathbf{L} \cdot \mathbf{S} \neq 0$, where ξ is a proportionality constant to evaluate the magnitude of the spin-orbit coupling energy. Given a crystal field energy D, a material may exhibit a weak anisotropic response to an external field H_{ext} with strong dependence on the crystal symmetry if $D > \xi \mathbf{L} \cdot \mathbf{S}$, or it may exhibit a strong anisotropic response as the spin rotates against both the crystalline and orbital charge distribution if $D < \xi \mathbf{L} \cdot \mathbf{S}$. Precisely evaluating the anisotropy based on D, L_z, $\mathbf{L}$, and $\mathbf{S}$ is neither straightforward nor trivial, since evaluating D itself in bulk materials becomes complicated by the emergence

of energy bands. The values of L_z also change as a result of crystal field splitting for $3d$ transition metal ions whereby the five $3d$ wavefunctions for a bonding ion split into two groups: t_{2g}, which contains d_{xy}, d_{yz}, and d_{xz}; and e_g, which contains d_{z^2} and $d_{x^2-y^2}$. The difference in energy between t_{2g} and e_g orbital configurations is proportional to the crystal field energy, and the valence electron configuration of the transition metal ion in question dictates whether filling in t_{2g} or e_g states is more favorable. Fe^{2+} ions have $3d^6$ configuration and prefer e_g occupation whereas Cr^{4+} ions have $3d^4$ configuration and prefer t_{2g} occupation [16]. Qualitatively, an applied field H_{ext} must overcome energy barriers between such states to re-orient the magnetization, and that these barriers represent the basis of magnetocrystalline anisotropy.

B.3 Domain Structures

The dipole nature of the magnetic field means its field lines can never terminate at a point source, a fact enshrined by Gauss' theorem $\nabla \cdot \mathbf{B} = 0$. The integral form of this equation, $\int\int \mathbf{B} \cdot d\mathbf{A} = 0$, implies that a magnetic material cannot generate excess magnetic flux outside of its surface; otherwise the magnet would act as the equivalent of a point charge, of which no example has been found in nature [16]. This condition leads to two important relations which describe how magnetic materials

influence the magnetic field surrounding them:

$$(\mathbf{B}_2 - \mathbf{B}_1) \cdot \mathbf{n} = 0 \tag{B.13}$$

$$(\mathbf{H}_2 - \mathbf{H}_1) \cdot \mathbf{n} = (\mathbf{M}_1 - \mathbf{M}_2) \cdot \mathbf{n} \tag{B.14}$$

where the subscripts 1 and 2 refer to the material's and environment's surfaces, respectively, and $\mathbf{n}$ is the surface normal. Equation B.13 states that the magnetic flux across an interface must maintain a continuous normal component, and Eq. B.14 specifically describes how the field $\mathbf{H}_2$ outside of a magnetic material is influenced by the magnetization $\mathbf{M}_1$ at the surface. In the center of magnetically charged surfaces, the magnetization aligns with the surface normal. Assuming the second surface is a vacuum, such that $\mathbf{M}_2 = 0$, the field outside the material is enhanced by $\frac{|\mathbf{M}_1|}{2}$ while inside the material an equal and opposite field develops. This opposing field is called the demagnetization field, H_d, and it is generally expressed as

$$H_d = \mathbf{M} \cdot \mathbf{n} = -NM \tag{B.15}$$

where N is called the demagnetization factor, a tensor relating the sample geometry to the internal field. The tensor is defined such that its trace equals 1; or, to put it another way, if the tensor can be defined by three principal orthogonal directions, then $N_x + N_y + N_z = 1$. A value of $N = 1$ for a position on the surface of a magnetic material implies the magnetization at that point is parallel to the surface normal. It costs energy to align magnetic dipoles along a surface in this manner,

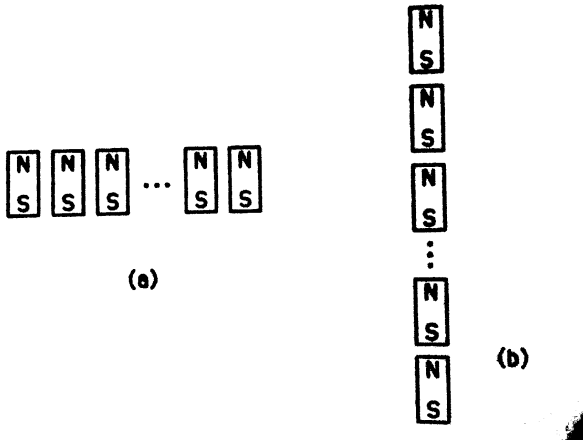

Figure B.2: Taken from [16], **(a)** side-by-side magnetic dipole configuration as compared to a **(b)** line of magnetic dipoles. The configuration in **(a)** has many unfavorable north-north interactions that are eliminated within a configuration like **(b)**.

energy which becomes stored in the demagnetization field surrounding the material, depicted in Figure B.2. These fields have potential $U = -\mu_m \cdot \mathbf{B}_0$. A material's magnetization influences this energy such that $(\frac{N}{V})U = u = -\frac{1}{2}\mathbf{M} \cdot \mathbf{B}_0$. The factor of $\frac{1}{2}$ is needed because this energy is a result of dipole pair interactions, meaning summation must only count each unique pair once. Recognizing that outside of an external field, $\mathbf{B}_0 = \mu_0 \mathbf{H}_d$, a material's magnetostatic energy is expressed by

$$u_{ms} = -\frac{\mu_0}{2}\mathbf{M} \cdot \mathbf{H}_d = \frac{\mu_0}{2} N M^2 \tag{B.16}$$

Saturated magnetic materials thus store considerable energy which they are able to reduce by dividing segments of themselves into regions of opposing magnetization, called magnetic domains. Within a domain, all magnetic moments are aligned along an easy axis, and domains are separated by special interfaces called domain walls. This phenomenon is shown in Figure B.3, taken from [76], and the

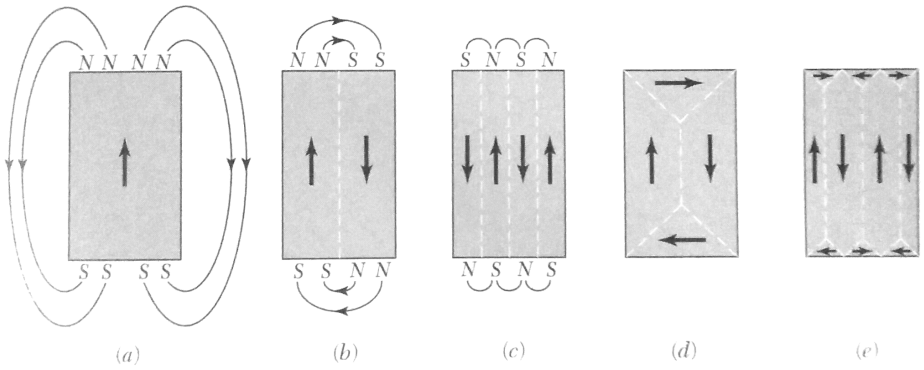

Figure B.3: Taken from [76], a series of magnetic domain configurations which better eliminate their magnetostatic energy through **(a)-(e)**.

splitting of the magnetization into separate domains reduces the magnetostatic energy approximately by a factor of $1/n$, where n is the number of domains formed in the system [77].This energy mitigation then comes into competition with the added energy to the system for creating a domain wall. The exchange energy (Eq. B.9) prevents spins from aligning antiparallel across neighboring atoms; otherwise the energy increase would be on the order of JS^2. Materials instead introduce very small rotations, $\theta \ll 1$ such that $\Delta E_{ex} = JS^2 \cos\theta \approx JS^2\theta^2$. These rotations, however, now add anisotropy energy into the system as they move off axis, proportional to the number of rotations introduced to mitigate the cost in exchange energy.

A thorough analytical model of this behavior was first developed by Landau and Lifshitz in 1935 [78] to minimize the free energy of a domain wall by considering an anisotropy density, $f_a(\theta)$, and macroscopic exchange energy density, $A\left(\frac{\partial\theta}{\partial z}\right)^2$, where A is called the exchange stiffness ($A = \frac{JS^2}{a}$), in the following expression:

$$f = f_a(\theta) + A\left(\frac{\partial\theta}{\partial z}\right)^2 \tag{B.17}$$

The surface energy density, σ_{dw} of a wall can be obtained by integrating this expression over the wall thickness:

$$\sigma_{dw} = \int \left[f_a(\theta) + A\left(\frac{\partial\theta}{\partial z}\right)^2 \right] dz \tag{B.18}$$

Minimizing this term means one must find the values of $\theta(z)$ which give $\partial\sigma_{dw} = 0$. With some arithmetic manipulation, the solution for this condition is solved using the general differential equation

$$\frac{\partial f_a(\theta)}{\partial\theta} - 2A\frac{\partial^2\theta}{\partial z^2} = 0 \tag{B.19}$$

The analytical solution can be obtained by using either the uniaxial or cubic expressions for anisotropy, Eqs. B.10 or B.11, respectively. For the uniaxial case, the solution for the spin angle across the boundary is

$$\theta(z) = \arctan\left[\sinh\left(z\sqrt{\frac{A}{K}}\right)\right] + \frac{\pi}{2}, \tag{B.20}$$

and equilibrium domain wall thickness, δ_{dw}, and domain wall energy now have definite values of

$$\delta_{dw} = \pi\sqrt{\frac{A}{K}} \tag{B.21}$$

$$\sigma_{dw} = 4\sqrt{AK} \tag{B.22}$$

These expressions hold true for uniaxial magnetic materials and apply specifically

to the formation of a 180° wall, but materials of cubic anisotropy can also form 90° walls which have a rotation of θ from 0 to $\frac{\pi}{2}$ rather than 0 to π. This reduces δ_{dw} and σ_{dw} by $\frac{1}{2}$. With 90° walls, it is possible to form closure domains at the material surface which completely eliminate all magnetostatic energy. This elimination of the magnetostatic energy also faces competition with another energy contribution, the magnetoelastic energy, which will be addressed in the following section.

B.4 Joule Magnetostriction

The observation of elastic strain under an applied field was first published by Joule in 1847 [14], and much of its description was phenomenologically characterized by material parameter λ_s, the saturation coefficient. For isotropic materials, one can determine the magnetostriction for any angle θ relative to a hard magnetization axis with the relation

$$\lambda = \frac{3}{2}\lambda_s\big(\cos^2 - \frac{1}{3}\big), \tag{B.23}$$

which, in turn, is proportional to H^2. The strain is uniaxially isotropic, possessing longitudinal strain $e_{\parallel} = \lambda_s$ and transverse strain $e_{\perp} = -\frac{\lambda_s}{2}$. Randomly oriented polycrystalline ferromagnets possess such magnetostrictive behavior, as was the case for the first iron and steel samples studied for this phenomenon. The coupling between magnetic and elastic energy allows one to formulate new magnetoelastic relations by expanding terms for the magnetization, specified by direction cosines

α_i, and the strain tensor, e_{ij} in a MacLaurin series:

$$\begin{aligned} u_m =& f_0 + K_1\alpha_i^2\alpha_j^2 + K_2\alpha_i^2\alpha_j^2\alpha_k^2 + \cdots + c_{ijkl}e_{ij}e_{kl} + H_{ijklmn}e_{ij}e_{kl}e_{mn} + \ldots \\ &+ B_{ij}e_{ij}\alpha_i\alpha_j + D_{ijkl}e_{ij}e_{kl}\alpha_i\alpha_j\alpha_k\alpha_l + \ldots \end{aligned} \tag{B.24}$$

where the K_i terms represent magnetocrystalline anisotropy constants, c_{ijkl} and and H_{ijklmn} describe the first- and second-order elastic stiffness constants, and B_{ij} and D_{ijkl} describe the first- and second-order magnetoelastic coupling coefficients which characterize the magnitude of elongation a material undergoes in response to an applied field.

It was not until 1954 that a microscopic origin for this coupling was put forth by Néel [15]. The interaction energy between two atoms in a solid can be expanded in Legendre polynomials as a function of the bond direction $\mathbf{r}$ and angle ψ between this direction and the magnetization:

$$u_{aa}(r,\psi) = g(r) + l(r)(\cos^2\psi - \frac{1}{3}) + q(r)(\cos^4\psi - \frac{6}{7}\cos^2\psi) + \frac{3}{35}) + \ldots, \tag{B.25}$$

where u_{aa} refers to the energy for a single bond, $g(r)$ describes spatially isotropic effects such as the exchange interaction, $l(r)$ describes dipole-dipole interactions and is called the dipolar term, and $q(r)$ in turn describes quadrupolar effects. Given a magnetization vector $\mathbf{M} = M_s(\alpha_1, \alpha_2, \alpha_3)$ and a direction vector $\mathbf{r} = r(\beta_1, \beta_2, \beta_3)$, where α andβ represent direction cosines, one obtains

$$\psi = \cos^{-1}\left(\frac{\mathbf{M}\cdot\mathbf{r}}{|M||r|}\right) = \alpha_1\beta_1 + \alpha_2\beta_2 + \alpha_1\beta_3 \tag{B.26}$$

One can now write an expression for a reference state of energy in terms of the magnetization angle, considering only first the dipole-dipole interactions:

$$\begin{aligned} u_{aa}(r_0, \psi_0) &= g(r_0) + l(r_0)\Big[(\alpha_1\beta_1 + \alpha_2\beta_2 + \alpha_3\beta_3)^2 - \frac{1}{3}\Big] + \dots \\ &\approx g(r_0) + l(r_0)\Big[(\alpha_1\beta_1 + \alpha_2\beta_2 + \alpha_3\beta_3)^2 - \frac{1}{3}\Big] \end{aligned} \tag{B.27}$$

For a simple cubic crystal, whose bonds may be represented by three orthogonal vectors $r_x = r_0(1,0,0)$, $r_y = r_0(0,1,0)$, and $r_z = r_0(0,0,1)$, under uniaxial strain such that $r_{xx} = r_x(1+e_{xx})(1, e_{xy}/2, e_{xz}/2)$, Eq. B.27 expands into

$$u_{aa}(r_{xx}, \psi_{xx}) = g(r_0(1+e_{xx})) + \Big[l(r_0) + l'(r_0)e_{xx}\Big]\Big[\big(\alpha_1 + \frac{\alpha_2 e_{xy}}{2} + \frac{\alpha_3 e_{xz}}{2}\big)^2 - \frac{1}{3}\Big] + \dots \tag{B.28}$$

If one subtracts Eq. B.27 from Eq. B.28, one obtains change in magnetic energy due to strain, or the magnetoelastic energy:

$$\begin{aligned} u_{me} &= u_{aa}(r_{xx}, \psi_{xx}) - u_{aa}(r_0, \psi_0) \\ &= g'(r_0)e_{xx} + l'(r_0)e_{xx}(\alpha_1^2 - \frac{1}{3}) + l(r_0)[\alpha_1\alpha_2 e_{xy} + \alpha_1\alpha_3 e_{xz}] + \dots \end{aligned} \tag{B.29}$$

Similar expressions would be obtained for $u_{aa}(r_{yy}, \psi_{yy})$ and $u_{aa}(r_{zz}, \psi_{zz})$, and when summing over all nearest neighbor interactions, one can fully express the magnetoelastic energy as

$$\begin{aligned} u_{me} =& B_1\big[e_{xx}\alpha_1^2 + e_{yy}\alpha_2^2 + e_{zz}\alpha_3^2 - \frac{1}{3}(e_{xx} + e_{yy} + e_{zz})\big] \\ &+ B_2\big[e_{xy}\alpha_1\alpha_2 + e_{yz}\alpha_2\alpha_3 + e_{xz}\alpha_1\alpha_3\big], \end{aligned} \tag{B.30}$$

where, for a given atomic density number ρ_a, $B_1 = \rho_a l'(r_0)$ and $B_2 = 2\rho_a l(r_0)$. The magnetoelastic constants to a material's equilibrium dipole-dipole interaction $l(r_0)$. More complex structures such as BCC or FCC crystals will have constants B_1 and B_2 in some linear combination of $l(r_0)$ and $l'(r_0)$ [16]. By substituting this expression into Eq. B.24 and minimizing the energy with respect to strain, yields the equilibrium magnetostrictive tensor

$$\lambda_{ij} = \begin{pmatrix} -\frac{B_1}{c_{11}-c_{22}}\left(\alpha_1^2 - \frac{1}{3}\right) & -\frac{B_2}{c_{44}}\alpha_1\alpha_2 & -\frac{B_2}{c_{44}}\alpha_1\alpha_3 \\ -\frac{B_2}{c_{44}}\alpha_1\alpha_2 & -\frac{B_1}{c_{11}-c_{22}}\left(\alpha_2^2 - \frac{1}{3}\right) & -\frac{B_2}{c_{44}}\alpha_2\alpha_3 \\ -\frac{B_2}{c_{44}}\alpha_1\alpha_3 & -\frac{B_2}{c_{44}}\alpha_2\alpha_3 & -\frac{B_1}{c_{11}-c_{22}}\left(\alpha_3^2 - \frac{1}{3}\right) \end{pmatrix} \tag{B.31}$$

These values represent the various strains that develop in a cubic crystal under a saturation magnetization direction α. The strain for a specific direction β is found by evaluating

$$\begin{aligned} \lambda = &- \frac{B_1}{c_{11} - c_{22}}\left(\alpha_1^2\beta_1^2 + \alpha_2^2\beta_2^2 + \alpha_3^3\beta_3^3 - \frac{1}{3}\right) \\ &- \frac{B_2}{c_{44}}(\alpha_1\alpha_2\beta_1\beta_2 + \alpha_2\alpha_3\beta_2\beta_3 + \alpha_1\alpha_3\beta_1\beta_3) \end{aligned} \tag{B.32}$$

One can obtain characteristic saturation strictions along major cubic directions using

Eq. B.32:

$$\lambda_{100} = -\frac{2}{3}\frac{B_1}{c_{11} - c_{12}} \tag{B.33}$$

$$\lambda_{111} = -\frac{1}{3}\frac{B_2}{c_{44}} \tag{B.34}$$

$$\lambda_{110} = \frac{1}{4}\lambda_{100} + \frac{3}{4}\lambda_{111} \tag{B.35}$$

More generalized expressions can be obtained for crystals of other symmetry by selecting special coefficients that possess symmetry-invariance, as detailed in the work by Callen and Callen [79].

B.4.1 Preliminary modelling of FSMA Magnetostriction

The discovery of large magnetostriction of Ni_2MnGa in 1996 demonstrates a newer kind of magnetoelastic coupling that involves the motion of twin boundaries as a response to the magnetic field [8]. The Zeeman energy of a crystal is the energy introduced into it by application of an external field, and is expressed by

$$u_{Zeeman} = -\mu_0 \mathbf{M} \cdot \mathbf{H}_{ext} = -\mu_0 M_s H \cos\theta \tag{B.36}$$

O'Handley put forth a simplified model for the motion of twin boundaries by evaluating energy differences across twin boundaries as a function of field according to different relative strengths of the Zeeman energy to the anisotropy and elastic energies [37]. His model uses twin geometry, defined by the angle of one variant with respect to the field, θ, by the angle of that variant with respect to the

other, ϕ. Given a 2D material of two 90° twin variants, magnetized along the direction of variant 1 such that $\theta = 0$, an effective twin boundary stiffness C, a transformation strain e_0, and strains corresponding to differing twin volume fractions of $f_1 = \frac{1}{2} + \delta f$, and $f_2 = \frac{1}{2} - \delta f$ such that $e_x = e_0 f_2 \sin\phi = e_0(\frac{1}{2} - \delta f)$ and $e_y = e_0(f_1 + f_2 \cos\phi) = e_0(\frac{1}{2} + \delta f)$, the relevant free energy of the terms become

$$u = u_{Zeeman} + u_{elastic} + u_{anisotropy} \tag{B.37}$$

$$\begin{aligned} u = &-\mu_0 M_s H[f_1 \cos\theta + f_2 \cos(\theta + \phi)] \\ &+ \frac{1}{2} C e_0^2 [(\frac{1}{2} - \delta)^2 + (\frac{1}{2} + \delta f)^2] + f_2 K_u \cos^2(\theta + \phi) \end{aligned} \tag{B.38}$$

which reduces to

$$\begin{aligned} u = &-\mu_0 M_s H \left[\frac{1}{2} + \delta f + \left(\frac{1}{2} - \delta f\right)\cos\phi\right] \\ &+ \frac{1}{2} C e_0^2 \left[\frac{1}{2} + 2\delta f^2\right] + \left(\frac{1}{2} - \delta f\right) K_u \cos^2\phi \end{aligned} \tag{B.39}$$

Equilibrating with respect to the magnetization angle ϕ and the changing volume fraction δf gives

$$\cos\psi = \frac{\mu_0 M_s H}{2K_u} \tag{B.40}$$

$$\delta f = \frac{\mu_0 M_s H - \mu_0 M_s H \cos\psi + K_u \cos^2\psi}{2C e_0^2} \tag{B.41}$$

One can introduced reduced field terms $h_a = \frac{\mu_0 M_s H}{2K_u}$ and $h_e = \frac{\mu_0 M_s H}{C e_0^2}$ to simplify the expressions to

$$\cos\psi = h_a \tag{B.42}$$

$$\delta f = \frac{h_e}{2}(1 - \frac{h_a}{2}) \tag{B.43}$$

These equations can be used in reduced expressions of the magnetization and strain such that

$$\begin{aligned} m = \frac{M}{M_s} &= f_1 + f_2 \cos\psi \\ &= \frac{1}{2}\left[1 + h_a + h_e(1 - h_a)\left(1 - \frac{h_a}{2}\right)\right] \end{aligned} \tag{B.44}$$

$$e_x = \frac{e_0}{2}\left[1 - h_e\left(1 - \frac{h_a}{2}\right)\right] \tag{B.45}$$

$$e_y = \frac{e_0}{2}\left[1 + h_e\left(1 - \frac{h_a}{2}\right)\right] \tag{B.46}$$

These relations depict strong non-linear relationships for the magnetization and strain as a function of field characterized by the reduced field terms h_a and h_e, which represent the ratio of the Zeeman energy to that of the anisotropy and elastic energy, respectively. The physical interpretation is that a material of low anisotropy, $h_a \gg 1$, magnetizes easily and at low fields. The low strength of these fields typically does not generate enough Zeeman energy to induce twin boundary motion; thus $h_{e,s}$ and e tend to be low. Materials of large anisotropy, $h_a \ll 1$, cause the h_a terms to vanish, at which point h_e dictates the extent to which a field is resisted by the stiffness of the twin boundary. In this case, the strain e has approximately

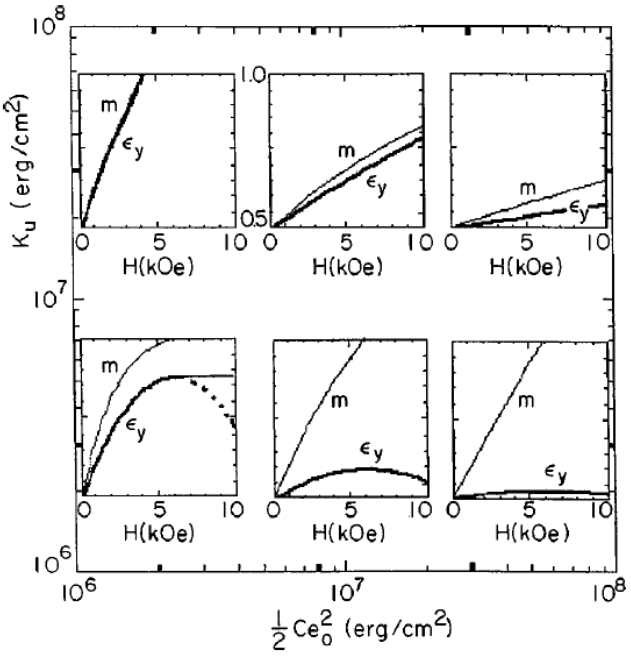

Figure B.4: Taken from [37], theoretical magnetization and magnetostriction curves generated by O'Handley's model for various chosen values of the anisotropy, K_u, and elastic constants, $1/2\ Ce_0^2$.

linear dependence of the field. For intermediate anisotropies, non-linear behavior develops and depends strongly on the ratio between the anisotropy and elastic energy, h_e/h_a, and several examples of what can be expected are shown in Figure B.4. This model does well illustrating the concepts of enhanced magnetostriction through twin boundary motions, but the simplifications made which ignore strain in the z-direction, the possibility of several twin variants, and temperature dependence of the material parameters make it unsuitable to accurately simulate all FSMA behavior.

Appendix C: Studies on FePd

C.1 Background on FePd - Premartensitic Phenomena

The elastic properties of Fe-Pd binary alloys near the 30-35 atomic % Pd range were extensively studied in the late 1980s and early 1990s for unusual martensitic shape memory properties. The martensite was first discovered in 1980 [10], developing as a metastable twinned disordered face-centered tetragonal (FCT) crystal structure when quenching from a high temperature homogeneous disordered FCC γ-phase rather than the more thermally stable BCT phase as shown in the phase diagram in Figure C.1 [80]. The transformation temperature has a large dependence on the atomic concentration of Pd, and near-room temperature transformations can ben expected in the 30-32 atomic % Pd range. What garnered specific interest in the elastic properties of these FePd alloys was first documented in 1986 by Sugiyama through TEM studies of the evolution of the martensite, shown in Figure C.2 [11]. Through these micrographs, it was noted that while in the nominal parent FCC austenite, striations along $\langle 110 \rangle$ directions appear in a cross-hatched pattern, earning the nickname tweed for its resemblance to the jacket fabric. This premartensitic behavior also imparts pseudo-second order transformation behavior to the martensite, and this can more readily be seen in the X-ray data of Seto [12],

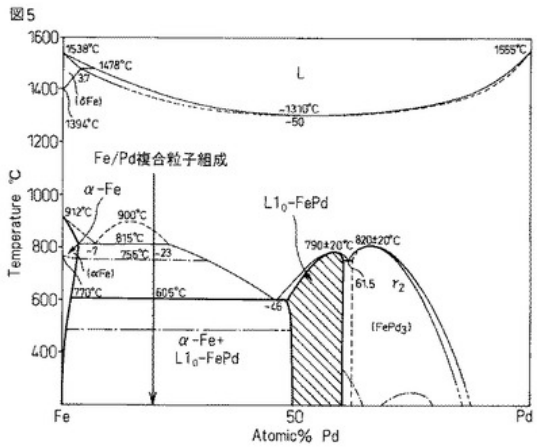

Figure C.1: Taken from [80], the binary phase diagram of Fe-Pd.

shown in Figure C.3, or the smearing peak reflections seen in synchrotron radiation measurements [18]. The measurements show how the trace of the cubic lattice parameter continuously changes in second-order fashion before an abrupt transition at the transformation temperature. Additionally, one can also observe in the XRD an intermediate phase emerges in a small temperature range of about 5 K, which Khachaturyan established as an adaptive martensite phase, whereby twins coalesce into nano-modulations with a 2:1 ratio to accommodate larger lattice strains between the parent FCC and martensite FCT phase [13]. These modulations give rise to a superlattice reflection in the XRD, making it appear as if a orthorhombic phase manifests, and this phenomenon only occurs in those martensites possessing unusually low surface energy across twin boundaries.

The magnetic behavior of FePd was ignored in these early studies, however, and only recently has the connection between the magnetic contributions to the martensitic behavior of FePd been looked into. In 2014, Gruner published DFT results that highlighted that the magnetic contributions to the binding energies of

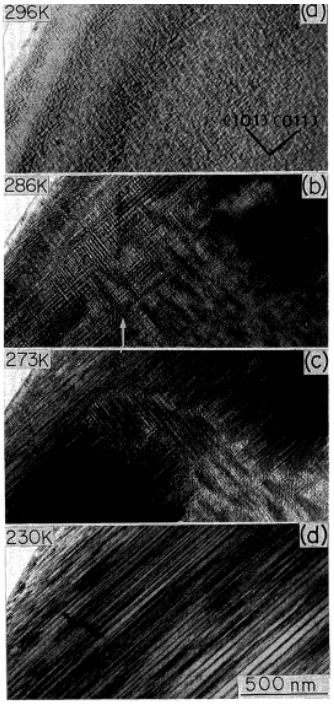

Figure C.2: Taken from [11], a series of TEM micrographs taken of FePd as it changes through its martensitic transformation temperature.

the twinned FCT crystal are what serve to stabilize this phase through a lower energy barrier transformation path over the more stable BCT phase, shown in the Bain path diagram in Figure C.4 [60]. Furthermore, it was found that the twinning is a natural consequence of these magnetic contributions as a means to minimize the magnetostatic energy of the crystal. These results suggest that the elastic softening assists the material in minimizing the surface energy across twin boundaries needed to contain the magnetic energy, and that elastically twinned domains are in actuality magnetoelastic domains separating magnetic and elastic information simultaneously.

C.2 Past results on FePd

Understanding the importance of the magnetic contributions to the development of the unusual martensitic properties of FePd, it became clear the magnetic properties must be properly characterized. All studies were performed on single crystals of composition $Fe_{68.8}Pd_{31.2}$. Thermal expansion curves in a temperature range from 233 to 343 K were taken by mounting a [100] disk with a strain gauge along the [010] direction atop a PID-controlled Peltier device in a custom-made evacuated stage suspended in an electromagnet. This same set-up was used to measure magnetostriction through a series of temperatures as well on a [100] disk with strain gauge mounted along either [010/001] and [011/01$\bar{1}$] directions. Magnetization curves along different crystalline directions: [010],[1$\bar{1}$0], and [1$\bar{1}$1] were taken of the crystal with a [110] normal using a vibrating sample magnetometer (VSM). Magnetic anisotropy measurements as a function of field at room temperature and at a saturation field as a function of temperature were taken on a [110] disk mounted to a controlled-rotation platform within a VSM.

The thermal expansion results are shown in Figure C.5. From them, one can see a clear transition occurring near 250K, with a transition region approximately 5K wide. The data itself closely resembles the change in the cubic lattice parameter a_c seen in the XRD data of Figure C.3. The transition is a clear sign for the FCC to FCT martensitic transformation. In addition, there exists an extensive invar region from 260-300 K temperature range which can be attributed to the presence of premartensitic tweed giving rise to complex expansion-accommodating

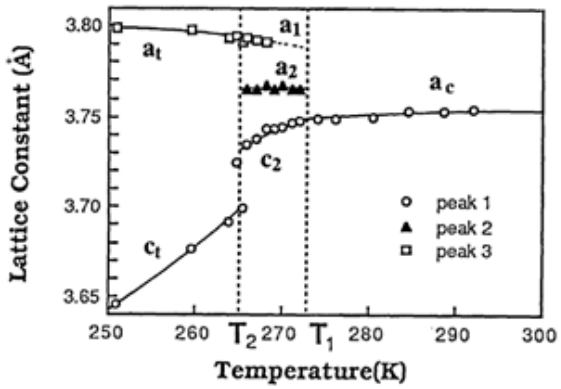

Figure C.3: Taken from [12], the measured lattice parameters of FePd as a function of temperature.

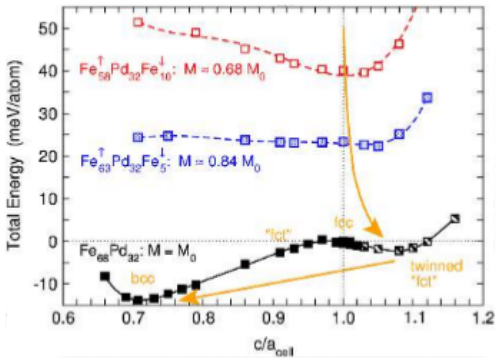

Figure C.4: Taken from [60], a binding energy evaluation of FePd along Bain strains corresponding to different crystal of lower symmetry.

microstructures, such as has been observed in FeNi [81].

The magnetostrictive response of $Fe_{68.8}Pd_{31.2}$ is again shown in Figure C.6 for a series of temperatures moving through the phase transformation, from 258 to 240 K, with transformation temperatures at 250 and 245 K. The data shown in figure 2.1d, with the field applied along the [011] direction shows the transformation very clearly, with an intermediary value of saturation magnetostriction $\lambda_{\parallel-\perp}$ demonstrating the emergence of the adaptive martensite. The slight discrepancy between these temperatures and the transformation temperature from the thermal expansion arises

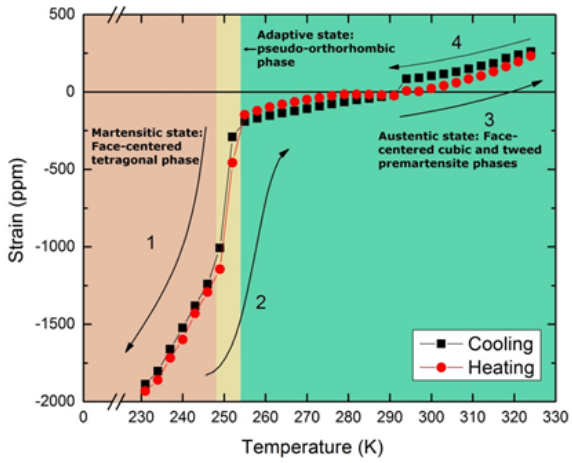

Figure C.5: Thermal expansion data taken along a ⟨100⟩ direction in a single crystal of $Fe_{68.8}Pd_{31.2}$ with different phases labelled in their respective temperature region.

from instrumental error. The values of the magnetostriction reach quite large values of 300 ppm in the austenitic state as compared to other FSMAs, an attribute due to the presence of the premartensitic tweed. In the austenitic state, the saturation magnetostriction is also isotropic with respect to a field applied either along a [010] or [011] direction. It can be also seen that the values of magnetostriction change close to the transition temperatures, indicating the possibility of short-range strain ordering occurring within the structure in anticipation of the displacive transformation. This is related to distortions caused by nano-platelet precipitates of the tetragonal phase beginning to coalesce and drive the transformation [82]. The data for magnetic saturation shown in Figure C.6d is fitted with an exponential decay function with an adjusted R^2 value of 0.967. The quality of this fit serves as an indication of short-range ordering leading up to the phase transformation.

Magnetization curves taken at room temperature along [010],[$1\bar{1}0$], and [$1\bar{1}1$] directions are shown in Figure C.7. The behavior is linear approaching saturation,

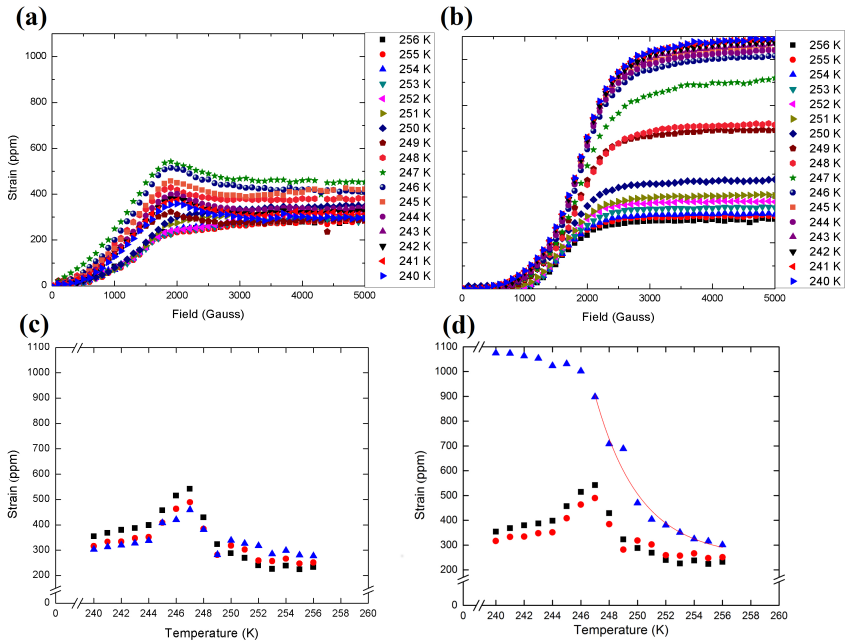

Figure C.6: Magnetostriction data shown for single crystal $Fe_{68.8}Pd_{31.2}$ at several different temperatures along the **(a)** $\langle 100 \rangle$ and **(b)** $\langle 110 \rangle$ crystalline directions as a function of field. The same data is shown as a function of temperature at select fields ■ 1900 Oe, ● 2500 Oe, and ▲ 4000 Oe, along the **(c)** 100 and **(d)** 110 crystalline directions. An exponential fit with adjusted R^2 of 0.967 is shown in **(d)** for the 4000 Oe data above 247 K.

possesses no hysteresis, and is independent of crystalline direction. The coercive force is very small and measures 0.05 Oe. Curves were measured in a temperature range from 255-360 K, though these are not shown since the behavior along this region shows no appreciable changes. That is to say, the behavior is persistent up to 100 K above the transformation temperature, and furthermore, the plot in Fig. C.7b shows the behavior also remains unchanged with cycling. Typically, a magnetic response such as this reflects a mechanism by which all ferromagnetic domains in the sample are pinned, meaning the spins can only rotate towards the applied field, a fact which could only be true if the material lacked crystallinity, e.g. metglass. This is not the case for $Fe_{68.8}Pd_{31.2}$. Instead, the evidence points towards an isotropic

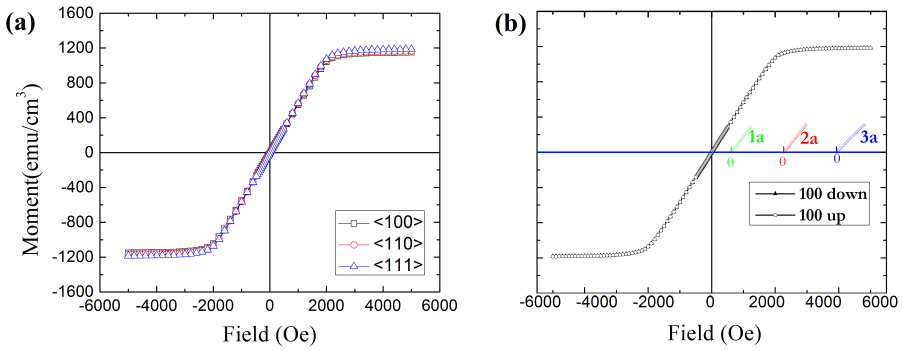

Figure C.7: Magnetization curves taken at 293K for **(a)** several crystal directions and **(b)** over several hysteresis loops, 1a, 2a,and 3a, of increasing (up) and decreasing (down) field, offset for clarity, for single crystal $Fe_{68.8}Pd_{31.2}$.

demagnetization field, and we propose this is a consequence of ultra-low anisotropy caused by the manifestation of premartensitic tweed.

As such, it became important to gauge the anisotropy as a function of field and temperature, with results of magnetic torque data shown again in Figure C.8. From the data, the magnetocrystalline anisotropy energy density equals less than 10^2 J/m^3 in the linear region and is about 425 J/m^3 at saturation, a value smaller than some metglasses. At low fields, the torque characteristic of $Fe_{68.8}Pd_{31.2}$ exhibits a 2-fold symmetry, which develops into a superposition of 2- and 4-fold symmetry at higher fields. That is, the premartensitic tweed likely gives rise to a tetragonal 2-fold symmetry, and it's possible that by de-twinning in response to the field, some of the tweed reforms back into a cubic structure, causing a stronger 4-fold symmetry component to appear, indirectly supporting that the magnetization and magnetostriction are a result of a twinning/de-twinning mechanism. We fitted the data using an $A\sin 4(\theta+\varphi_1) + B\sin 2(\theta+\varphi_2)$ model and Origin software to look at the relative contribution of each symmetry component to the overall torque,

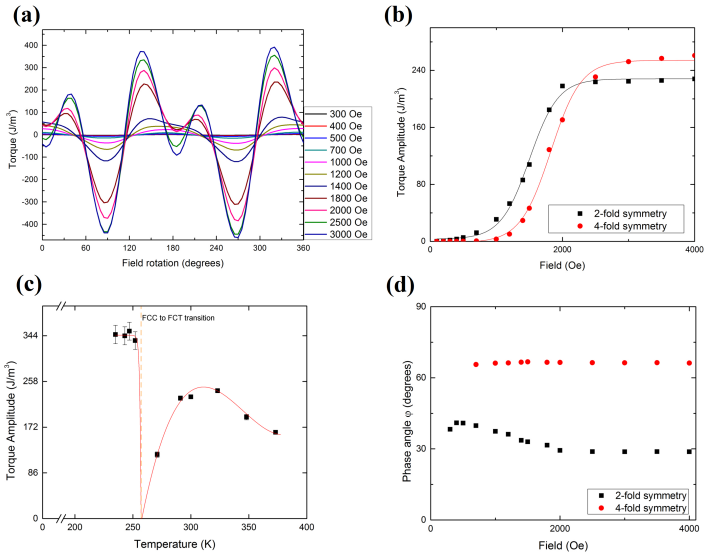

Figure C.8: **(a)** Magnetic torque data of several field strengths taken at 293K for single crystal $Fe_{68.8}Pd_{31.2}$, **(b)** change of torque amplitudes A and B fitted to $A\sin 4(\theta+\varphi_1)+B\sin 2(\theta+\varphi_2)$ for curves of **(a)** to separate the anisotropy behavior of the ■2-fold symmetry and ●4-fold symmetry, **(c)** temperature dependence of the 2-fold symmetry with applied field of 3000 Oe, and **(d)** change in phase angles φ_1 and φ_2 as a function of field for curves in **(a)**.

shown in Fig. C.8b. The 2-fold symmetry is a superposition of both the shape anisotropy and an intrinsic 2-fold symmetry. Shape anisotropy accounts for slight differences in the demagnetization factor for orthogonal axes of a non-perfect circle. That is, any amount of ellipticity will contribute a shape anisotropy to the overall system, but for disk-shaped samples it is often negligible. However, $Fe_{68.8}Pd_{31.2}$ possesses an unusually low anisotropy energy which means it would be erroneous to discount the contribution of shape anisotropy. We believe this is the case because the response of the amplitude for the 2-fold symmetry as a function of field follows a quadratic pattern, fitted with an adjusted R^2 value of 0.992. This shape anisotropy is independent of temperature, but we also show in Fig. C.8c that the amplitude of the 2-fold symmetry has strong temperature dependence, exhibiting a sharp drop

before the phase transformation temperature of this material. Such behavior is also seen in a cubic to monoclinic transition for Fe_3O_4 [83]. Hence we conclude some premartensitic 2-fold crystal symmetry contributes strongly to the magnetic behavior of the system even in the austenitic phase. We assume the remnant 2-fold component of anisotropy at the drop at 271 K accounts for the shape anisotropy of our system, totaling ~ 120 J/m^3. This corresponds to a difference of 1.40×10^{-3} in the biaxial demagnetization factors, which amounts to a deviation of 0.1% or 5 μm around the perimeter of the disk. It is unusual for a material to exhibit an anisotropy so highly dependent on the magnetic field, but this can be reconciled by considering the anisotropy is a manifestation of both a regular magnetic component, K_m and a magnetoelastic component K_{me}. We also show the change in phase angles φ_1 and φ_2 in Figure C.8d as a function of field. The cubic phase angle φ_1 remains constant whereas the tetragonal phase angle φ_2 experiences a continuous shift from 43° to 30° as the field increases from 1000 to 2000 Oe, at which point it becomes constant due to magnetic saturation. This shift is another sign of the magnetic field rearranging and ordering the premartensitic tweed.

The magnetization behavior in FePd is closely tied to the microstructural rearrangements that come from these twinning and de-twinning processes in response to the magnetic field. The fact that this behavior is isotropic with respect to crystalline direction means that the twins, carrying magnetic information, arrange themselves in such a manner as to perfectly magnetize and demagnetize themselves to any applied field. FePd is unique in that this behavior exists in the austenitic state due to premartensitic tweed acting as twin-like entities in the material. An additional mag-

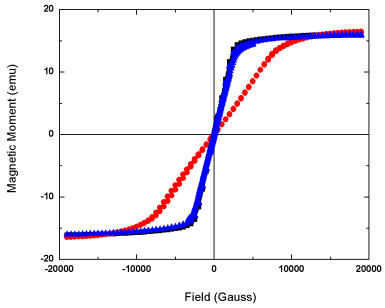

Figure C.9: Magnetization curves for single crystal $Fe_{68.8}Pd_{31.2}$ taken along in-plane directions of [001] (black ■) and [1$\bar{1}$1] (blue ▲) as well as the out-of-plane [110] normal (red ●).

netization curve is shown in Figure C.9, demonstrating that the crystalline isotropic response may be broken by applying a field out of plane or normal to the disk rather than in the plane. In fact, this reveals that sample geometry almost entirely determines the slope of the magnetization curve. This comes back to the fact that this behavior perfectly mimics the classical theory for the magnetization of a pinned, single domain with a perpendicularly applied field [84] whose magnetization behavior is modelled through the expression

$$\boldsymbol{M} = M_s \cos\alpha = \frac{H}{2N}, H < H_d \tag{C.1}$$

,

where $\boldsymbol{M}$ denotes the magnetization vector, M_s is the saturation magnetization, H is the applied field, N is the demagnetization factor–dictated by sample geometry–and H_d is the demagnetization field, below which the sample is unsaturated. This equation describes the magnetic response of FePd quite well. The slope of the magnetization curves give a demagnetization factor of 0.071, which matches

closely to the theoretical value of 0.081 for our disks with aspect ratio 5:1 [36].

Since materials which exhibit solely rotational magnetic responses typically possess no crystalline structure, the de-twinning magnetic response of crystalline $Fe_{68.8}Pd_{31.2}$ is a mechanism that mimics domain rotation. This is made possible through highly mobile twins in premartensitic tweed clusters which exist to minimize the magnetostatic energy and demagnetize the material when no external field is applied. Without any field applied, the twins within these clusters are arranged such that the average magnetization angle, $\langle \cos \alpha \rangle$, equals 0. Twin rearrangement and detwinning induced by an external field causes this average to deviate between 0 and 1 until saturation, upon which these magnetoelastic twins are eliminated from the cluster and the bulk of the sample fully magnetizes. If each twin is separated by a boundary of γ_{me} surface energy, one can formulate the energetics of the material system with the expression

$$E = nA\gamma_{me} + V(E_{elastic} + E_{magnetostatic} + E_{magnetoelastic} + E_{anisotropy}) \tag{C.2}$$

where n is the number of interfaces in the system, A is the interfacial area of each twin, and V is the volume of a twin. Assuming the anisotropy energy is very low and therefore negligible, along with a sample with total volume L^3, subdivided into

n twins of thickness t each, this becomes

$$E = nL^2\gamma_{me} + \frac{L^3}{n}(E_{elastic} + E_{magnetostatic} + E_{magnetoelastic}) \tag{C.3}$$

To simplify, we factor out the area L^2. We approximate the magnetoelastic energy as some elastic constant multiplied by the strain induced by destroying an interface, or detwinning, caused during magnetization. The magnetostatic energy is the dot product of the magnetization with both its internal field and the applied external field, and the resultant expression becomes

$$E = n\gamma_{me} + \frac{L}{n}(-\mu_0 \boldsymbol{M} \cdot (\boldsymbol{H_d} + \boldsymbol{H_{ext}}) + G(\lambda^2) \tag{C.4}$$

where μ_0 is the permittivity of free space, $\boldsymbol{H_{ext}}$ is the applied external field, G is an elastic constant, and λ is a magnetoelastic strain. The demagnetization field is equal to the negative of the saturation magnetization M_s, modified by the demagnetization factor N depending on the sample geometry. The overall magnetization may be expressed as the saturation magnetization with respect to the angle of magnetization, α, as well, resulting in

$$E = n\gamma_{me} + \frac{L}{n}(-\mu_0 M_s(-NM_s\cos\alpha + H_{ext})\cos\alpha + G(\lambda^2). \tag{C.5}$$

Rearranging terms and equilibrating with respect to n and α gives

$$n = \sqrt{\frac{L(G\lambda^2 + N\mu_0 M_s^2 \cos^2\alpha - \mu_0 M_s H_{ext}\cos\alpha)}{\gamma_{me}}} \tag{C.6}$$

and

$$2NM_s \cos\alpha = H_{ext}. \tag{C.7}$$

If there is no applied field, and assuming a random starting distribution of magnetization angles such that $\langle\cos^2\alpha\rangle = 1/2$, then

$$n_0 = \sqrt{\frac{L(G\lambda^2 + \frac{1}{2}N\mu_0 M_s^2)}{\gamma_{me}}}, \tag{C.8}$$

Recognizing that $M_s \cos\alpha$ is simply $\boldsymbol{M}$, the equilibrium condition of equation (6) tells us that

$$M = \frac{H_{ext}}{2N}, \text{ if } H_{ext} < H_d, \tag{C.9}$$

which again is the same expression as in (C.1).

Appendix D: Studies on FeNi

D.1 Background on FeNi - Adaptive Martensite

FeNi alloys fabricated within the 30-38 atomic % Ni range representing an interesting parallel to the magnetostriction of FePd and FeGa in terms of their invar expansion properties. The invar effect, a temperature region with near-zero thermal expansion, has origins tied to magnetic anomalies [85] as well as complex ordered and martensitic microstructures that provide a compensatory thermal contraction to compete against linear thermal expansion coefficients of constituent phases present in these alloys [58, 81]. Achieving the invar effect in these alloys requires careful annealing in a two-phase α and γ phase region, followed by quenching and low-temperature tempering treatments to tailor the compensatory effect. The γ phase becomes unstable below the $\alpha/L1_2$ eutectic, and a quench induces a $\gamma - \alpha'$ martensitic transformation. Cold-working these alloys also affects the thermal expansivity behavior and offers an alternative method to tailor the invar properties.

Recently, Rao et al. demonstrated the applicability of phase field microelasticity (PFM) modelling towards the Fe-Ni system as proof of concept in explaining the invar effect [58]. PFM is a thermodynamic computational technique that evaluates elastic contributions to the free energy from such sources as point-defects, dislo-

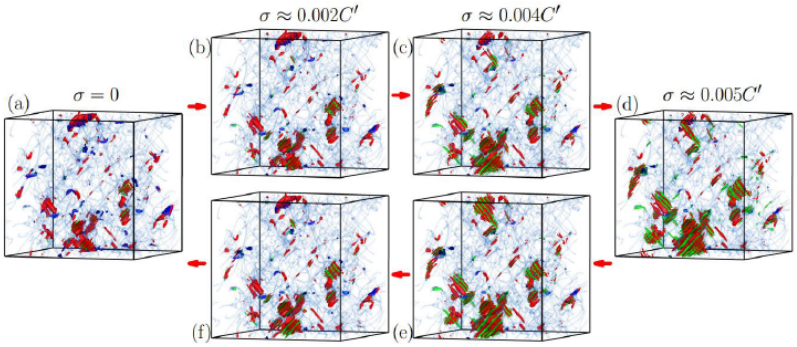

Figure D.1: Taken from [58], simulated microstructure of an $Fe_{65}Ni_{35}$ alloy obtained through phase field microelasticity calculations based on a randomly generated initial state of dislocations and applied stress proportional to the elastic constant C'.

cations, second-phase precipitates, and martensitic transformations. It takes into account size-dependent parameters, and because of this, it is possible to calculate theoretical microstructures for a material wholly on the basis of energy minimization. The results of Rao et al.'s work indicate that stress-generating defects naturally present in martensitic materials such as Fe-Ni tend to induce local martensitic transformations around the defect sources. The phenomenon is, in essence, a localized application of the Clausius-Clapeyron equation raising T_{MS} inhomogeneously and preferentially about these stress-centers. The formation of these nanoscale martensitic embryos facilitates adaptive growth and shrinkage in response to external stimuli, such as stress or a magnetic field. An example of this is shown in Figure D.1, where the introduction of external stress term shows reversible growth and shrinkage of the martensite through a theoretical stress cycle. In terms of PFM, a change in temperature or application of a magnetic field has an equivalent elastic energy term reflected within the model, meaning similar microstructures develop in response to

thermal or magnetic environmental changes. This they claim implies the invar effect is an adaptive response of FeNi to resist elastic energy changes during thermal expansion by instead growing martensite to maintain constant volume. This section contains experimental studies done on differently processed FeNi alloys to provide experimental evidence verifying this theory.

D.2 Completed studies of FeNi

Knowing the importance of processing conditions in generating adaptive martensite structures within FeNi, we have carried out studies on differently processed samples from a single sheet of polycrystalline $Fe_{65}Ni_{35}$: one in the as-received (AR) state, one cold-rolled to a 50% reduction in thickness (CR), and one quenched from room temperature to liquid nitrogen temperatures (LN). For each sample, thermal expansion, magnetization at room temperature and above, magnetostriction as a function of temperature, and SEM micrography have been carried out. Because these samples are polycrystalline with no known pre-texture, isotropic behavior for the magnetization and magnetostriction is expected, and an enhancement of the magnetization and magnetostriction is expected for the FeNi-CR and FeNi-LN samples as compared to the FeNi-AR one.

The thermal expansion results for the three alloys are shown in Figure D.2 over a temperature range fof 233-378K. In each case, a strong thermal contraction with increasing temperature is seen, which attests to a crystal possessing excess premartensite reverting back to a more thermally stabilized cubic state [58]. No

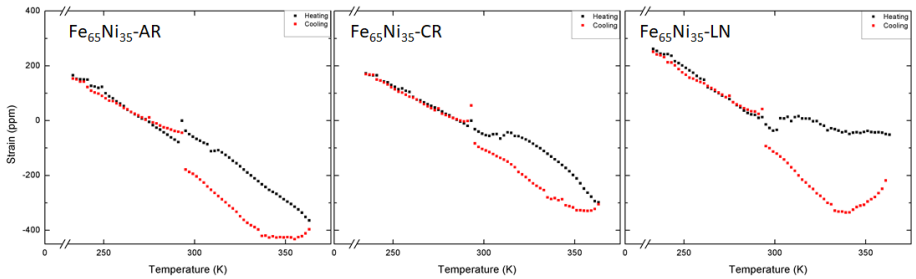

Figure D.2: Thermal expansion curves within a range of 233-378 K taken for as-received (AR), cold-rolled (CR), and liquid N_2 quenched (LN) $Fe_{65}Ni_{35}$ polycrystalline alloys.

well-defined first-order martensitic transformation occurs, which would otherwise be captured by a sharp jump in the data, as seen for $Fe_{68.8}Pd_{31.2}$ in Fig. C.5. Only the FeNi-LN sample shows a region of significant invar expansion, from 308-378 K, but all alloys show extensive hysteresis when cooling from 378 K to room temperature. The cause of the hysteresis is nebulous, since it is expected that the formation of nanoscopic premartensites leads to highly reversible transformations, which should imply the same forward and reverse paths when cycling the temperature. Instead, it may be the case that the microstructure evolves unpredictably when cooling from a higher temperature, such that premartensite might be eliminated through heating and reform in a different configuration when it becomes restabilized at colder temperatures. These data are also at odds with Rao's, as a higher amount of plastic strain as in the case of FeNi-CR should lead to a sharper thermal contraction from the increase in plastic strain, but the contraction is about equal. Furthermore, a contraction this sharp below room temperature would indicate alloys of $> 10\%$ pre-applied plastic strain which, in turn, is predicted to increase T_{MS} to near 330K, none of which is evidenced by these results.

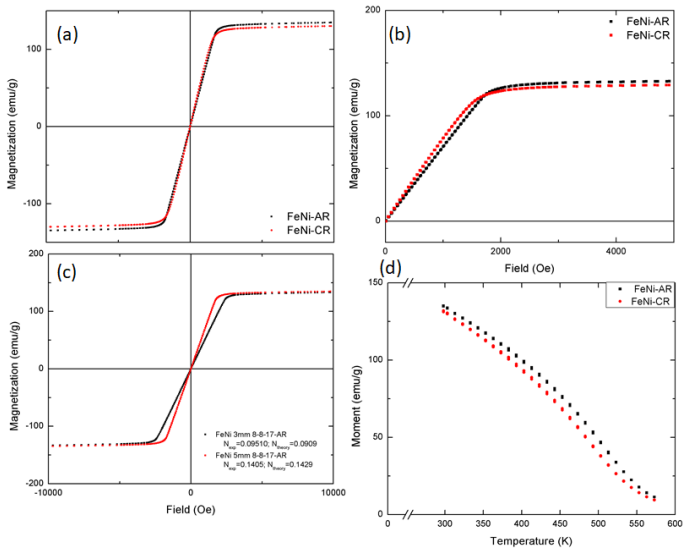

Figure D.3: **(a)** Magnetization curves taken at room temperature for the as-received (AR) and cold-rolled (CR) $Fe_{65}Ni_{35}$ polycrystalline alloys along with **(b)** a zoomed in scaling to observe the anhysteretic approach to and from saturation. **(c)** Magnetization curves for two FeNi-AR disks of different geometries with a comparison between the theoretical demagnetization for those samples and the factor obtained from the slope of the curves. **(d)** Saturation magnetization measurements taken as a function of temperature for the FeNi-AR and FeNi-CR samples.

Several different magnetization measurements are shown in Figure D.3, with data omitted for the FeNi-LN sample. The reason for this omission is that the FeNi-LN sample showed no appreciable difference in behavior as compared to the FeNi-AR sample, which is a sign the quench did not affect the magnetic behavior of the sample in any way despite affecting the thermal expansion. Also omitted were data for longitudinal and transverse magnetization for the FeNi-CR sample with respect to the rolling direction; these data showed no appreciable difference, indicating that the possibility of texturing due to rolling did not affect the isotropic magnetization. Both the FeNi-AR and -CR sample exhibit magnetization remarkable similar to $Fe_{68.8}Pd_{31.2}$, linear until saturation and anhysteretic within the sensitivity limit of the VSM. The ultimate magnetic saturation is less for the CR sample than for

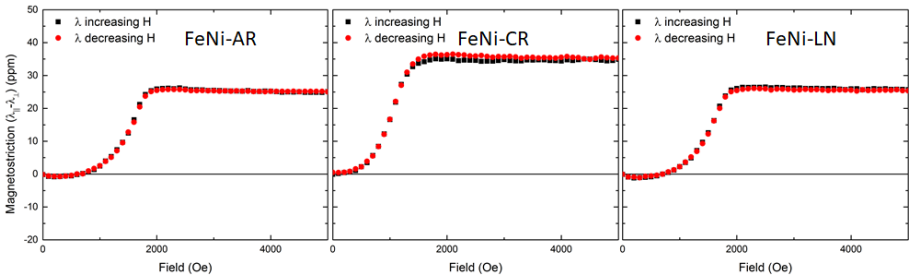

Figure D.4: Overall ($\lambda_{\parallel} - \lambda_{\perp}$) magnetostriction curves taken at room temperature for as-received (AR), cold-rolled (CR), and liquid N_2 quenched (LN) $Fe_{65}Ni_{35}$ polycrystalline alloys.

the AR, contrary to expectations, though the difference is about 3.5% between 134 emu/g opposed to 130 emu/g. The data in Fig. D.3c also demonstrates that the shape of the magnetization curve depends heavily on the demagnetization factor for the applied field direction. The slopes of the curves for an in-plane magnetized 3 mm diameter disk and 5 mm diameter disk, both 1 mm in thickness corresponding very closely with theoretical demagnetization factor values estimated from [36]. This alludes to a significantly reduced magnetic anisotropy as observed in $Fe_{68.8}Pd_{31.2}$. The magnetization as a function of temperature, shown in Fig. D.3d, has a very gentle approach towards zero with an anomalous slope change near 550K , similar to behavior seen by Gorría et al. for a $Fe_{64}Ni_{36}$ alloy which had a T_c of 500 K [86]. Their work demonstrated considerable enhancement of T_c to 620 K by high energy ball milling, of which we observe no similar phenomenon for the FeNi-CR sample. The small tail of weak magnetization for T >550 K indicates short range magnetic ordering in the paramagnetic phase [16].

The magnetostriction data at room temperature for the three alloys are shown in Figure D.4, and the saturation magnetostriction $\lambda_{\parallel-\perp}$ as a function of temperature

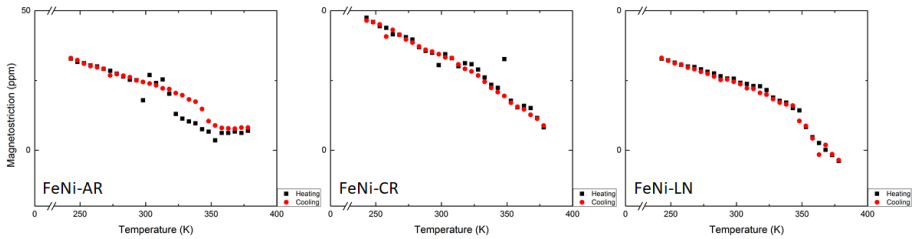

Figure D.5: Saturation magnetostriction data plotted as a function of temperature for as-received (AR), cold-rolled (CR), and liquid N_2 quenched (LN) $Fe_{65}Ni_{35}$ polycrystalline alloys.

is shown in Figure D.5. From Fig. D.4, no apparent difference is seen between the magnetostrictive response of the AR and LN sample, having a magnitude of 28 ppm, not significantly higher than that found in pure Fe of 20 ppm [16]. The CR sample shows a significantly higher magnetostriction of 35 ppm, or a 25% increase, which may be attributable to a larger presence of premartensite in the alloy formed from the cold-rolling process, though this observation is at odds with the lack of such a significant change seen for the sample in the thermal expansion data. All samples exhibit a quadratic dependence of λ with respect to field, and, though not shown, the majority of magnetostriction curves show $\lambda_{\parallel} = \frac{2}{3}\lambda_s$ and $\lambda_{\perp} = -\frac{1}{3}\lambda_s$. This suggests Joule magnetostriction responses for these materials, not one of strong magnetoelastic coupling to martensitic structures. The temperature dependence of magnetostriction for the three samples is quite different. Both the AR and LN sample experience anomalous slope changes near 350 K that aren't readily accounted for in either the thermal expansion or magnetization versus temperature data. This makes it difficult to say whether the origin is due to structural changes, magnetic changes, or microstructural changes. However, the LN sample has no hysteresis between measurements made during cooling or heating cycles, as opposed to the

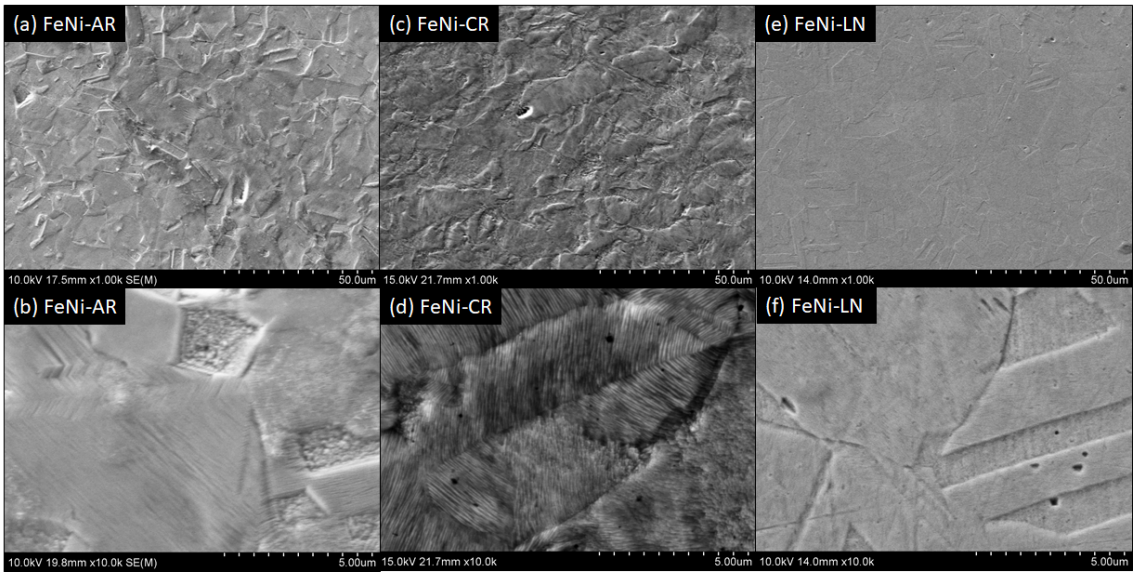

Figure D.6: SEM micrographs obtained at low (1000x) and high (10000x) magnifications for the **(a)(b)** as-received (AR), **(c)(d)** cold-rolled (CR), and **(e)(f)** liquid N_2 quenched $Fe_{65}Ni_{35}$ polycrystalline alloys.

AR sample, indicating perhaps the LN sample has more 'frozen'-in premartensite such that its microstructure between the thermal cycling remains more constant than that of the AR sample's. The CR sample does not show this slope change, meaning the extra plastic deformation has some sort of quenching effect whatever the transition mechanism may be.

SEM micrographs for the samples at 1000x and 10000x magnifications are shown in Figure D.6. Each sample was mechanically polished and etched with 3 successive 20s applications of aqua regia to elucidate the microstructure. All samples show a similar size distribution of grains, averaging 20 μm in size. The AR and LN microstructures exhibit a large quantity of coherent boundaries, while the CR structure shows substantial deformation along similar pre-coherent interfaces. In higher magnifications, one actually sees these deformed interfaces resolve into a network of coherent twinning structures. For the FeNi-CR sample, there is near 100%

coverage of the surface with such structures, and EDS measurements, not shown, could not find compositional heterogeneity between them. Their exact structure is to be determined. All samples possessed varying degrees of these structures, all 100 nm in size, but accurate estimates for the volume fraction are difficult due to the inability to resolve them at lower magnifications. In the LN sample, the structures however seem much less apparent throughout the bulk than the AR sample, meaning the quench may have suppressed their formation.

The data obtained so far on these FeNi alloys seem at odds with one another. Plastic strain seems to have increased the amount of nanoscopic twinning structures in the FeNi-CR sample, as predicted by Rao [58], but this increase in supposed premartensite seems not to have affected either thermal expansion or magnetization behavior significantly. It did, however, increase the magnetostriction, implying there must be, to some extent, an increase in magnetoelastic coupling. In comparison, the FeNi-LN sample appeared to have less amounts of these structures, which imparted invar like behavior in the thermal expansion, yet neither the magnetostriction nor magnetization seemed too affected compared to the AR sample. As seen in the SEM, however, the martensite developed in these FeNi alloys is significantly larger in size than those structures observed in either FePd or FeGa, which attests to the drastic effect reduction in size of the martensites imparts on the overall magnetostriction.

A large missing piece in these studies of FeNi so far is crystallographic data as a function of temperature within the range of the thermal expansion and magnetostriction measurements. The nanoscopic nature of these martensites requires high resolution XRD equipment or TEM capable of detecting their presence distinct

from the cubic parent, a phenomenon responsible for streaking of diffraction spots in TEM for these premartensitic materials [12, 22].

Appendix E: Measurement and Analyses Details

E.1 Sample Preparation

Three FeGa alloys studied were ordered from Ames Laboratory in Iowa State University. Crystals were prepared of composition 18, 19, and 22 at. % Ga from arc melting of 99.999% pure Fe and 99.99% pure Ga sources. The crystals were grown using the Bridgman technique, and single crystals were ordered only for the 18 and 22 % Ga alloys with a [100] normal. The crystallinity was confirmed at Ames through Laue back-scattering. Each alloy was prepared as a rod 5-7 cm in length with a diameter of 8 mm. All of the alloys were subject to a heat treatment of 1273 K in inert atmosphere for 3 days for homogenization followed by an ice-quench to room temperature. The 26 at. % Ga alloy came from AJA International in Massachusetts, prepared by hot pressing pellets of 99.99 % pure Fe and 99.9 % pure Ga into a target. Disks of each alloy were cut 0.5-1 mm thickness using electro-discharge machining (EDM) in a programmable wire-cutting machine, using a wire of 0.5 mm diameter. Compositions were confirmed through wavelength dependent spectrometry carried out with the JAX 8900R Microprobe in the AIM lab at the University of Maryland. Disks cut from the top and bottom of the 18 % single crystal rod revealed that the rod itself possessed a composition gradient, yielding

samples 17 and 18 at. % from the same rod.

A polycrystalline FeNi alloy of 35.6 at. % Ni also came ordered from Ames Laboratory, prepared in a similar procedure. The rod was machined into a 1.5 mm thick sheet and sent to us as a 1.5 in.^{2} cut-out, but the exact process was not revealed to us. A number of disks of 3, 5 , and 10 mm diameters were cut using the same EDM procedure as for the FeGa alloys. Some of these disks were subject to a liquid-N_2 quench from room temperature by immersion in a Dewar flask followed by subsequently allowing for them to again reach room temperature. Remnants of the FeNi sheet were cold-rolled to a 50 % reduction in thickness after several iterations through a mechanical roller. A further number of disks 3, 5, and 10 mm in diameter were cut from the cold-rolled sheet.

The $Fe_{68.8}Pd_{31.2}$ single crystal was prepared by Takashi Fukuda of Osaka University, who used a high purity Fe rod (99.999%) and a Pd sheet (99.9%) source elements. The ingot was first prepared via arc melting, and a [100] single crystal was grown using the floating zone method The crystalline orientation was determined by a back-reflection Laue method. The alloy was heat treated at 1373K for 24h followed by quenching into ice water. Disks of 5mm diameter and 1mm thickness were cut via EDM with both [100] and [110] normals.

Microscope specimens were each prepared first through mounting the disks in epoxy, followed by mechanical polishing down to a 0.3 μm finish using an alumina-powder colloid. The $Fe_{64.4}Ni_{35.6}$ samples examined in SEM underwent three successive 20 s applications of aqua regia for etching. TEM samples of the FeGa alloys were created using focused ion-beam microscopes (FIB). Rough machining was per-

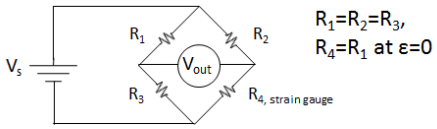

Figure E.1: The circuit configuration of a Wheatstone Bridge to measure strain.

formed in the XEIA-FIB in the AIM lab facilities to create a 20 x 5 μm sized lamella roughly 2 μm thick. A $\sim$1 μm thick platinum coating was deposited on each sample for support and protection during this procedure. Samples were then transferred to the GAIA-FIB in the AIM lab, where samples were glued with tungsten deposition onto a fine-tipped probe, after which the lamella were liberated from the bulk alloy via milling. The lamella was transferred from the probe to Cu support grids, glued to the side of the supports with tungsten, followed by subsequent milling to remove their attachment to the probe. Fine polishing of these mounted lamella was carried out with iterative milling of the samples with small currents (40-80 pA) of the ion beam. These iterations were performed until the protective Pt layer had been completely destroyed, and the sample revealed itself to have extremely thin electron transparent areas revealed through SEM micrographs taken in the GAIA-FIB.

E.2 Strain Measurements: Thermal Expansion and Magnetostriction

All strain measurements came from measuring the voltage drop across a Wheatstone Bridge circuit. The Wheatstone Bridge is depicted in figure E.1, and it involves a connection of a voltage source to two equivalent resistors connected in parallel with a another equivalent resistor and an unknown, with a voltage probe connected across the parallel 'bridge.' The unknown resistance comes from a strain gauge designed

to have the same resistance at zero strain, and, when attached to a sample, any change in length causes a proportional change in resistance which is detected by the voltage across the bridge. The measurements were taken using a PXIe-4330 data acquisition (DAQ) card interfaced with an NI PXIe-1073 Chassis, and we connected this to WK-06-030WT-120 specification strain gauges from Vishay Precision Group, mounted to samples with M-Bond 200 epoxy. When possible, gauges were adhered along specific crystalline orientations determined by rotating samples in a saturated magnetic field to identify easy magnetic axes.

The temperature was controlled using Laird Technologies multi-stage Peltier device with PID control outputted by a Keithley 2200 Power Supply and programmed through LabVIEW software. Temperature itself was monitored using T-type thermocouples from Omega, interfaced to the computer with a TC01-USB adapter possessing internal calibrations. To improve performance of the device, a stainless steel apparatus was constructed to fit between the poles of the electromagnet contained in our lab. The Peltier device rested atop a custom-machined CuBe flange, which had teflon flanges secured above and below to improve thermal insulation. The apparatus was sealed by inserting a glass dome into the top teflon flange. A Cu tube fitting was silver-brazed around the outside of the CuBe flange, and hosing was attached to water cool the flange and the Peltier device to prevent overheating and strong thermal drift. The hosing had an additional fitting to a secondary LC-200 Peltier device from TE Technology Inc., and this reduced the base temperature of the Laird Peltier device to make lower temperatures attainable for measurements. The stainless steel apparatus possessed a fitting on the back to

attach to a mechanical floor pump to evacuate the measurement chamber to prevent condensation. When running the vacuum and water cooling, the stage could reach temperatures of 233 to 378 K (-40 to 105 $^{\circ}C$) and maintain a fidelity of $\pm$ 0.1 K to the set temperature.

The magnetic field of the electromagnet was controlled using a second Keithley 2200 Power Supply connected directly to the power supply of the magnet. Field calibrations with respect to the output voltage of the power supply were carried out using a Model 455 Gaussmeter from Lake Shore Cryotronics, Inc. LabVIEW programs were developed using these calibrations to develop set-point as well as magnetic cycling protocols.

With tight control of both temperature and magnetic field, LabVIEW programs were created to carry out three types of measurements: (1) thermal expansion, (2) magnetostriction, and (3) magnetostriction at different temperatures. These programs outputted measurement files containing temperature, magnetic field, and strain data directly. These files would contain up to 10,000 individual data points, and macros were created through Microsoft Excel to condense the data by averaging measurements rounded to either specified temperature or field targets. To assess the expansion and magnetostriction of the strain gauges/epoxy, measurements on a Ti-silicate bar possessing near zero thermal expansion and zero magnetostriction were carried out and subtracted from measurements on the Fe-alloys to improve the accuracy.

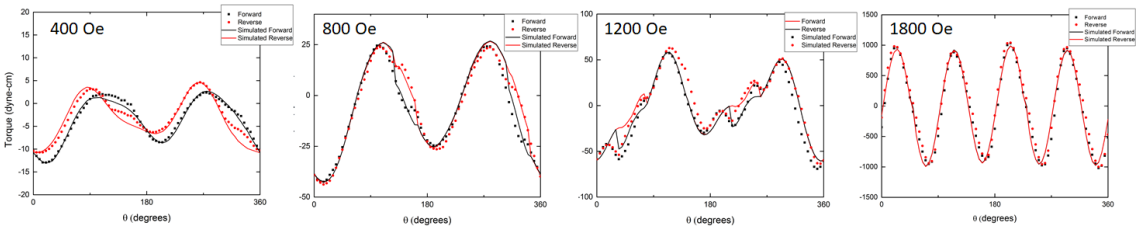

Figure E.2: Magnetic torque measurements along with simulated fits to the experimental data taken on $Fe_{82}Ga_{18}$ at applied fields of 400, 800, 1200, and 1800 Oe.

E.3 Magnetization and Magnetic Torque

All magnetization measurements were carried out using a Lake Shore Cryotronics 7400 Series Vibrating Sample Magnetometer (VSM). Without going into finer detail, a VSM measures sample magnetization through the principles of Lenz's Law. Pick-up coils of a known geometry are attached to the poles of an electromagnet while the measured sample is kept suspended between the poles and mounted to a rod driven into rapid oscillation by piezoelectrics in a vibrating head. When a field is applied, the rapid vibration of the sample causes an AC induced electromotive force in the pick coils due to the moving magnetic flux. The magnitude of this induced voltage is linearly proportional to the magnetization of the sample. Nearly all magnetization measurements were carried out through a magnetic field cycle of 1 T to -1 T back to 1 T. The magnetization versus temperature measurements carried out on FeNi samples were completed using a 74034 High Temperature Oven attachment and PID control through a 741-VTA Instrument, both produced by Lake Shore Cryotronics for use with their instrument.

Magnetic torque measurements were completed at Morgan State University

with the help of Dr. Abdellah Lisfi and his student Sabin Pokharel. They developed a custom-stage capable of holding rotating samples in the middle of an electromagnet. Their instrumentation includes a calibrated spring force sensor to measure the force the sample exerts when rotated a specified angle away from its easy axes. They helped perform measurements with and without the use of a cryostat to measure the magnetic torque at different temperatures in addition to different fields.

Figure E.2 shows the evolution of magnetic torque in the $Fe_{82}Ga_{18}$ sample which exhibited hysteretic switching behavior due to the presence of a uniaxial anisotropy component. The torque initially has a hysteretic 2-fold symmetry, and the switching changes phase abruptly when a 4-fold symmetry starts to manifest at higher fields before ultimately dominating the overall signal. In order to extract anisotropy information corresponding to the uniaxial and 4-fold component, the data has to be simulated and fitted with an appropriate model. Unlike FePd, which had a 2-fold symmetry component possessing substantially lower anisotropy, FeGa could not be easily modelled with a $A\sin(2\theta)+B\sin(4\theta)$ function. For materials with high enough uniaxial anisotropy, there are certain angles along the hard axis that the Zeeman energy from the external field must overcome, and for weak applied fields, it may be impossible to magnetize the sample along these angles [44]. Over these rotation angles, the magnetization becomes pinned and the torque stagnates until such rotation occurs that the magnetization spontaneously switches to the opposite direction. The anisotropy energy for this process has to be described then in terms of both the applied field angle θ and the material's actual angle of magnetization

relative to the easy axis, ψ, resulting in the expression

$$u_a = K_u \sin^2(\psi) - HM_s \cos(\theta - \psi) \tag{E.1}$$

where the first term represents the uniaxial anisotropy with constant K_u, and the second term represents the Zeeman energy for a material with magnetization $M_s \cos(\theta - \psi)$ under applied field H. To determine the magnetization angle and ultimately the torque a uniaxial material exhibits for an applied field angle θ, the energy must be minimized:

$$\frac{\partial u_a}{\partial \psi} = 0 = 2K_u \sin(\psi)\cos(\psi) - HM_s \sin(\theta - \psi) \tag{E.2}$$

$$K_u \sin(2\psi) = HM_s \sin(\theta - \psi) \tag{E.3}$$

The relation defined in E.3 represent the solutions for ψ in terms of θ, but the relation itself is non-linear and cannot be solved analytically. To determine $\psi_0(\theta)$, numerical methods must be used, and this was achieved by creating scripts in MATLAB which generated expressions of u_a as a function of both ψ and θ from 0 to 2π and sifting through the resulting energy surface to identify local minima of ψ at constant θ. For each value of θ, there exists either one or two equilibrium magnetization angles, ψ that correspond to local energy minima, and an additional script was developed to properly index two solution functions as a results $\psi_{0,1}(\theta)$ and $\psi_{0,2}(\theta)$ which physically represent how the uniaxial component rotating the material clock-wise (increasing θ) or counter-clockwise (decreasing θ), respectively.

The total anisotropy was then modelled as a superposition of the 4-fold symmetry, the shape anisotropy, and the uniaxial anisotropy. Each data set contained clockwise and counter-clockwise measurements, which are labelled as forward and reverse in Fig. E.2. The expressions for modelling this data are

$$L_1(\theta) = K_1 \sin(4\theta) + K_u \sin(2\psi_{0,1}(\theta - \theta_u) + NM^2 \sin(2(\theta - \theta_d)) \tag{E.4}$$

$$L_2(\theta) = K_1 \sin(4\theta) + K_u \sin(2\psi_{0,2}(\theta - \theta_u) + NM^2 \sin(2(\theta - \theta_d)) \tag{E.5}$$

where L_1 and L_2 are the overall torques for the two solutions, K_1 is the 4-fold anisotropy constant, NM^2 is the shape anisotropy which grows quadratically in proportion to the magnetization, and θ_u and θ_d are phase shifts which adjust the placement of the uniaxial and shape anisotropy curves with respect to the 4-fold component. These expressions are intrinsic by nature, but the data taken on $Fe_{82}Ga_{18}$ was extrinsic, which meant that the amplitude of the 4-fold and uniaxial components had been recorded in proportion to the volume of material responsible for each respective signal. Without knowing the phase fraction for the two components within the material, it is not possible to convert the extrinsic experimental data to intrinsic values without additional assumptions. The modelling itself then, in some sense, captures the volume-modified results of the intrinsic model, and it is more accurate to state the model followed the expressions

$$L_1(\theta) = N_c \sin(4\theta) + N_u \sin(2\psi_{0,1}(\theta - \theta_u) + N_d \sin(2(\theta - \theta_d)) \tag{E.6}$$

$$L_2(\theta) = N_c \sin(4\theta) + N_u \sin(2\psi_{0,2}(\theta - \theta_u) + N_d \sin(2(\theta - \theta_d)) \tag{E.7}$$

where N_c, N_u, and N_d have replaced the intrinsic proportionality constants and simply correspond to the relative amplitude of the different components.

It also became clear throughout the simulation process that these expressions lacked the ability to capture the hysteretic switching regions perfectly when the 4-fold fold anisotropy began to take larger values. For instance, in the 1200 Oe torque measurement shown in Fig. E.2, the switching area has a non-uniform shape, possessing convex curvature in the forward direction and concave curvature in the reverse. The data itself suggested that the 4-fold anisotropy in these regions exponentially decays to near zero, causing the uniaxial anisotropy to strongly manifest rather than simply superposing on top of a regular $\sin(4\theta)$ curve. The physical reasons for this are not exactly clear, but careful analysis of the simulation showed that the phase difference θ_u often caused the hysteretic switching to occur at angles where the cubic anisotropy passed through 0. In other words, the uniaxial component's hard axis lay along the cubic 4-fold component's easy axis, meaning the 4-fold anisotropy in this region is at an energy minimum, since magnetic torque is the derivative of the anisotropy with respect to angle. With this in mind, the model was modified to exponentially decay to 0 in the first half of the switching region and then to exponentially grow from 0 in the second half. Physically, this implies that the pinning of the uniaxial component also affects the magnetization angle of the 4-fold component, keeping the 4-fold magnetization angle confined to near 0 anisotropy during the switching process. Thus, the complete model used to simulate these curves involved breaking the data into piece-wise functions, with critical switching angles, $\theta_{1,s}$, $\theta_{1,f}$, $\theta_{2,s}$, and $\theta_{2,f}$, defining the respective pieces, with the

subscripts 1 referring to the first switching region, 2 referring to the second switch region, s referring to the starting angle of switching, and f referring to the final angle of switching. For brevity, only the forward model is expressed:

$$L_1(\theta) = \begin{cases} N_c \sin(4\theta) + N_u \sin(2\psi_{0,1}(\theta - \theta_u) + N_d \sin(2(\theta - \theta_d)), & \text{for } [0, \theta_{1,s}] \\ N_c e^{\frac{2\psi_{0,1}(\theta) - (\theta_{1,s} + \theta_{1,f})}{2C}} \sin(4\theta) + N_u \sin(2\psi_{0,1}(\theta - \theta_u) + N_d \sin(2(\theta - \theta_d)), & \text{for } [\theta_{1,s}, \theta_{1,f}] \\ N_c \sin(4\theta) + N_u \sin(2\psi_{0,1}(\theta - \theta_u) + N_d \sin(2(\theta - \theta_d)), & \text{for } [\theta_{1,f}, \theta_{2,s}] \\ N_c e^{\frac{2\psi_{0,1}(\theta) - (\theta_{2,s} + \theta_{2,f})}{2C}} \sin(4\theta) + N_u \sin(2\psi_{0,1}(\theta - \theta_u) + N_d \sin(2(\theta - \theta_d)), & \text{for } [\theta_{2,s}, \theta_{2,f}] \\ N_c \sin(4\theta) + N_u \sin(2\psi_{0,1}(\theta - \theta_u) + N_d \sin(2(\theta - \theta_d)), & \text{for } [\theta_{2,f}, 2\pi] \end{cases} \tag{E.8}$$

where C was introduced as a decay constant to improve the fit to the data.

The numerical simulation needed to evaluate the complex torque express of eq. E.8 made it difficult to create scripts which automatically generated the best fit for a given set of experimental data, and, as such, most of the simulations were evaluated manually with scripts plotting numerous iterations of eq. E.8 for comparison with the data. Overall, the model effectively could reproduce the torque curves, and the parameters extracted from the fit presented in Fig. 4.7 demonstrate the interesting characteristics of these torque curves as a function of field.

E.4 Hall Probe Measurements in the TEM

The Hall Effect refers to the creation of a transverse electric field, $\mathbf{E}_H$, when a material carrying a current density $\mathbf{J}$ is placed in a perpendicular applied magnetic

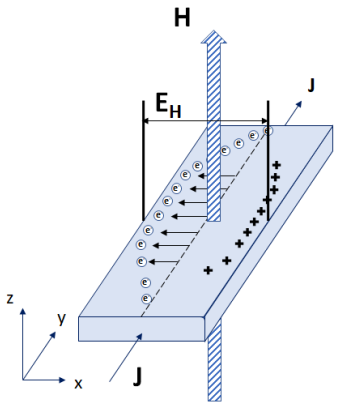

Figure E.3: A schematic representation for the Hall Effect in materials.

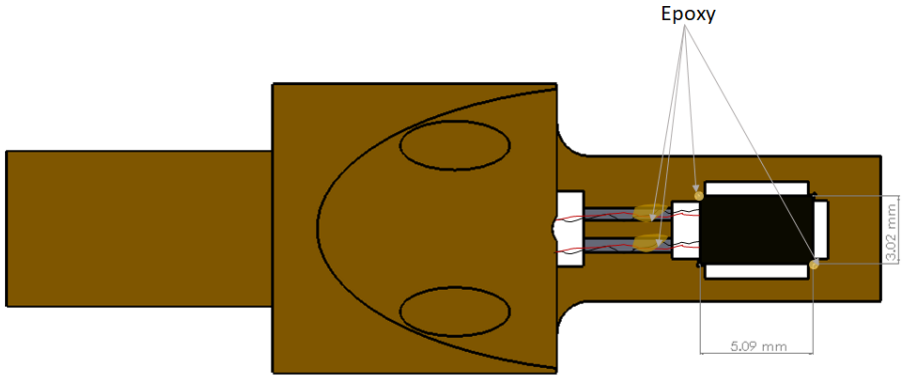

Figure E.4: The design of the nose piece to hold the Hall Probe for insertion into the TEM.

field **H**. This occurs due to the Lorentz force of travelling electrons (or holes) in the conducting material, $F = \mu_0 q(\mathbf{v} \times \mathbf{H})$, deflecting them transverse to the current carrying direction. A schematic of the effect is shown in Figure E.3. The voltage generated is ideally linearly proportional to the applied field moderated by a so-called Hall coefficient, R_H, which depends on the mobility and density of charge carriers of the material. It is generally higher for semiconductors, which possess high mobility but lower conductivity than metals, preventing a short circuiting of the effect [16].

An AS-NTP Transverse Hall Probe was obtained from Projekt Elektronik, calibrated to sense fields up to 2 T with a sensitivity of approximately 0.1 mT in this range. The probe itself has dimension of 5 x 3 x 0.9 mm, and a custom nose piece for the TEM was machined to support the probe and facilitate its insertion into the JEOL 2100 LaB_6 and JEOL 2100 FEG TEMs in the AIMLab facilities at the university. A schematic of this nose piece is shown in Figure E.4. The probe itself was laid within a hole designed to oversize the probe by about 0.1 mm and glued into place with a minimal amount of epoxy so as to minimize any possible stress on the probe. Since the probe itself is a brittle semiconductor, minimal stress is crucial to prevent any influence on the conductive properties or possible fracture. After successively gluing the probe, its wires were fed through the nose piece and secured into a specialized TEM rod with vacuum feedthroughs for the electronics.

The objective lens (OL) within a TEM column controls the strength of the magnetic field used to focus electrons into a collimated beam, and the current passing through the coils in the lens can be controlled in "Fren Lens Control" mode using the software installed to operate the instrument. There are two main options to adjust this voltage, subdivided into a 'coarse' and 'fine' control, differentiated by the magnitude in which the lens voltage is increased by an equivalent increase in output of the function. To use a quantitative example, adjusting the Free Lens Control value of the coarse OL from a hexadecimal code of 1000 to 2000 adjusts V_{OL} from 0.62 to 0.94 V whereas the equivalent adjustment in fine OL changes V_{OL} from 0.01 to 0.03 V. These voltages are nominal in nature and do not reflect the true voltage drops over the OL lens, as standardized practices in software design for TEM

instruments keeps these adjustments to span a range of 0 to 5 V across different lens designs, whereas different lenses require additional resistors and transformers to generate the proper current output to sustain the high fields needed to focus the electron beam [87]. For instance, the JEOL 2100 FEG TEM can sustain a maximum current of 13.4053 A, and possesses 5.8 Ω, meaning the 5 V output reported by the software at this current in reality corresponds to an actual voltage of 77.75 V across the lens. However, the reported software voltages are useful to measure the magnetic field against since they can be directly controlled with the software. Obtaining actual voltage readings across the lens would prove a more difficult effort that would require extra calibrations between the software readings and real voltages at any rate.

Measurements taken for the magnetic field using coarse and fine OL adjustment for both the LaB_6 and FEG TEMs are shown in Figure E.5. The figure makes clear that the FEG TEM is capable of operating at a much higher field, which is to be expected owing to the instrument's superior resolution limits over the LaB_6 TEM, but this unfortunately means the voltage range from 2.16 to 5 V cannot be measured currently by the Hall Probe without adapting its electronics to interface with a lock-in amplifier to obtain accurate results outside the specifications manufactured by Projekt Elektronik. Current efforts are underway to carry out such measurements. The current sensor cannot detect fields above 2.5 T, and it is even possible that the values from 2.0-.5 T possess unaccounted for errors due to non-linear deviations of the current sensor calibration. These results also suggest that the LaB_6 may be more suitable for studying low field magnetic behavior in Lorentz microscopy because it can achieve tighter control of low field values due to

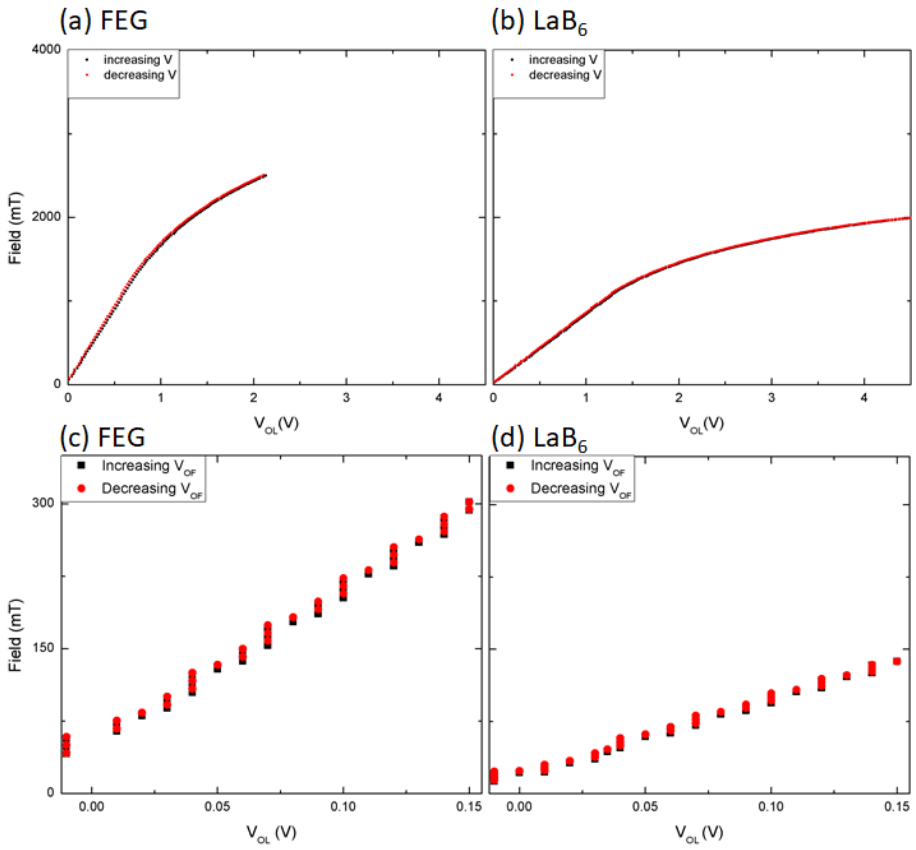

Figure E.5: Magnetic field data as a function of objective lens voltage for the JEOL 2100 FEG and JEOL 2100 LaB_6 TEMS using coarse, **(a) (b)**, and fine, **(c) (d)**, control.

its reduced sensitivity to the OL voltage.

The STEM analysis conducted on the FeGa samples spanned a V_{OL} range of 1.92 to 4.56 V, meaning the Hall Probe could not obtain field data the upper end of voltages used in the *in situ* structural studies. To extend the measurement capabilities of the Hall Probe, custom wires were created to acquire readings of the Hall voltage using an SR830 Lock-In Amplifier. A 500 kΩ resistor was introduced to lower the current across the Hall Bar from a 2.5 V, 100 kHz AC signal of the lock-in. A second measurement was taken in the FEG TEM for taking simultaneous probe sensor and lock-in voltage readings as a function of V_{OL}, and an interpolation

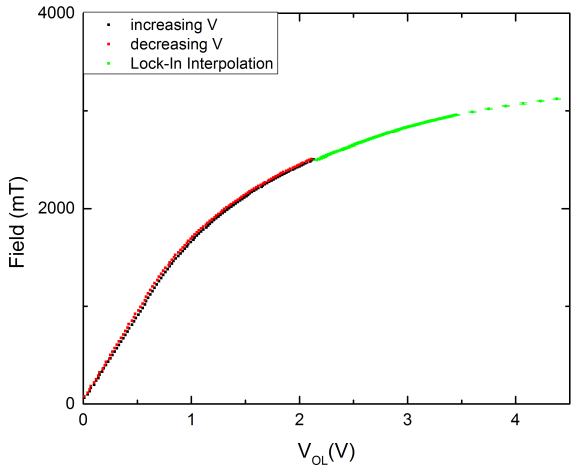

Figure E.6: Magnetic field data as a function of objective lens voltage for the JEOL 2100 FEG with a calibrated interpolation of Lock-In Amplifier measurements shown for voltages which generated a field outside the sensitivity range of the Hall Probe sensor.

of the calibration between the two readings was done to estimate the field for V_{OL} values which exceeded the probe sensor's capabilities.The interpolation from which field values are reported in the body of the thesis is shown in Figure E.6.

E.5 TEM Measurements and STEM analysis

The use of TEM makes possible an enormous amount of material analysis at the nanoscale, including diffraction, chemical mapping, defect analysis, and, perhaps most importantly, high resolution imaging of atomic columns and even individual atoms in special cases. Employing such techniques requires an intimate understanding of the physical interactions between electrons and material solids, and much of these measurements involve detecting different angular regions of scattering experienced by electrons passing through solid materials and correct interpretation of the mechanisms responsible for such scattering. Transmission Electron Microscopy, by

Williams and Carter, is a comprehensive textbook which covers the various science made possible through the use of TEM and should be referred to for more in depth explanation of the physics and materials science covered in this section [45].

The majority of TEM analysis covered in this thesis focuses on diffraction, or coherent scattering of electrons along the transmitted beam into strong intensity reflections which relate to the structure of the atomic lattices through which the electrons pass. In great simplification, the sample in the TEM acts as a diffraction grating with slits created by the periodic spacing of atoms in a crystal lattice, and diffraction patterns can be obtained over areas of a TEM sample by placing an aperture through the back focal plane of the objective lens and adjusting the lens currents to bring the pattern into focus on the image plane. Such selected area diffraction (SAD) has advantages over bulk diffraction probes such as X-ray or neutron diffraction, since localized diffraction patterns can be obtained over extremely small areas, allowing one to distinguish distinct crystalline phases at the nanoscale by focusing the aperture onto areas corresponding to those phases. Even amongst differently oriented grains, SAD can allow one to characterize differently oriented grains, and high resolution imaging can allow one to study interfaces and boundaries between crystallites. The introduction of a second aperture, often called a High Contrast aperture, can allow a user to focus specifically on a single diffraction spot and highlight areas of a sample which contribute to the scattering of this specific diffraction peak. It's possible to tilt a sample in a TEM to enhance the brightness of just a single peak and the transmitted beam to minimize interference of other scattering, such as effects of double diffraction, and this technique, called the Two-

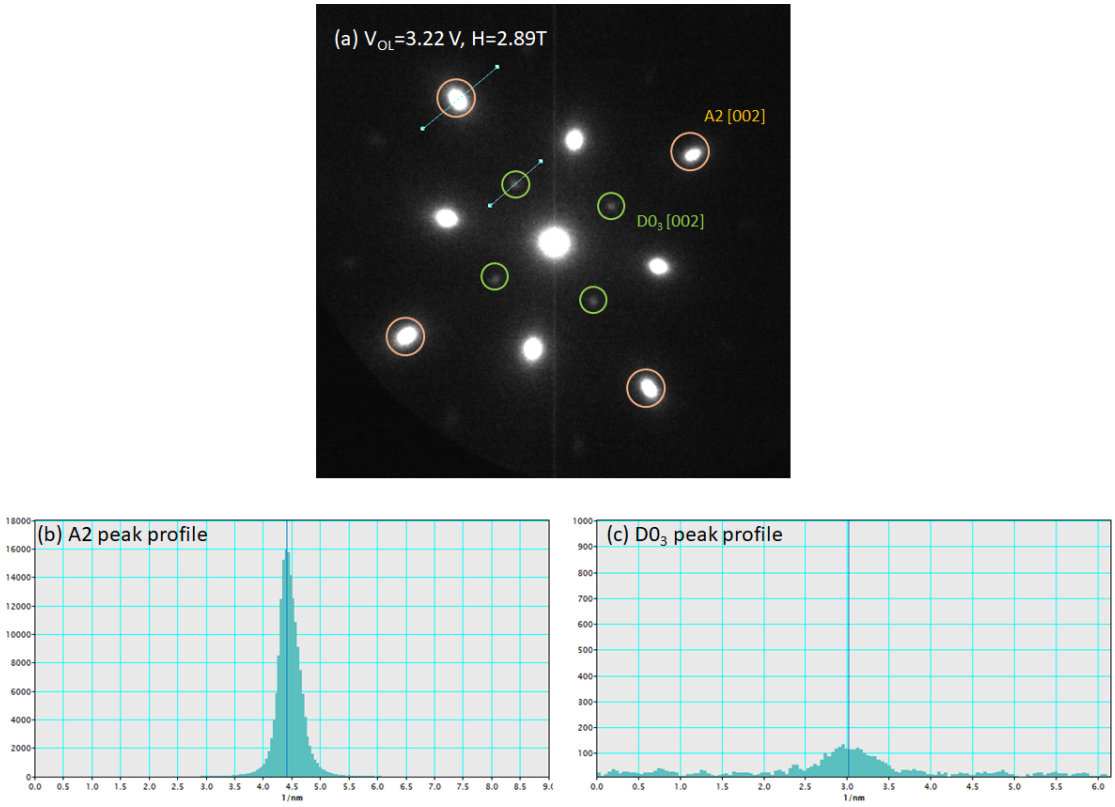

Figure E.7: **(a)** A NED diffraction pattern of $Fe_{78}Ga_{22}$ taken at an objective lens voltage of 3.22 V, with corresponding peak profiles for **(b)** the A2 phase and **(c)** the $D0_3$ phase.

Beam Condition, allows one to obtain dark field images. Such images allow for clear contrast differences to highlight the presence of different crystal structures as well as defects such as dislocation and stacking faults within a material. For instance, the dark field images reported on FeGa in the body of this thesis highlighted the lack of dislocations in supposed single crystal alloys and instead revealed a large amount of nanocrystalline precipitates dispersed throughout the bulk of these alloys (Figs. 4.9 and 4.10).

Scanning transmission electron microscopy (STEM) involves condensing the electron beam into a coherent, focused probe less than 1 nm in size, which allows one to surpass the localized probe of SAD, which has a smallest probe size of roughly

150 nm. This makes it possible to obtain nanoelectron diffraction patterns (NED) which correspond to the local structure of individual nano-sized grains, and the electron beam in STEM has tightly controlled placement through the use of specialized scanning coils which induce magnetic fields to deflect the beam to a desired position. This technique become necessary to attempt to identify the structure of the nanocrystalline precipitates observed through dark field imaging and high resolution imaging of the FeGa alloys. Because images in the TEM are always obtained from scattered electrons, one must understand that focused images are essentially formulated through the magnification of diffracted electrons onto the image plane. The TEM always detects both real space and diffracted information simultaneously, and depending on the focus, one can switch from one set of information to the other. This is the principle through which NED works. Free Lens Control in the TEM allows one to modify the strength of the condenser lens which affects the focus of the scanning beam and bring sharp diffraction peaks into focus while in scanning mode [46–48, 88]. The *in situ* STEM analysis involved acquiring NED patterns at different objective lens voltages, which in turn affects the strength of the focusing magnetic field in the instrument. In optical terms, adjusting the objective lens voltage changes the focal length of the lens itself, and NED patterns can be brought back into focus by compensating with adjustments to the strength of the condenser lens [49].

The analysis of these NED patterns focuses on the intensity of diffraction peaks corresponding to an ordered BCC $D0_3$ crystal compared to the peaks of disordered BCC A2. In FeGa, the lattice difference between these two crystals is about 0.2

% [29]. Allowed reflections in disordered BCC correspond to crystal directions with Miller indices h, k, and l such that $h+k+l$ =an even number. In $D0_3$, the ordering of Ga atoms allows for more reflections due to the difference in structure factor between Fe and Ga. Even odd summations of h, k, and l give rise to weak reflections for this structure, which allows one to distinguish $D0_3$ from A2. An example [100] zone axis NED pattern for $Fe_{78}Ga_{22}$ is shown in Figure E.7, along with intensity profiles for an A2 and $D0_3$ peak in E.7b and E.7c. The analysis of these peaks focused on recording the maximum intensity of the peaks for the respective phases as well as the noise level surrounding the peaks. For each NED pattern, 4 intensities for the A2 structure, 4 for the $D0_3$ structure, and 8 intensities for the noise were recorded. An average was taken for each of these intensity groups as well as a standard of deviation. The calculation of the $D0_3$ intensity used the expression

$$\%_{D0_3} = \frac{(D0_{3,average} - n_{average})}{(D0_{3,average} - n_{average}) + (A2_{average} - n_{average})} * 100 \tag{E.9}$$

where n represents the noise intensity. Error estimates were obtained in quadrature, and this method of error estimation has the generic form

$$\Delta f(x, y, ...) = \sqrt{\left(\Delta x \frac{\partial f}{\partial x}\right)^2 + \left(\Delta y \frac{\partial f}{\partial y}\right)^2 + \ldots} \tag{E.10}$$

First this was done for the error of intensity for each respective phase, such that

$$\Delta x = \sqrt{D0_{3,STD}^2 + n_{STD}^2} \tag{E.11}$$

$$\Delta y = \sqrt{A2_{STD}^2 + n_{STD}^2} \tag{E.12}$$

If one simplifies eq. E.9 such that $x = D0_{3,average} - n_{average}$ and $y = A2_{average} - n_{average}$, then one determines the error expression for $\%D0_3$ as

$$\Delta\%_{D0_3} = 100\sqrt{\left(\frac{\Delta x * y}{(x+y)^2}\right)^2 + \left(\frac{\Delta y}{(x+y)^2}\right)^2} \tag{E.13}$$

Bibliography

[1] A.E. Clark, J.B. Restorff, M. Wun-Fogle, T.A. Lograsso, and D.L. Schlagel. Magnetostrictive properties of body-centered cubic fe-ga and fe-ga-al alloys. *IEEE Trans. Magn.*, 36(5):3238–3240, Sep 2000.

[2] Nasir Rahman, Junming Gou, Xiaolian Liu, Tianyu Ma, and Mi Yan. Enhanced magnetostriction of fe81ga19 by approaching an instable phase boundary. *Scripta Materialia*, 146:200 – 203, 2018.

[3] A. E. Clark and H. S. Belson. Giant room-temperature magnetostrictions in tbfe2 and dyfe2. *Phys. Rev. B*, 5:3642–3644, May 1972.

[4] A.E. Clark. Chapter 7 magnetostrictive rare earth-fe2 compounds. volume 1 of *Handbook of Ferromagnetic Materials*, pages 531 – 589. Elsevier, 1980.

[5] Mark B. Moffett, Arthur E. Clark, Marilyn Wun-Fogle, Jan Linberg, Joseph P. Teter, and Elizabeth A. McLaughlin. Characterization of terfenol-d for magnetostrictive transducers. *The Journal of the Acoustical Society of America*, 89(3):1448–1455, 1991.

[6] Frederick T. Calkins, Alison B. Flatau, and Marcelo J. Dapino. Overview of magnetostrictive sensor technology. *Journal of Intelligent Material Systems and Structures*, 18(10):1057–1066, 2007.

[7] P. J. Webster, K. R. A. Ziebeck, S. L. Town, and M. S. Peak. Magnetic order and phase transformation in ni2mnga. *Philosophical Magazine Part B*, 49(3):295–310, 1984.

[8] K. Ullakko, J. K. Huang, C. Kantner, R. C. OHandley, and V. V. Kokorin. Large magnetic field-induced strains in ni2mnga single crystals. *Appl. Phys. Lett.*, 69(13):1966–1968, 1996.

[9] Julia R. Downing, Suok-Min Na, and Alison B. Flatau. Compressive pre-stress effects on magnetostrictive behaviors of highly textured galfenol and alfenol thin sheets. *AIP Advances*, 7(5):056420, 2017.

[10] M. Matsui, T. Shimizu, H. Yamada, and K. Adachi. Magnetic properties and thermal expansion of fe-pd invar alloys. *Journal of Magnetism and Magnetic Materials*, 15:1201 – 1202, 1980.

[11] Masaaki Sugiyama, Ryuichiro Oshima, and Francisco Eiichi Fujita. Mechanism of fcc-fct thermoelastic martensite transformation in fe-pd alloys. *Trans. Jap. Inst. Met.*, 27(10):719–730, 1986.

[12] Hideki Seto, Yukio Noda, and Yasusada Yamada. Precursor phenomena at martensitic phase transition in fe-pd alloy. i. two-tetragonal-mixed phase and crest-riding-periodon. *J. Phys. Soc. Jap.*, 59(3):965–977, 1990.

[13] A. G. Khachaturyan, S. M. Shapiro, and S. Semenovskaya. Adaptive phase formation in martensitic transformation. *Phys. Rev. B*, 43:10832–10843, May 1991.

[14] J.P. Joule Esq. Xvii. on the effects of magnetism upon the dimensions of iron and steel bars. *The London, Edinburgh, and Dublin Philosophical Magazine and Journal of Science*, 30(199):76–87, 1847.

[15] Nel, Louis. Anisotropie magntique superficielle et surstructures d'orientation. *J. Phys. Radium*, 15(4):225–239, 1954.

[16] Robert C. O'Handley. *Modern magnetic materials: principles and applications*. John Wiley and Sons, 2000.

[17] M Sato, B H Grier, S M Shapiro, and H Miyajima. Effect of magnetic ordering on the lattice dynamics of fcc fe 1-x pd x. *Journal of Physics F: Metal Physics*, 12(10):2117, 1982.

[18] M. Mitsuka, T. Ohba, T. Fukuda, T. Kakeshita, and M. Tanaka. Martensitic transformation in fepd alloy revealed by synchrotron radiation. *Mat. Sci. Eng. A*, 438–440:332–335, 2006. Proceedings of the International Conference on Martensitic Transformations.

[19] A. E. Clark, K. B. Hathaway, M. Wun-Fogle, J. B. Restorff, T. A. Lograsso, V. M. Keppens, G. Petculescu, and R. A. Taylor. Extraordinary magnetoelasticity and lattice softening in bcc fe-ga alloys. *J. Appl. Phys.*, 93(10):8621–8623, 2003.

[20] Sadia Rafique, James R. Cullen, Manfred Wuttig, and Jun Cui. Magnetic anisotropy of fega alloys. *Journal of Applied Physics*, 95(11):6939–6941, 2004.

[21] Jayasimha Atulasimha, Alison B Flatau, and James R Cullen. Analysis of the effect of gallium content on the magnetomechanical behavior of single-crystal fega alloys using an energy-based model. *Smart Materials and Structures*, 17(2):025027, 2008.

[22] Q. Xing, Y. Du, R.J. McQueeney, and T.A. Lograsso. Structural investigations of fega alloys: Phase relations and magnetostrictive behavior. *Acta Materialia*, 56(16):4536 – 4546, 2008.

[23] M. Laver, C. Mudivarthi, J. R. Cullen, A. B. Flatau, W.-C. Chen, S. M. Watson, and M. Wuttig. Magnetostriction and magnetic heterogeneities in iron-gallium. *Phys. Rev. Lett.*, 105:027202, Jul 2010.

[24] H. D. Chopra and M. Wuttig. Non-joulian magnetostriction. *nature*, 521:340, 2015.

[25] Yangkun He, J. M. D. Coey, Rudolf Schaefer, and Chengbao Jiang. Determination of bulk domain structure and magnetization processes in bcc ferromagnetic alloys: Analysis of magnetostriction in $Fe_{83}Ga_{17}$. *Phys. Rev. Materials*, 2:014412, Jan 2018.

[26] H. Cao, P. M. Gehring, C. P. Devreugd, J. A. Rodriguez-Rivera, J. Li, and D. Viehland. Role of nanoscale precipitates on the enhanced magnetostriction of heat-treated galfenol ($fe_{1-x}ga_x$) alloys. *Phys. Rev. Lett.*, 102:127201, Mar 2009.

[27] Mianliang Huang and Thomas A. Lograsso. Short range ordering in fege and fega single crystals. *Applied Physics Letters*, 95(17):171907, 2009.

[28] A.G. Khachaturyan and D. Viehland. Structurally heterogeneous model of extrinsic magnetostriction for fe-ga and similar magnetic alloys: Part i. decomposition and confined displacive transformation. *Metallurgical and Materials Transactions A*, 38(13):2308–2316, Sep 2007.

[29] I.S. Golovin, .M. Balagurov, V.V. Palacheva, I.A. Bobrikov, and V.B. Zlokazov. In situ neutron diffraction study of bulk phase transitions in fe-27ga alloys. *Materials & Design*, 98(Supplement C):113 – 119, 2016.

[30] Manfred Wuttig. personal transfer of data acquired for results published on by Rafique, Cullen, and Wuttig [20]., 2016.

[31] Manfred Wuttig, Liyang Dai, and James Cullen. Elasticity and magnetoelasticity of fega solid solutions. *Appl. Phys. Lett.*, 80(7):1135–1137, 2002.

[32] J. Cullen, P. Zhao, and M. Wuttig. Anisotropy of crystalline ferromagnets with defects. *Journal of Applied Physics*, 101(12):123922, 2007.

[33] Xiaolian Liu, Meixun Li, Junming Gou, Qiaochu Li, Yunhao Lu, Tianyu Ma, and Xiaobing Ren. Evidence for lattice softening of the fe-ga magnetostrictive alloy: Stress-induced local martensites. *Materials & Design*, 140(Supplement C):1 – 6, 2018.

[34] K Otsuka, C.M Wayman, K Nakai, H Sakamoto, and K Shimizu. Superelasticity effects and stress-induced martensitic transformations in cualni alloys. *Acta Metallurgica*, 24(3):207 – 226, 1976.

[35] Jake Steiner, Abdellah Lisfi, Tomoyuki Kakeshita, Takashi Fukuda, and Manfred Wuttig. Unique magnetostriction of fe68.8pd31.2 attributable to twinning. *Scientific Reports*, 6, 2016.

[36] M. Sato and Y. Ishii. Simple and approximate expressions of demagnetizing factors of uniformly magnetized rectangular rod and cylinder. *Journal of Applied Physics*, 66(2):983–985, 1989.

[37] R. C. OHandley. Model for strain and magnetization in magnetic shape-memory alloys. *Journal of Applied Physics*, 83(6):3263–3270, 1998.

[38] V. Z. C. Paes and D. H. Mosca. Magnetostrictive contribution to poisson ratio of galfenol. *Journal of Applied Physics*, 114(12):123915, 2013.

[39] Ganesh Raghunath and Alison B. Flatau. Study of magnetic domain evolution in an auxetic plane of galfenol using kerr microscopy. *Journal of Applied Physics*, 117(17):17E704, 2015.

[40] Suok-Min Na and Alison B. Flatau. Secondary recrystallization, crystallographic texture and magnetostriction in rolled fega based alloys. *Journal of Applied Physics*, 101(9):09N518, 2007.

[41] Suok-Min Na and Alison B. Flatau. Deformation behavior and magnetostriction of polycrystalline fegax (x=b,c,mn,mo,nb,nbc) alloys. *Journal of Applied Physics*, 103(7):07D304, 2008.

[42] S. Na, J. Yoo, and A. B. Flatau. Abnormal (110) grain growth and magnetostriction in lt;newline/ gt; recrystallized galfenol with dispersed niobium carbide. *IEEE Transactions on Magnetics*, 45(10):4132–4135, Oct 2009.

[43] A. Lisfi, C. M. Williams, L. T. Nguyen, J. C. Lodder, A. Coleman, H. Corcoran, A. Johnson, P. Chang, A. Kumar, and W. Morgan. Reorientation of magnetic anisotropy in epitaxial cobalt ferrite thin films. *Phys. Rev. B*, 76:054405, Aug 2007.

[44] A Lisfi, S Pokharel, W Morgan, G Warren, and M Wuttig. The power of torque magnetometry: defect induced switching in hexaferrite nano-structures. *Nanotechnology*, 25(41):415702, 2014.

[45] David B. Williams and C. Barry Carter. *Transmission Electron Microscopy: A Textbook for Materials Science*. Springer US, 2009.

[46] J. M. Cowley. Electron diffraction phenomena observed with a high resolution stem instrument. *Journal of electron microscopy technique*, 3:25–44, 1986.

[47] J.M. Cowley. Applications of electron nanodiffraction. *Micron*, 35(5):345 – 360, 2004.

[48] Kyou-Hyun Kim, Hui Xing, Jian-Min Zuo, Peng Zhang, and Haifeng Wang. Tem based high resolution and low-dose scanning electron nanodiffraction technique for nanostructure imaging and analysis. *Micron*, 71(Supplement C):39 – 45, 2015.

[49] Masahiro Kawasaki. personal communication, 2017.

[50] QingPing Sun, Ahadi Aslan, MingPeng Li, and MingXiang Chen. Effects of grain size on phase transition behavior of nanocrystalline shape memory alloys. *Science China Technological Sciences*, 57(4):671–679, Apr 2014.

[51] E L Principe, P Gnauck, and P Hoffrogge. A three beam approach to tem preparation using in-situ low voltage argon ion final milling in a fib-sem instrument. *Microscopy and Microanalysis*, 11(S02):830831, 2005.

[52] K. Otsuka, H. Sakamoto, and K. Shimizu. Successive stress-induced martensitic transformations and associated transformation pseudoelasticity in cu-al-ni alloys. *Acta Metallurgica*, 27(4):585 – 601, 1979.

[53] M.P. Li and Q.P. Sun. Nanoscale phase transition behavior of shape memory alloys closed form solution of 1d effective modelling. *Journal of the Mechanics and Physics of Solids*, 110:21 – 37, 2018.

[54] L.C. Brinson. One-dimensional constitutive behavior of shape memory alloys: Thermomechanical derivation with non-constant material functions and redefined martensite internal variable. *Journal of Intelligent Material Systems and Structures*, 4(2):229–242, 1993.

[55] Mohammad-Zaman Kabir and Behrang Tavousi Tehrani. Closed-form solution for thermal, mechanical, and thermo-mechanical buckling and post-buckling of sma composite plates. *Composite Structures*, 168:535 – 548, 2017.

[56] M. Brocca, L.C. Brinson, and Z.P. Baant. Three-dimensional constitutive model for shape memory alloys based on microplane model. *Journal of the Mechanics and Physics of Solids*, 50(5):1051 – 1077, 2002.

[57] Eric N. Hahn and Marc A. Meyers. Grain-size dependent mechanical behavior of nanocrystalline metals. *Materials Science and Engineering: A*, 646:101 – 134, 2015.

[58] W.-F. Rao, Y.-C. Xu, J. W. Morris, Jr., and A. G. Khachaturyan. Responses of Pre-transitional Materials with Stress-Generating Defects to External Stimuli: Superelasticity, Supermagnetostriction, Invar and Elinvar Effects. *ArXiv e-prints*, May 2017.

[59] Armen Khachaturyan. personal communication, 2017.

[60] Markus Ernst Gruner, Sebastian Fähler, and Peter Entel. Magnetoelastic coupling and the formation of adaptive martensite in magnetic shape memory alloys. *Phys. Status Solidi B*, 251(10):2067–2079, 2014.

[61] HKDH Bhadeshia. Martensite in steels. *Materials Science & Metallurgy*, 2002.

[62] G. R. Barsch and J. A. Krumhansl. Twin boundaries in ferroelastic media without interface dislocations. *Phys. Rev. Lett.*, 53:1069–1072, Sep 1984.

[63] GEORGE B. KAUFFMAN and ISAAC MAYO. The story of nitinol: The serendipitous discovery of the memory metal and its applications. *The Chemical Educator*, 2(2):1–21, 1997.

[64] Kaushik Bhattacharya. *The Microstructure of Martensite and Its Implications for the Shape-Memory Effect*. Springer New York, New York, NY, 1993.

[65] Oleg Shchyglo, Umut Salman, and Alphonse Finel. Martensitic phase transformations in niti-based shape memory alloys: The landau theory. *Acta Materialia*, 60(19):6784 – 6792, 2012.

[66] J. M. Ball and R. D. James. *Fine Phase Mixtures as Minimizers of Energy*, pages 647–686. Springer Berlin Heidelberg, Berlin, Heidelberg, 1989.

[67] Yintao Song, Xian Chen, Vivekanand Dabade, Thomas W. Shield, and Richard D. James. Enhanced reversibility and unusual microstructure of a phase-transforming material. *nature*, 502:85–88, October 2013.

[68] Christoph Chluba, Wenwei Ge, Rodrigo Lima de Miranda, Julian Strobel, Lorenz Kienle, Eckhard Quandt, and Manfred Wuttig. Ultralow-fatigue shape memory alloy films. *Science*, 348(6238):1004–1007, 2015.

[69] Jr. William D. Callister and David G. Rethwisch. *Fundamentals of Materials Science and Engineering: An Integrated Approach*. John Wiley and Sons, Inc., Hoboken, NJ, 2008.

[70] Eugene M. Chudnovsky and Javier Tejada. *Lectures on Magnetism with 128 Problems*. Rinton Press, Inc., Princeton, NJ, 2006.

[71] David Jiles. *Introduction to Magnetism and Magnetic Materials*. Taylor and Francis Group, New York, NY, 1998.

[72] Jiyu Fan, Li Pi, Kuang He, Wenqin Wang, and Yuheng Zhang. Charge ordering melting and evidence for a metastable antiferromagnetic phase in nd 0.5(1 x) ca 0.5(1 + x) mn 1 x ti x o 3. *EPL (Europhysics Letters)*, 74(3):506, 2006.

[73] B. D. Cullity and C. D. Graham. *Introduction to Magnetic Materials*. Wiley-IEEE Press, 2 edition, 2008.

[74] O. Hjortstam, K. Baberschke, J. M. Wills, B. Johansson, and O. Eriksson. Magnetic anisotropy and magnetostriction in tetragonal and cubic ni. *Phys. Rev. B*, 55:15026–15032, Jun 1997.

[75] M. Farle, B. Mirwald-Schulz, A. N. Anisimov, W. Platow, and K. Baberschke. Higher-order magnetic anisotropies and the nature of the spin-reorientation transition in face-centered-tetragonal ni(001)/cu(001). *Phys. Rev. B*, 55:3708–3715, Feb 1997.

[76] C. Kittel. *Introduction to Solid State Physics*. Wiley, 2004.

[77] Charles Kittel. Physical theory of ferromagnetic domains. *Rev. Mod. Phys.*, 21:541–583, Oct 1949.

[78] L. D. Landau and E. M. Lifshitz. On the theory of the dispersion of magnetic permeability in ferromagnetic bodies. *Phys. Z. Sowjetunion*, 8:153, 1935.

[79] Earl Callen and Herbert B. Callen. Magnetostriction, forced magnetostriction, and anomalous thermal expansion in ferromagnets. *Phys. Rev.*, 139:A455–A471, Jul 1965.

[80] Toyota Motor Corporation. Method for producing fepd/fe magnetic nanoparticles, November 2010.

[81] Yu. I. Ustinovshchikov, I. N. Shabanova, and N. V. Lomova. Microstructures responsible for the invar and permalloy effects in fe-ni alloys. *Russian Metallurgy (Metally)*, 2015(5):389–394, 2015.

[82] R. Oshima, M. Sugiyama, and F. E. Fujita. Tweed structures associated with fcc-fct transformations in fe-pd alloys. *Metallurgical Transactions A*, 19(4):803–810, 1988.

[83] Koki Abe, Yoshiko Miyamoto, and Soshin Chikazumi. Magnetocrystalline anisotropy of low temperature phase of magnetite. *Journal of the Physical Society of Japan*, 41(6):1894–1902, 1976.

[84] S. Chikazumi and S. H. Charap. *Physics of Magnetism*. R. E. Krieger Pub. Co., Reading, Massachusetts, 1978.

[85] Jürgen Hesse. From feni-invar to fenimn reentrant spin-glasses. *Hyperfine Interactions*, 47(1):357–378, Mar 1989.

[86] Pedro Gorria, David Martínez-Blanco, María J. Pérez, Jesús A. Blanco, Antonio Hernando, María A. Laguna-Marco, Daniel Haskel, N. Souza-Neto, Ronald I. Smith, William G. Marshall, Gaston Garbarino, Mohamed Mezouar, Alejandro Fernández-Martínez, Jesús Chaboy, L. Fernandez Barquín, J. A. Rodriguez Castrillón, M. Moldovan, J. I. García Alonso, Jianzhong Zhang, Anna Llobet, and J. S. Jiang. Stress-induced large curie temperature enhancement in $fe_{64}ni_{36}$ invar alloy. *Phys. Rev. B*, 80:064421, Aug 2009.

[87] John Cumings. personal communication, 2018.

[88] Jingyue Liu. Scanning transmission electron microscopy and its application to the study of nanoparticles and nanoparticle systems. *Journal of Electron Microscopy*, 54(3):251–278, 2005.